Theoretical and Experimental Investigation of 3D Plasmonic Stub Resonators

by

Solmaz Naghizadeh

A Dissertation Submitted to the
Graduate School of Sciences and Engineering
in Partial Fulfillment of the Requirements for
the Degree of

Doctor of Philosophy

In

Physics

September 2016

Theoretical and Experimental Investigation of
3D Plasmonic Stub Resonators

Koç University
Graduate School of Sciences and Engineering

This is to certify that I have examined this copy of a doctoral dissertation by

Solmaz Naghizadeh

and have found that it is complete and satisfactory in all respects,
and that any and all revisions required by the final
examining committee have been made.

Committee Members:

_____
Asst. Prof. Dr. Şükrü Ekin Kocabaş (Advisor)

_____
Prof. Dr. İrşadi Aksun

_____
Assoc. Prof. Dr. Kaan Güven

_____
Assoc. Prof. Dr. Arda Deniz Yalcinkaya

_____
Asst. Prof. Dr. Alexandr Jonas

Date:

I dedicate this thesis to my husband Philipp Heck for nursing me with affections and his dedicated support for success in my PhD program.

ABSTRACT

In this thesis we compare the performance of plasmonic waveguide integrated stub-resonators based on 2D metal-dielectric-metal (MDM) and 3D slot-waveguide (SWG) geometries. We show that the scattering matrix theory can be extended to 3D devices, and by employing the scattering matrix theory we provide the guidelines for designing plasmonic 2D and 3D single-stub and double-stub resonators with a desired spectral response at the design wavelength. We provide transmission maps of 2D and 3D double-stub resonators versus stub lengths, and we specify the different regions on these maps that result in a minimum, a maximum or a plasmonically induced transparency (PIT) shape in the transmission spectrum. Radiation loss from waveguide terminations leads to a performance degradation in the 3D slot-waveguide based resonators. We illustrate improved waveguide terminations that boost resonator properties. We verify our results with 3D FDTD simulations.

The designed devices are then fabricated with Electron Beam Lithography (EBL), employing standard fabrication procedure. In the fabrication phase we add Yagi-Uda style dipole antennas to the input and output ports of the slot-waveguides to increase the coupling efficiency of the far-field input beam into the subwavelength gap of the slot-waveguides. Furthermore, 90 degree bent waveguides are used instead of the straight waveguides to increase the signal-to-noise ratio via a cross-polarization based measurement scheme. A home-built far-field cross-polarization reflection microscope setup is used for the characterization of our plasmonic double-stub resonators.

ÖZETÇE

Bu tezde 2 boyutlu metal-dielektrik-metal (MDM) ve 3 boyutlu oluk dalga kılavuzu geometrisine sahip plazmonik dalga kılavuzlarına eşlenik çubuk tınlayıcının performansı karşılaştırılır. Saçılım matrisi kuramının 3 boyutlu cihazlara uygulanabileceği sunulup, bu kuramı kullanarak tasarım dalga boyunda istenilen tayfsal tepkiyi gösterecek 2 boyutlu ve 3 boyutlu tek veya çift çubuklu tınlayıcı tasarımı için gerekli prensipler sağlanır. 2 boyutlu ve 3 boyutlu çift çubuklu tınlayıcıların çıkıntı uzunluğuna bağlı olarak geçirim haritası elde edilip, bu harita üzerinde hangi bölgelerin geçirim tayfında çukur, tepe veya plazmonik olarak tetiklenen saydamlık etkilerine yol açtığı belirtilir. Dalga kılavuzu uçlarındaki ışınım kayıpları 3 boyutlu oluk dalga kılavuzu tasarımına sahip yapılarda performans kaybına yol açar. Bu sorunun üstesinden gelmek için yeni dalga kılavuzu uçları tasarlanır ve tınlayıcı özelliklerini ne yönde iyileştirdiği gösterilir. Elde edilen sonuçlar 3 boyutlu FDTD simülasyonları ile doğrulanır.

Tasarlanan fotonik cihazlar elektron demeti litografisi ile üretilir. Üretim aşamasında plazmonik oluk dalga kılavuzuna Yagi-Uda tarzında dipol antenler eklenir, bu sayede uzak alandaki lazer ışığının dalga kılavuzu kiplerine eşlenimi sağlanır. Ek olarak, kıvrımlı dalga kılavuzları kullanılarak ölçüm aşamasında sinyalin gürültüye oranını arttırılır. Çift çubuklu tınlayıcıların özelikleri ev yapımı polarizasyona duyarlı yansıma mikroskopu düzeneği kullanılarak saptanır.

ACKNOWLEDGEMENT

There are a number of people who helped me to accomplish my PhD and to whom I am greatly indebted.

First and foremost, I wish to express my sincere appreciation to Dr. Şükrü Ekin Kocabaş, my supervisor during my doctoral study, for giving me a chance to be a part of his group. Without him I had a hard time finding my place at the university. It is his patient guidance, continuous encouragement, understanding and good temper that helped me seeing my PhD through to the end.

Next, I would like to give my thanks to my husband Philipp for his emotional support during my hardships. He generously gave me freedom to achieve my personal goals and development cause we had to live separately for three years until my PhD was done. His presence enriched my life and helped me to realize my potentials.

I would like to thank the *Scientific and Technological Research Council of Turkey* (TUBITAK) for financially supporting us during the project with Grant No: 112E247.

I would like to thank my group members Adeel Afridi and Ongun Arisev for creating a friendly and cooperative atmosphere.

I would like to thank my friend Nasrin Yousefi for being a friend in need and Sanaz and Yahya for making the last days of my stay at university joyful.

Last but not least, I would like to thank my family, for their greatest love and caring.

TABLE OF CONTENTS

LIST OF TABLES

LIST OF FIGURES

Chapter 1
INTRODUCTION

The continued shrinking of device sizes in integrated circuits into nanoscale, as predicted by Moore's law [1], requires size reduction of the data carrying metal wires into nanoscale accordingly. As a result of this miniaturization, the performance of traditional metal wire interconnects operated by electric charge and discharge is expected to degrade [2]. Efficiency of an interconnect is evaluated based on three prominent parameters: delay time for signal propagation, power dissipation, and cross-talk amongst the wires [3].

By reducing the size of the traditional metal wires all these three parameters are increased in an undesired manner which has caused some researchers in the semiconductor industry to consider alternative approaches to the charging and discharging of wires for communicating information across integrated circuits, to minimize delay, energy dissipation and cross-talk. The chip designers have been able to develop ever smaller and faster transistors but have had a harder time building minute electronic circuits that can move data quickly across the chip. Therefore, regarding speed, power, and noise wires are as important as transistors.

These problems with conventional metal wires arise from the fundamental physical limitations of transmitting information along these interconnects by electric charging and discharging [4]. The delay time for signal propagation is limited by RC time constant of the interconnect (R and C being the total resistance and capacitance of the interconnect). As the cross-sectional area A of a metal wire is reduced, the wire resistance $R=\rho L/A$ increases (where ρ and L are wire resistivity and length, respectively). Furthermore, the effective resistivity ρ of the metal interconnect increases above the resistivity of bulk metal as the cross-sectional dimensions of the wire approach the mean free path of conduction electrons [5,6]. Since the distributed capacitance per unit length c does not change significantly as the interconnect is scaled down, the time for a signal to propagate

across a fixed distance of an integrated circuit will increase with geometric scaling due to the undesirable increase in wire resistance.

The energy consumed to transmit a bit through a length of interconnect is a good measure of the energy efficiency of communication on an integrated circuit. The total energy required to charge a conventional wire of capacitance C through a potential change V is CV^2, half of this energy is the change in electrostatic potential energy of the wire, and the other half is dissipated in wire resistance during charging leading to a dissipation of $\frac{1}{2}CV^2$ on average. One of the early motivations for circuit integration was the reduction of this energy consumption by reducing wire capacitance $C=cL$ between components through shorter inter-component distances [1]. The operating potential V is presently fixed to that required for switching of transistors which is of the order of 1V. The distributed capacitance per unit length c of an interconnect is weakly dependent on geometry – and is in fact invariant upon geometric scaling of cross-sectional dimensions. It is only the ratio of cross-sectional dimensions that determines c, and not the absolute values of cross-sectional dimensions. For example, the capacitance per unit length of a coaxial line only depends on the logarithim of the ratios of the inner and outer conductor radii, not on the actual cross-sectional size or overall diameter of the line. Consequently, the energy dissipated per unit length per bit transmission is weakly dependent on interconnect scale. Hence, by having C and V fixed the energies to communicate data across the chip cannot be reduced. However, as interconnect density increases through scaling, the energy dissipated per unit of chip area will increase proportionally.

Finally, the increase in distributed wire resistance per unit length $r=R/L$ with geometric scaling increases the cross-talk amongst wires. As so-called aggressor wires are charged to transmit data, the potential on an adjacent victim wire will change substantially due to capacitive coupling $C_{\text{wire-wire}}$ between the aggressor and victim wires (see Figure 1.1). At large operating frequencies typical of high-performance integrated circuits, the impedances between interconnects ($1/j\omega C_{\text{wire-wire}}$ where ω is the angular frequency) are reduced to values much lower than the resistance $R=rL$ through which current must flow in the victim wire to counteract induced potential changes. As a result, the scaling trends of increasing frequency and increasing wire resistance lead to greater cross-talk amongst

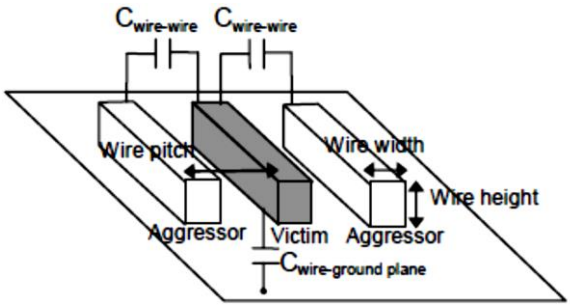

Figure 1.1 Electrostatic interconnect geometry where a victim wire's potential is changed as a result of capacitive coupling, $C_{\text{wire-wire}}$, to adjacent aggressor wires [4].

wires. As cross-talk increases, bit-error-rates increase, such that metal interconnects cease to be sufficiently reliable components in a fully operational integrated circuit.

Nanophotonic interconnects have been proposed as a replacement of global metal interconnect because of their almost distance-independent power consumption and low-latency and high bandwidth. Employing optical interconnection which uses light instead of electricity to carry the data, requires high speed optical transceivers (device that can both transmit and receive communications) monolithically integrated on electronic ICs to convert digital information from electrical domain to optical domain (transmit) and vice versa (receive). Such transceivers should be compact, offer large bandwidth and consume little power in order to be economically and technologically efficient.

The most promising technology for realization of optical transceivers seemed to be the CMOS compatible silicon photonics platform whose large scale fabrication is ensured by well-developed advanced CMOS fabrication lines. However, photonic components have diffraction-limited sizes such that even state-of-the-art Si photonic transceivers are bulky compared to electronic transistors. For example, currently available CPUs have a gate length of approximately 20nm, or roughly 40 atoms, given that the standard wavelength for telecommunication devices is 1550nm, integrated photonic systems are on the micron scale and 10–100 times larger than today's transistors [7]. Therefore, the integrated Si photonic transceivers would occupy large portion of the optoelectronic ICs making them economically not efficient because of the expensive cost associated to every square micrometer in the CMOS fab. This size mismatch between micrometer-scale photonic

components and nanometer-scale electronic ones limits the integration viability of both technologies on the same chip using the same process.

This size mismatch not only causes fabrication challenges but the relatively bigger sizes of photonic components makes them to have higher capacitance which requires more power consumption to drive and limits the speed at which they can operate. This high power consumption in every photonic link which includes these major components: light source, modulator, photodetector, and amplifier, limits the minimum distance at which nanophotonic waveguides can be more power efficient than electrical signaling. Therefore, although optical interconnects has been proved energy efficient in long distant communications they are not more energy-efficient than metallic wires in shorter communications such as intra-chip or chip-to chip communications.

Moreover, cross talk is a problem for nanophotonic waveguides due to the low confinement of the modes and large bending losses. The minimum pitch of a Si waveguide to avoid cross-talk is 5.5 μm.

Energy already limits our ability to process and communicate information. The fraction of energy used for handling information has risen to a level that is environmentally significant [8,9]. If we cannot continue reducing the energy required to handle each bit, then we cannot continue our exponential growth in the use of information. Over time, ever smaller transistors [1] reduced the logic energy per bit. But, the energy to send information inside electronic machines does not scale down in the same way, especially for longer connections. As a result, most of the energy dissipated inside electronic machines is used to communicate.

To overcome the problems with conventional interconnects and Si-photonics, in recent decades, scientists have been working on a new technique for transmitting optical signals through minuscule nanoscale structures. In the 1980s researchers experimentally confirmed that directing light waves at the interface between a metal and a dielectric can result in the generation of surface waves called surface plasmon polaritons.

Surface plasmon polaritons (SPPs) are one-dimensional bound electromagnetic waves propagating along metal-dielectric (MD) interfaces. These non-radiative modes result

from longitudinal oscillation of free electrons along MD interfaces that are excited by an incident electromagnetic wave with its propagation vector modified by a prism or a grating to match the propagation vector of an SPP mode [10]. The coupling of free electrons with the incident electromagnetic wave assists the wave to propagate along metallic surfaces further than the skin depth of the bulk metal. SPP modes exponentially decay into the dielectric and metallic media on both sides of the MD interface. This is the origin of subwavelength confinement in the plasmonic field and more confinement can be reached by bringing two MD layers together [11].

At first glance, the use of metallic structures to transmit light signals seems impractical, because metals are known for high optical losses. The electrons oscillating in the electromagnetic field collide with the surrounding lattice of atoms, rapidly dissipating the field's energy. But the plasmon losses are lower at the interface between a thin metal film and a dielectric than inside the bulk of a metal because the field spreads into the nonconductive material, where there are no free electrons to oscillate and hence no energy-dissipating collisions. This simple metal-dielectric (MD) structure serves as a SPP waveguide and it is the onset of the plasmonic field.

Interestingly, surface plasmons excited at an MD interface maintain the frequency of the exciting light, while at the same time have a much shorter wavelength. These shorter wavelengths allow the construction of nanoscale waveguides and devices that tightly confine even very high frequency electromagnetic waves (optical frequencies). As a result, by emergence of SPP waveguides, efforts for designing plasmonic devices that could manipulate SPP waves initiated.

Researchers have constructed passive and active plasmonic devices with dimensions as small as 50 nanometers—about the same size as the smallest electronic circuits. Plasmonic devices based on SPP modes are therefore capable of overcoming the diffraction limit, which dictates the minimum size of the photonic devices, and are expected to resolve the size mismatch between photonic and electronic devices.

One important aspect of plasmonics is that, the propagation velocity of plasmons in SPP waveguides can be comparable to the speed of light and hence they offer the speed advantage of optical interconnects [12]. Therefore, SPP wire waveguides, so-called

plasmonic interconnects, have the potential to reduce signal delay, and are investigated as alternative for photonic interconnects.

Another important aspect of plasmonics is that, unlike optical modes, the SPP modes are highly confined which is required for low cross-talk among high density plasmon wire interconnects. In a plasmon metal-dielectric-metal (MDM) waveguide, a typical plasmonic interconnect which consists of two metallic sheets separated by a thin dielectric core, to achieve maximum mode confinement the depth of the metal should be optically opaque, as thick as the metal skin depth (approximately 20 nm). Having a metal thickness a little higher than double the skin depth ensures that modal fields remain confined within the core and metallic cladding, leading to very low pitch of 100s of nanometers (compared to 5.5 μm of Si waveguides). For a core thickness less than roughly 50 nm, only plasmonic modes will propagate. As the core thickness is increased, the waveguide begins to support transverse electric and magnetic photonic modes, similar to microwave waveguides. Therefore, depending on the type of the mode and its level of confinement the dielectric thickness can range from just a few nanometers to over hundreds of nanometers. Therefore, it is the highly localized nature of SPPs that distinguishes them from optical modes in dielectric waveguides as a new means of integrated circuit communication.

In addition to providing low cross-talk, plasmonic interconnects enable routing light signal around a sharp bends a feature that is never feasible with photonics interconnects [13].

To summarize, the properties of SPPs that make them worthy of consideration as an alternative means of communication in an integrated circuit are: (1) the group velocity of SPPs can approach that of light, this solves the signal delay (2) SPPs can be localized to the surface of a metal, this mitigates the cross-talk, (3) the energy required to send and receive an SPP pulse can be less than that needed for electric charging of a metallic wire, and (4) they have very large operating bandwidths.

Some research has been conducted to compare the performances of electrical, optical, and plasmonic on-chip interconnects [4,14]. It is found that plasmonic interconnects offer reduced signal latency compared to conventional CMOS interconnects, however, the high

confinement required for low cross-talk amongst high density plasmon wire interconnects significantly increases energy dissipation per transmitted bit, above and beyond that required for electric charge/discharge interconnects at the same density [4].

The plasmonic interconnects although are much faster compared to CMOS interconnects, due to the limitation on propagation length, according to International Technology Roadmap for Semiconductors (ITRS) [15], are expected to be used as future intermediate level interconnects.

Despite passive plasmonic waveguides which are less practical because of the high losses, active plasmonic devices can still be useful because of their high speed and ultra-compact characteristics. Further, due to their smaller sizes and thus smaller capacitances, plasmonic devices have been proved to be more energy efficient than the Si-photonic devices.

Realization of various plasmonic devices such as electrically pumped SPP lasers [16], and plasmonic modulators [17,18,19] has encouraged researches to employ Si-plasmonic transceivers instead of Si-photonic transceivers combined with photonic interconnects [20,21] to reduce the energy consumption of optical links.

The key plasmonic components are the plasmonic nanolaser and the modulator which make the plasmonic transmitter and plasmonic amplifiers and photodetectors which make the plasmonic receiver. In a Si-plasmonic platform (shown in Figure 1.2) light generated

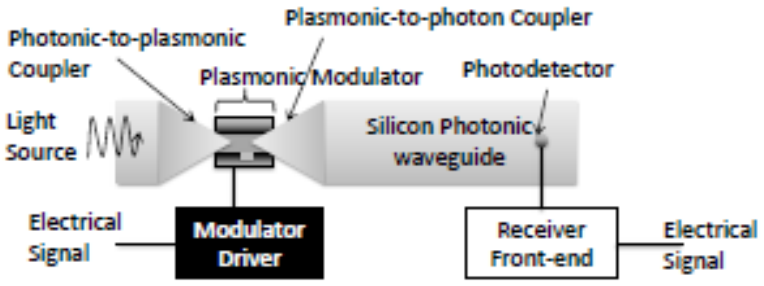

Figure 1.2 Hybrid Link: By using a plasmonic modulator and silicon photonic waveguide, we can achieve the best of both worlds: long range propagation, and low power consumption and high performance modulation. Couplers convert photons into SPP and vice versa [20].

in plasmonic nanolaser is coupled into the Si nanowire waveguide which feeds the rest of the circuit with a continuous wave signal. After being modulated in the modulator, the light is then coupled out from the chip using a grating coupler. The optical signal is then transferred to the neighboring chip through a passive optical link. The signal is detected by the plasmonic photodetector of the transceiver located on the second chip. This approach saves a lot of heating power required for photonic micro-ring modulators since their resonance range is adjusted using heating.

Many waveguide structures have been proposed and have been investigated for SPP waves [22,23,24,25,26,27,28]. Among them, 2D metal-dielectric-metal (MDM) plasmonic waveguides [11] with confinement in one dimension, and 3D plasmonic slot waveguides (SWG) [26,27] with confinement in two dimensions have gained popularity due to their high confinement, long propagation length, wide bandwidth, and ease of fabrication.

The development of resonators compatible with the underlying plasmonic waveguides helps with the design of functional devices. Stub resonators which are finite-length waveguides side coupled to the input waveguide are widely used in microwave engineering for impedance matching, filtering or switching purposes [29]. Due to the similarities between plasmonic waveguides and transmission lines, the stub idea has also been successfully extended to plasmonic applications at optical frequencies. As already stated above, this is due to the unique property of SSP waveguides that are capable of routing electromagnetic waves around sharp corners such that we could not have stub resonators with photonoic waveguides because of high radiation losses at bends. Two-dimensional plasmonic single-stub (SS) and double-stub (DS) resonators have been employed in various applications such as tunable stop-band or band-pass filters [30,31], low-power high-contrast switches [32], absorption switches [33], high-performance T-splitters [34], reflection-less step junctions [35], plasmonic demultiplexers [31,36], modulators [37], and observation of plasmonic analogue of electromagnetically induced transparency phenomenon (PIT) [38,39,40,41,42]. Arrays of single- or double-stub resonators have also been utilized in developing surface plasmon reflectors [43], or slow-light waveguides [33, 38].

Many of the proposed and designed plasmonic devices have used 2D plasmonic MDM waveguides as their platform for three main reasons: a) two-dimensional MDM waveguides do not suffer from radiation losses which significantly degrade the device performance, b) MDM waveguides are infinite in one dimension thus their 2D numerical simulations are easier to handle, c) a variety of analytical methods such as transmission line theory (TLT) [31,35], scattering matrix theory (SMT) [30,38], and temporal coupled mode theory (CMT) [32] have been successfully applied in the analysis of 2D MDM-based devices. Nonetheless, to fully realize an integrated plasmonic circuit and to avoid cross-talk among densely packed components, two-dimensional confinement offered by 3D SWG-based structures is needed. Additionally, SWG-based structures are much more compatible with the integrated circuit fabrication technology than the MDM-based devices.

However, a slot-waveguide is inherently an open system such that the introduction of any type of discontinuity along its propagation axis results in scattering and thus radiation loss to the substrate and cladding layers [34]. Slot-waveguide propagation loss and radiation loss hinder the performance of plasmonic waveguide integrated structures. The propagation loss can be reduced by decreasing the device footprint to dimensions far less than the propagation length of the waveguide mode, however suppressing the radiation loss remains an issue to be tackled.

So far, only general properties of 2D MDM waveguides and 3D slot waveguides, such as dispersion, propagation length, and confinement factors, have been compared [27,34]. However, to the best of our knowledge, comparison between functional 2D and 3D plasmonic devices has not been made yet. Therefore, in this thesis we compare the performance of 2D and 3D versions of two functional plasmonic devices, i.e., single-stub resonator (SSR) and double-stub resonator (DSR), around the operating wavelength of 1550nm. In this comparison, 2D structures utilize MDM waveguides, 3D structures utilize slot waveguides. Schematics of 2D and 3D plasmonic and microwave single- and double-stub resonators are shown in Figure 1.3 and Figure 1.4 for comparison and illustration.

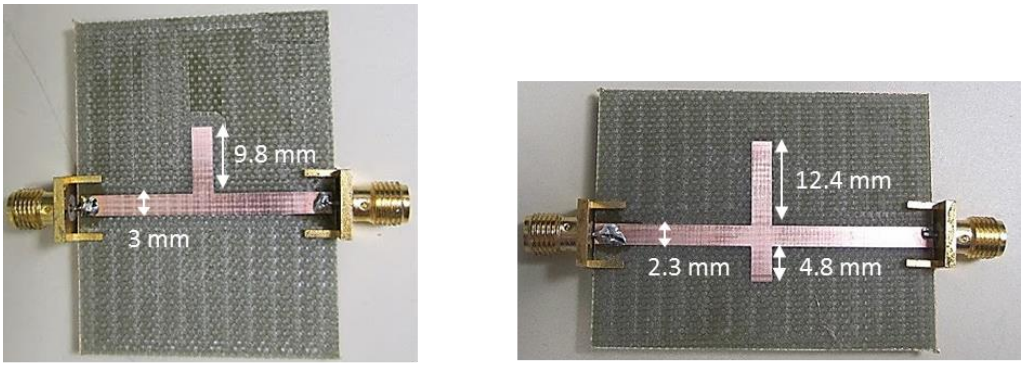

Figure 1.3 (a) Single-stub microstrip resonator used as bandstop filter, (b) double-stub microstrip resonator used as bandpass filter in communication systems. Microstrip resonators have dimensions around 1cm and they operate at GHz.

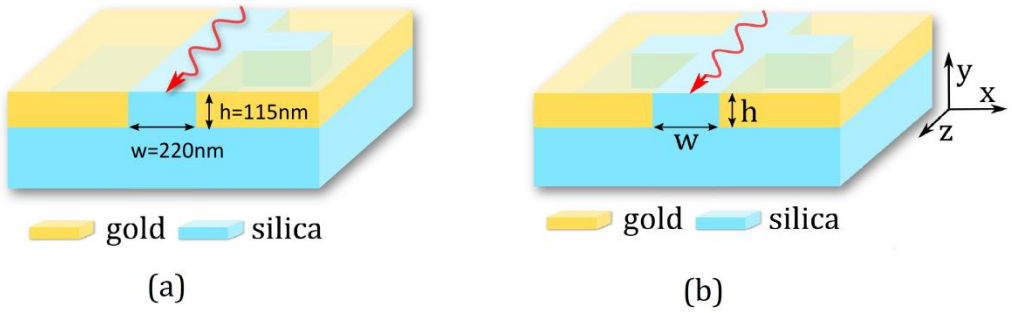

Figure 1.4 (a) 3D plasmonic single-stub resonator, (b) 3D plasmonic double-stub resonator, without top cladding for more clear visualization. In both cases the SPP wave propagates along the *z*-direction. Plasmonic stub-resonators have nanoscale dimensions and are not visible with bare eyes. These resonators operate at 100s of THz.

Moreover, utilizing the simulation results of DS resonators we design a compact and easy to fabricate 3D terminated-end (TE) to boost the back reflection from open 3D TEs.

It should be noted that to avoid radiation losses at the terminated ends, stub-resonators based on three-dimensional plasmonic coaxial waveguides with performances close to their MDM counterparts has been offered [44]. However, fabrication of plasmonic coaxial waveguides in a manner compatible with integrated circuit technology is a challenge.

We analyzed the spectral response of the 2D and 3D plasmonic single-stub and double-stub resonators numerically with finite-difference time-domain (FDTD) method and

verified its results with a semi-analytical model based on the scattering matrix theory. We fabricated the designed structures with Electron Beam Pattern Generator EBPG (Vistec EBPG 5000PlusES) of Sabanci University [Sabanci University Nanotechnology Research and Application Center (SUNUM)] as shown in Figure 1.5.

The fabricated designs are then experimentally characterized and measured with a home-made far-field cross-polarization microscope setup.

This thesis is composed of three parts. In chapter two we review the theory and simulation results. In chapter three we give the fabrication results. And finally, in chapter four the experimental setup is introduced and the experimental results are provided.

Figure 1.5 Electron Beam Pattern Generator EBPG (Vistec EBPG 5000PlusES).

Chapter 2
THEORY AND SIMULATION

In this chapter we provide the simulation results of the structures that we inspected. We used a commercial-grade simulator based on the finite-difference time-domain method to perform the calculations [45].

In section 2.1 we introduce the 2D and 3D waveguides and single-stub and double-stub resonator geometries and the nomenclature used to define each structure.

In section 2.2, we overview the application of the semi-analytical scattering matrix model to the stub-resonators and we provide the elements of the scattering matrix required for the analysis of each stub-resonator. Scattering matrix model provides us with insight to the operational mechanism of the single-stub and double-stub resonators.

In section 2.3, we demonstrate the simulation method for evaluating the reflection and transmission coefficients of the junctions. We verified the results of our simulation model, for obtaining the reflection and transmission coefficients, against the results obtained by FDTD Solutions built-in package *Mode Expansion Monitor*.

In section 2.4, the numerical and semi-analytical results for the comparison of the 2D and 3D structures studied in this work are provided.

2.1 Structures and their Specifications

2.1.1 Plasmonic 2D MDM and 3D slot waveguides

Schematics of the 2D plasmonic metal-dielectric-metal (MDM) waveguide and 3D plasmonic slot-waveguide (SWG) that we used as our reference structures are depicted in Figure 2.1(a,b), respectively. In both cases dielectric parts are silica and metallic parts are gold with complex dielectric function taken from [46]. Small optical losses of silica in our wavelength of interest 0.8-2.3 μm were neglected and its refractive index was set to a constant value of 1.44. We use a symmetric slot-waveguide with identical substrate and superstrate materials (silica) which ensures the existence of a bound mode for a broadband excitation [27]. The two waveguiding structures support deep subwavelength

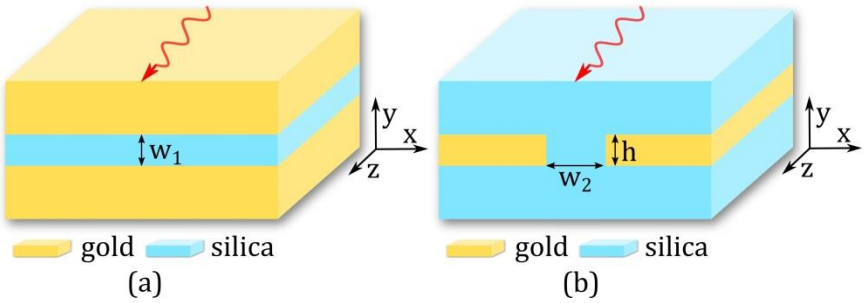

Figure 2.1 (a) 2D MDM waveguide (gold/silica/gold) with width w_1=200 nm, (b) SWG with dimensions $w_2 \times h$=220 nm×115 nm. The mode propagates in the z-direction in both cases.

modes and the symmetric slot waveguide has no wavelength or dimensional cutoff as it scales up or down in contrast to the asymmetric slot waveguides, in which substrate and superstrate layers are not identical [27]. Symmetric SWG waveguides have longer propagation lengths and are capable of guiding a broadband mode compared to the asymmetric slot waveguides.

MDM waveguide is infinite in the x direction and is confined only in y-direction while slot waveguide is confined in both x- and y- directions. The mode propagates along z direction in both 2D and 3D geometries.

Regarding simulation, fabrication, and experimental performance, each of the symmetric and asymmetric waveguides have their own advantages and disadvantages. For instance, broadband simulations are possible with symmetric slot-waveguide however due to wavelength cutoff only narrowband simulations are possible with asymmetric slot-waveguides. On the other hand, fabrication of the asymmetric slot-waveguides is less challenging than the symmetric ones. To fabricate a symmetric slot-waveguide, the asymmetric slot-waveguide needs to coated with a cladding layer which might not fill the slot gap fully or uniformly or the filling might be different from one structure to another that will result in discrepancy in the measured results. However, since symmetric slot-waveguides have no cutoff and provide longer propagation lengths than the asymmetric ones, they are experimentally suitable; thus we selected them as a platform for our 3D structures.

In Figure 2.2(a,b), we give the real and imaginary parts of the gold experimental

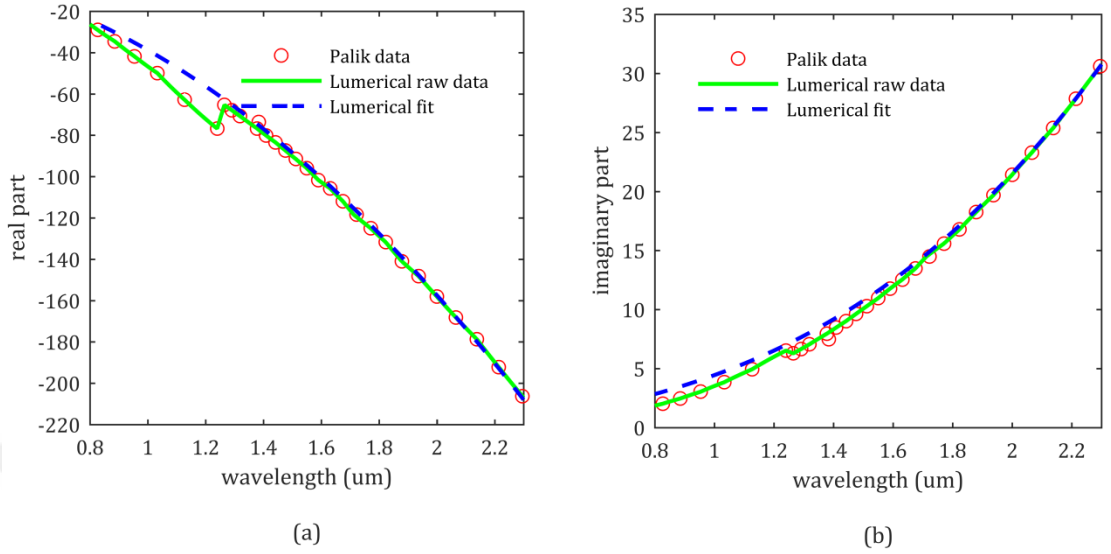

Figure 2.2 (a) Real part of the gold dielectric function, (b) imaginary part of the gold dielectric function.

dielectric function, respectively, along with the curve fitted by the material database of the Lumerical FDTD Solutions into this experimental data. It is this fitted line that we used in our simulations. We have also plotted the data we extracted from Palik handbook on top of the Lumerical FDTD Solutions raw data to ensure that they completely match.

2.1.2 Selecting optimum dimensions

To obtain the optimum width and height for our reference slot-waveguide that provide us long propagation length and moderate confinement at operational wavelength of 1550 nm, using COMSOL Multiphysics, a commercial program that uses finite element method (FEM), we swept over the width (*w)* and height (*h*) of the slot waveguide both over the range 50-300 nm. Then for each (*w*, *h*) pair, we found complex propagation constant $k=\beta+i\alpha$ and then calculated the propagation length defined as $L_p=1/imag(k)=1/\alpha$ and effective refractive index defined as $n_{eff}=real(k)/k_0$ where k_0 is the free-space wave vector. The sweep results are shown in Figure 2.3(a,b).

There is a trade-off between propagation length and modal confinement such that we cannot have high confinement and long propagation length simultaneously [27]. As *w* and *h* increased the propagation length L_p increased and maximum L_p occurred for the maximum values of *w* and *h*, i.e. for $w\times h$=300 nm×300 nm. However, for this *w* and *h*

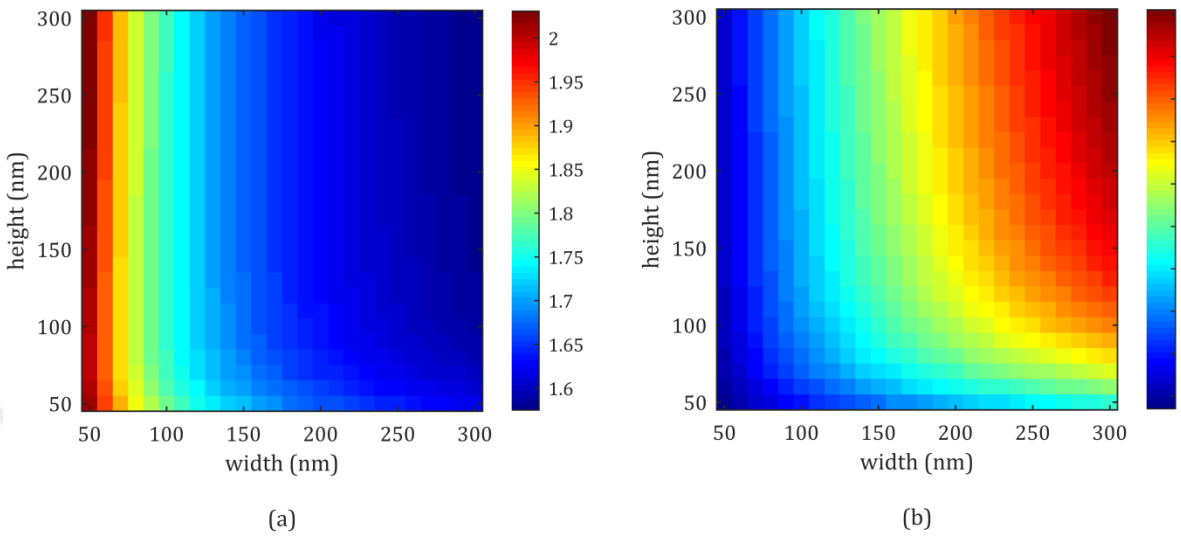

Figure 2.3 3D slot-waveguide (a) effective refractive index (n_{eff}) at 1550 nm versus slot width and height, (b) propagation length (L_p) at 1550 nm versus slot width and height.

pair we have the least confinement. Bearing in mind the fabrication challenges of narrower gaps, we set the widths of MDM and slot-waveguides to 200 nm and 220 nm, respectively, and then by sweeping over the height of the slot-waveguides we found the height h=115 nm for which the real part of the effective refractive index of the modes in the two structures were the same at the operating wavelength of 1550 nm up to 4 decimal points. In microwave frequencies, the k value is critical for stub resonances that is why we keep the k value the same at 1550 nm for MDM and SWG waveguides.

The real part of the complex effective refractive index and propagation length calculated by Comsol for the two waveguides are shown in Figure 2.4(a,b). The intersection point in Figure 2.4(a) amounts to n_{eff}~1.6 at 1550 nm which is higher than the refractive index of the surrounding material i.e. silica of refractive index 1.44. This further ensures that the two waveguides are supporting bound modes. The numerically evaluated propagation length for our reference MDM and slot waveguides amounts to 22.5 μm and 17.5 μm at 1550 nm, respectively.

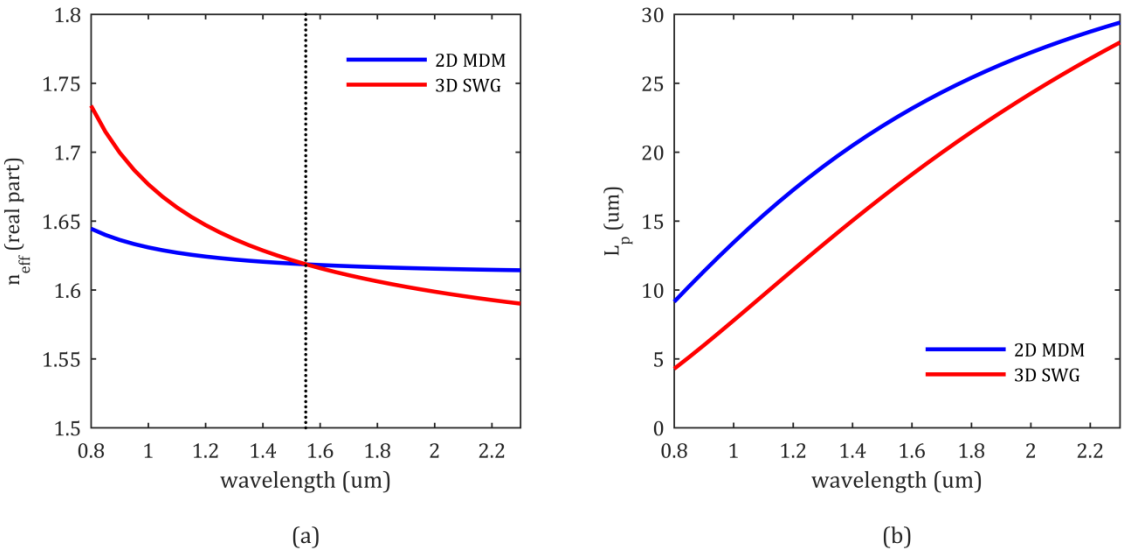

Figure 2.4 (a) Effective index of 2D MDM waveguide with width 200 nm has the same value as 3D slot waveguide with width 200 nm and height 115 nm, vertical black line goes through wavelength 1550 nm, (b) propagation lengths of MDM and slot waveguides.

It is worth noting that, at first, by setting the widths of both 2D and 3D waveguides to 220 nm, we tried to find a height for the 3D waveguide that gave the same n_{eff} at 1550 nm as the 2D MDM waveguide. However, it turned out that this is only possible at very large values of height that converts the 3D slot waveguide into a 2D MDM waveguide. Therefore, we concluded that the width of the 2D MDM waveguide needs to be different than the 3D slot-waveguide. We call the MDM waveguide of width w_1=200 nm and slot waveguide of dimensions $w_2 \times h$=220 nm×115 nm as our reference 2D and 3D waveguides and in all the subsequent 2D and 3D simulations throughout this thesis the material properties and the dimensions of the waveguides will be kept fixed.

It is possible to adjust the 2D MDM waveguide width such that we get a higher height than 115 nm for 3D slot waveguide which results in longer propagation length, however due to our fabrication constraints that limited us in deposing thicker gold layers and removing them in liftoff procedure we continued with the height that we found. Therefore, there are other width and height configurations that result in the same n_{eff} at 1550 nm, however, our particular choice is based on having structures that are easy to fabricate.

2.1.3 Dispersion curves of the waveguides

So far we used Comsol, which is a frequency-domain solver, to obtain the modal properties of our reference waveguides. However, since we will be doing our simulations with FDTD Solutions, to be consistent we also calculated the dispersion curve, effective refractive index n_{eff}, and propagation length L_p of the 2D and 3D waveguides with Lumerical. We used two methods to calculate the dispersion in Lumerical: 1) by recording dominant time-varying electric or magnetic component of modes along propagation direction using point time monitors (PTM), then taking FFT of time dependent fields and monitoring the evolution of the amplitude and phase of the recorded component which give us the propagation length and effective refractive index, respectively, 2) by using built-in mode solver embedded in expansion monitors (EXPM) of FDTD Solutions. The simulation results evaluated with different methods and solvers are shown and compared in Figure 2.5(a-c) for 2D MDM waveguide and in Figure 2.6(a-c) for 3D slot-waveguide.

As it is seen, for 2D structures there is a great match between Lumerical and Comsol results, however in 3D structures there is a discrepancy among different methods at longer wavelengths. In plasmonic waveguides, longer wavelengths have longer propagation lengths L_p and thus their probability to reach the perfectly matched layers (PML) and undergo back reflections is high.

Our results have been extracted for 3D slot-waveguide of 5.5 μm long; however, we have noticed that by increasing the waveguide length to 20 μm, the results obtained by different methods converge. Therefore we conclude that the discrepancy either rises from PML reflections that are not functioning perfectly in the 3D simulations or there is a bug in FDTD Solutions that shows up in 3D simulations.

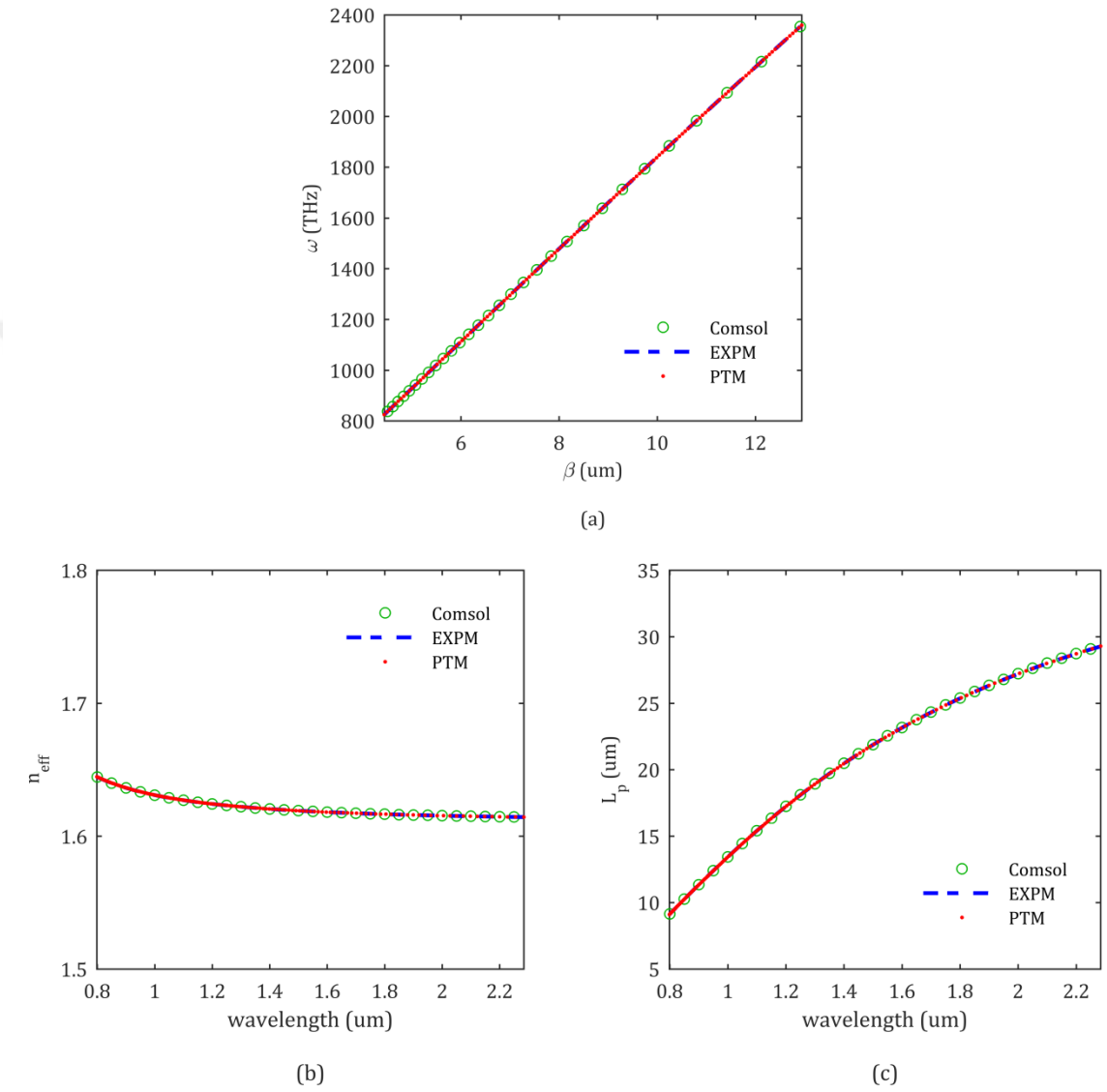

Figure 2.5 2D MDM waveguide: (a) dispersion curve, (b) effective refractive index, (c) propagation length in μm.

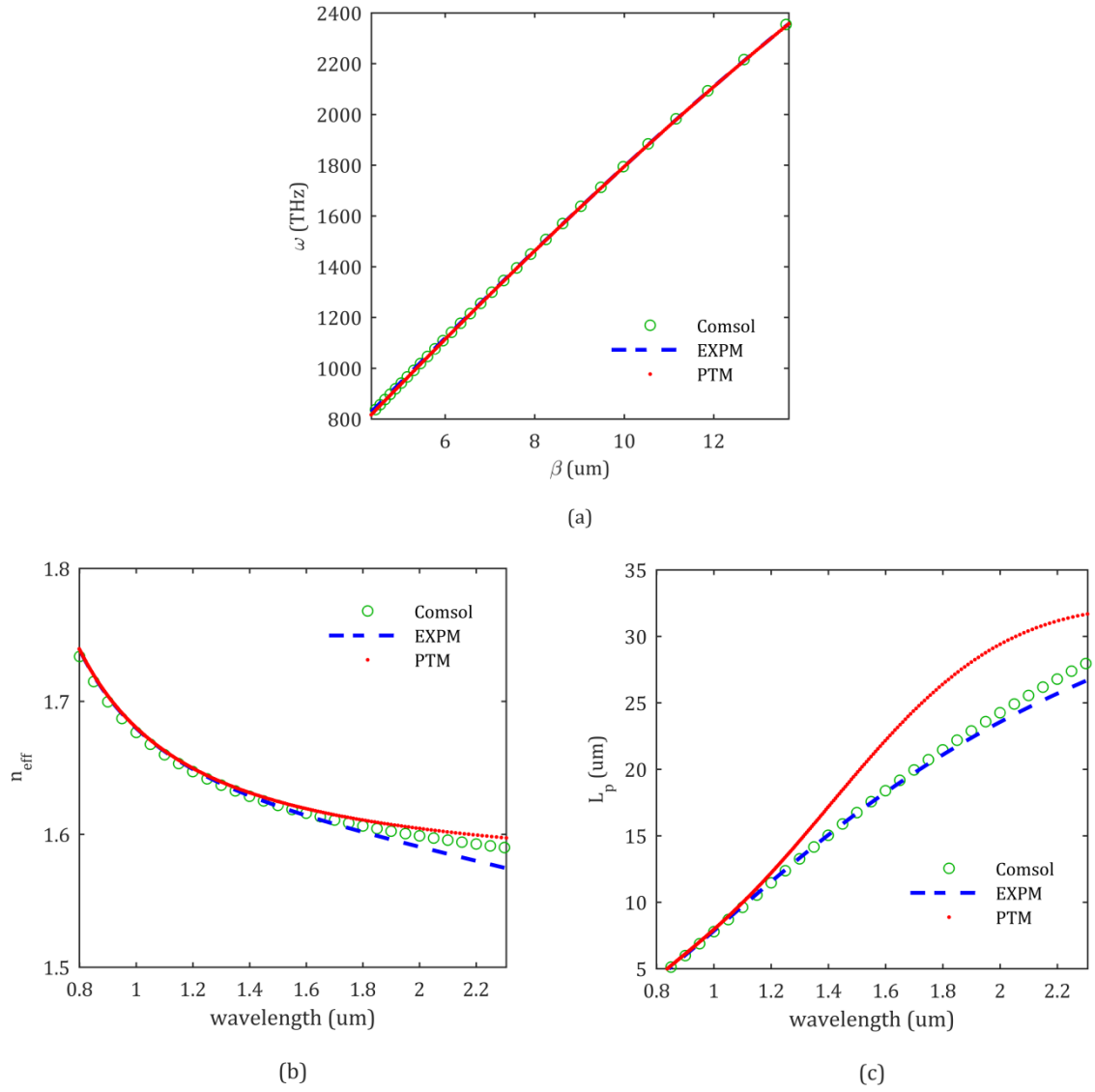

Figure 2.6 3D slot waveguide: (a) dispersion curve, (b) effective refractive index, (c) propagation length in μm.

2.1.4 SWG modal field distributions

Modal field components of our standard slot-waveguide obtained by FDTD solutions at 1550 nm are shown in Figure 2.7. Horizontal electric field component E_x and vertical magnetic field H_y are the dominent components of the mode which makes the central part of the slot eigenenmode a quasi- TEM mode with a much weaker longitudinal field E_z bound to the metal-dielectric interfaces. The size of the bound mode supported by the metallic nano-slot is deeply subwavelength since a majority portion of the mode energy is localized inside the slot region.

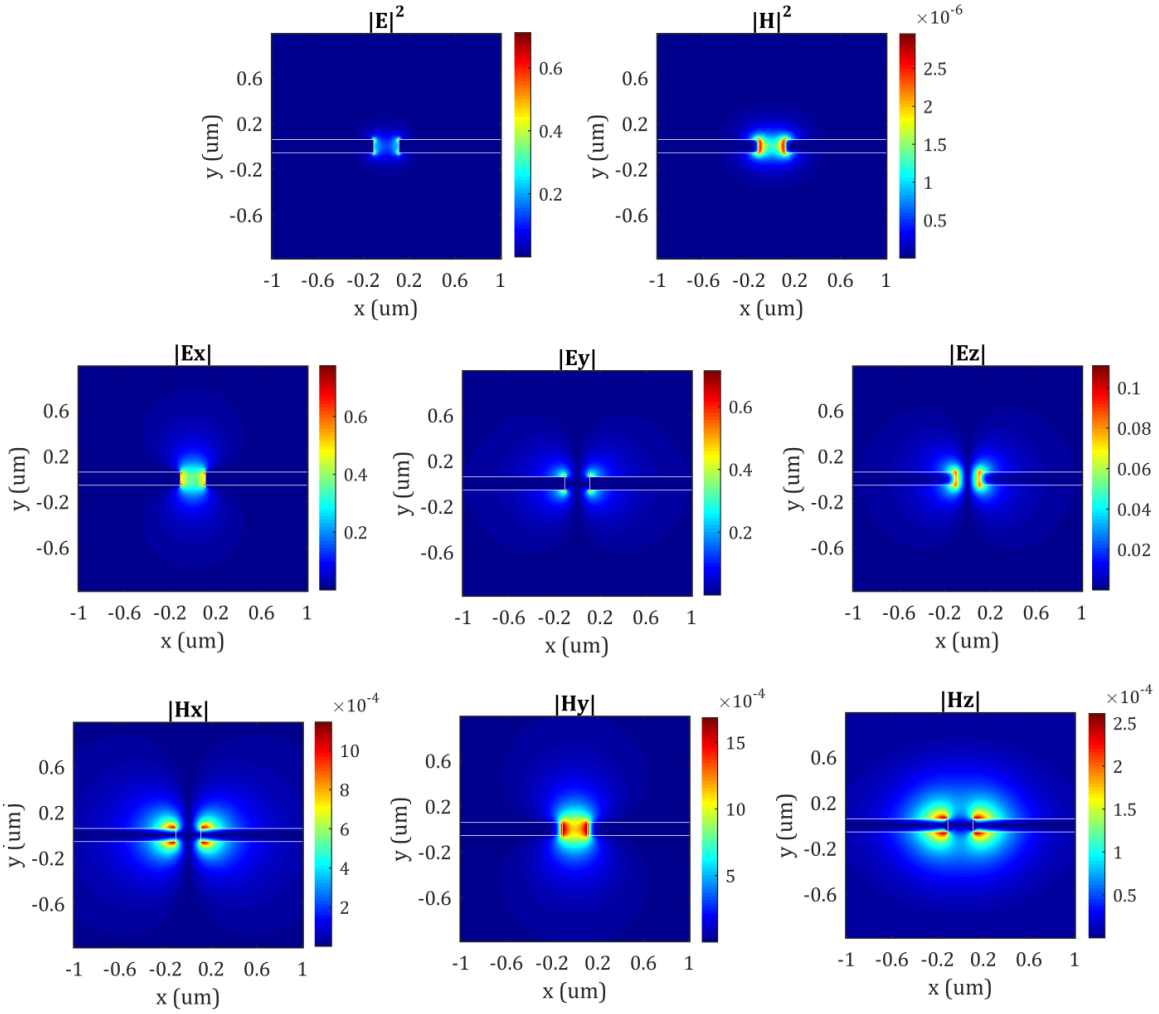

Figure 2.7 Spatial distributions of modal field components of 3D plasmonic slot-waveguide at 1550 nm.

2.1.5 Geometries of 2D and 3D stub-resonators

Schematics of the single-stub resonators (SSR) and double-stub resonators (DSR) for 2D and 3D cases are shown in Figure 2.8. In Figure 2.8(b,d) the top silica cladding has been removed for a more clear visualization of the geometry. Double-stub resonators (DSR) are formed by two single-stub resonators (SSR) located at the same site along the input waveguide, indicating that SS resonators are the building blocks of the DS resonators.

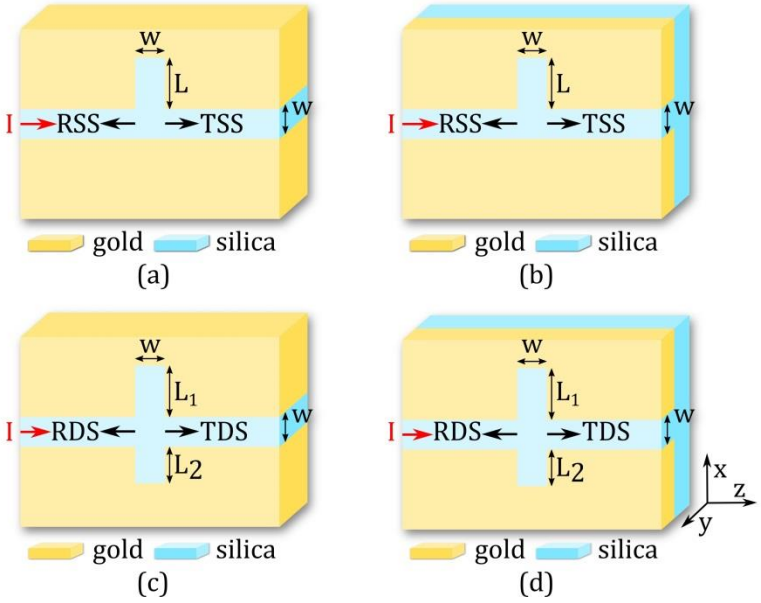

Figure 2.8 (a) 2D single-stub resonator, (b) 3D single-stub resonator without top cladding, (c) 2D double-stub resonator, (b) 3D double-stub resonator without top cladding.

2.2 Analytical Model

The subwavelength size of our reference waveguides compared to the operating wavelength of 1550 nm ensures their single-mode operation which is the prerequisite for employing single-mode scattering matrix theory as a semi-analytical model. We applied scattering matrix theory to analyze the resonator structures.

Scattering matrices are matrices that relate incoming waves to the outgoing waves of a junction. They allow us to calculate the complex reflection and transmission coefficients of a wave scattered at a junction and are helpful in applying transfer matrix theory to the cascaded optical structures [29].

The SS resonator is composed of three simple geometries, namely: a T-junction with input from the left, a terminated waveguide, and a T-junction with input from the top, as sketched in Figure 2.9(a-c) and Figure 2.10(a-c) for 2D and 3D cases, respectively. Complex reflection and transmission coefficients of these geometries are denoted as follows: r_1 is the reflection from the input port of the T-junction (with input from the left), t_1 is the transmission to its straight output waveguide, and t_2 is the transmission to its cross output waveguide [Figure 2.9(a) and Figure 2.10(a)]. r_2 is the reflection from the terminated waveguide [Figure 2.9(b) and Figure 2.10(b)], r_3 is the reflection from the input port of the T-junction (with input from the top), and t_3 gives the corresponding transmission coefficient to its cross output waveguides junction which due to symmetry are identical [Figure 2.9(c) and Figure 2.10(c)].

With these definitions the complex transmission (TSS) and reflection (RSS) amplitudes of 2D single-stub resonator with stub length L are given by [30]

$$TSS = t_1 + \frac{r_2 t_2 t_3 \, exp(2ikL)}{1 - r_2 r_3 \, exp(2ikL)} \qquad (2.1)$$

$$RSS = r_1 + \frac{r_2 t_2 t_3 \, exp(2ikL)}{1 - r_2 r_3 \, exp(2ikL)} \qquad (2.2)$$

The first term in Eq. (2.1), i.e. t_1, is the portion of the input SPP wave that directly propagates into the straight waveguide output of the corresponding T-junction without entering the stub [Figure 2.11(a)]. However, the second term gives the contribution from the input SPP wave that enters the stub and then exits to the main waveguide. This term has been derived by the summation of all the transient portions of the incident SSP wave infinitely bouncing back and forth inside the stub to obtain the stationary response [Figure 2.11(b)]. The same argument holds for Eq. (2.2) in which the first term r_1 is the reflection from the left port of the corresponding T-junction, and the second term is the portion of the SPP wave in the stub that is emitted to the left.

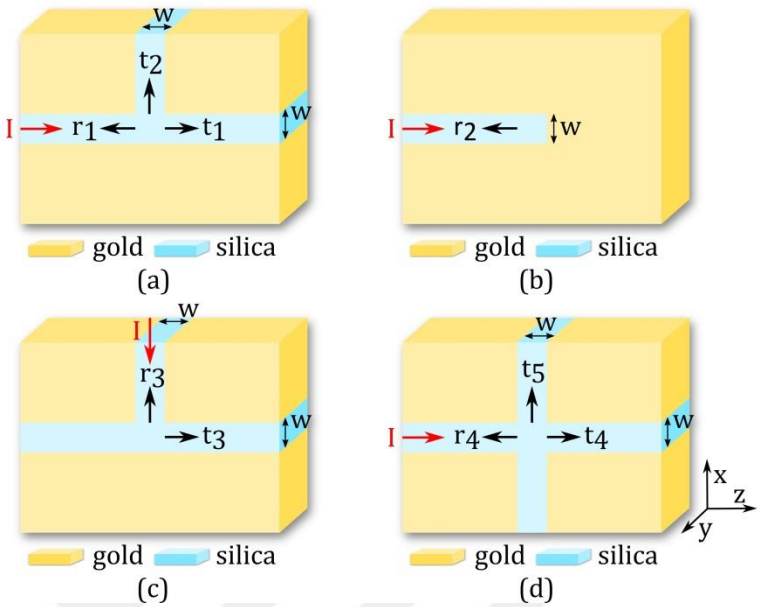

Figure 2.9 Two-dimensional: (a) T-junction with input from the left, (b) terminated waveguide, (c) T-junction with input from the top, (d) X-junction.

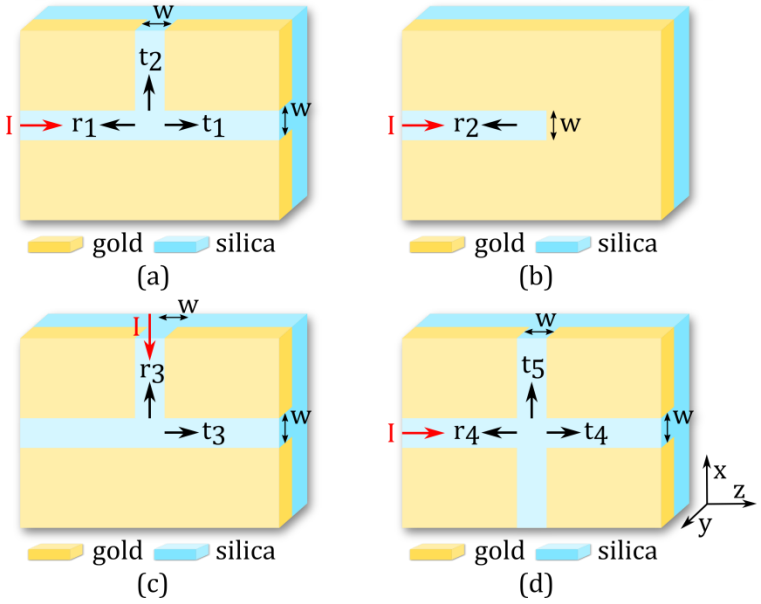

Figure 2.10 Three-dimensional: (a) T-junction with input from the left, (b) terminated waveguide, (c) T-junction with input from the top, (d) X-junction.

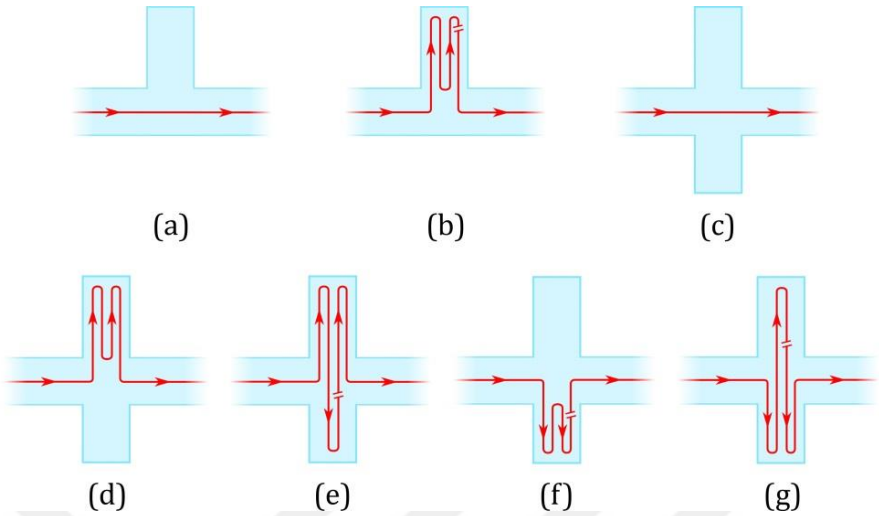

Figure 2.11 SPP wave scattering pathways in (a-b) single-stub resonator, (c-g) double-stub resonator.

Similarly, scattering matrix theory has been employed in the derivation of the complex transmission (TDS) and reflection (RDS) amplitudes of the 2D double-stub resonator by deconstructing the DS resonator as a combination of two geometries: a terminated waveguide and an X-junction as sketched in Figure 2.9(b,d) and Figure 2.10(b,d) for 2D and 3D cases, respectively. For a 2D double-stub resonator of stub lengths L_1 and L_2 the complex transmission coefficient (TDS) and the complex reflection coefficient (RDS) are given by [33,38]:

$$TDS = t_4 - C \qquad (2.3)$$

$$RDS = r_4 - C \qquad (2.4)$$

where

$$C = t_5^2\,(2t_4 - 2r_4 + s_1 + s_2)/[t_4^2 - (r_4 - s_1)(r_4 - s_2)] \qquad (2.5)$$

$$s_1 = 1/r_2\, exp(-2ikL_1) \qquad (2.6)$$

$$s_2 = 1/r_2\, exp(-2ikL_2) \qquad (2.7)$$

Complex reflection and transmission coefficients of the X-junction are denoted as follows: r_4 is the reflection from the input port of the X-junction, t_4 is the transmission to

its straight output waveguide, and t_5 is the transmission to its cross output waveguides which due to symmetry are identical [Figure 2.9(d) and Figure 2.10(d)].

Similar to the single-stub resonator, the Eq. (2.3) and Eq. (2.4) have been derived by assuming the incident SPP wave undergoing five different pathways depicted in Figure 2.11(c-g) and described as follows: Figure 2.11(c) shows the portion of the incident SPP wave that directly propagates through the X-junction, Figure 2.11(d) shows the portion of the incident SPP wave that enters the upper stub, bounces there multiple times and emits out to the right of the input waveguide, Figure 2.11(e) shows the portion of the incident SPP wave that enters the upper stub and bounces back and forth in the combined resonator of length L_1+w+L_2 and then emits out to the right of the input waveguide, similarly, Figure 2.11(f) shows the portion of the input SPP wave that enters the lower stub, bounces there multiple times and emits out to the right of the input waveguide, finally Figure 2.11(g) shows the portion of the input SPP wave that enters the lower stub and bounces back and forth in the combined resonator of length L_1+w+L_2 and then emits out to the right of the input waveguide.

In the literature, only the closed-form formulas for transmission of SS and DS resonators have been provided [30,33]. We extended the idea and we obtained the closed-form formulas for their reflection given in Eq. (2.2) and Eq. (2.4) (see Appendices A and B for the detailed derivations of these formulas).

2.3 Simulation Model

Equations (2.1)-(2.4) enable us to predict and investigate the properties of plasmonic single-stub and double-stub resonators without running numerical simulations. This is particularly of importance in 3D structures which require more simulation time and memory. Furthermore, the equations provide additional insight into the operational principles of SS and DS resonators.

We used the commercial software package Lumerical FDTD Solutions [45] for numerical simulations of our structures. To utilize Eqs. (2.1)-(2.4) first we need to extract all the complex reflection and transmission coefficients of the relevant 2D and 3D geometries

[Figure 2.9(a-d) and Figure 2.10(a-d)]. The methodology for obtaining the complex reflection and transmission coefficients of these structures is illustrated in Figure 2.12(a-d) [47]. The reflection and transmission coefficients of SS and DS resonators are extracted in a similar way as shown in Figure 2.12(f-g).

To allow waveguide modes to completely form and to avoid higher order modes that might be excited upon reflection or scattering from junctions, in both 2D and 3D simulations SPPs are collected sufficiently away from the waveguide junctions. Therefore in both 2D and 3D simulations we set our ports (P_1, P_2, P_3, P_4), d_1=1 μm away from junctions (J_1, J_2, J_3, J_4) and by defining a set of point time monitors (PTM) within d_2=0.4 μm from ports [Figure 2.12(a-g)] we collect time varying magnetic fields from each time monitor and then perform FFT to obtain the frequency-domain response of each PTM. We calculate the complex reflection and transmission coefficient for each point time monitor as

$$t = \frac{H_2^-}{H_1^+} \qquad (2.8)$$

$$r = \frac{H_1^+ + H_1^-}{H_1^+} - 1 = \frac{H_1^-}{H_1^+} \qquad (2.9)$$

Frequency-domain values of the fields are substituted into these equations and the incident SPP wave, H_1^+, which is used as normalization is obtained by running a separate simulation for each of the 2D and 3D straight waveguides [Figure 2.12 (a)].

In 2D simulations point time monitors are distributed in a *xy*-plane however in 3D simulations they are distributed in a *xyz*-volume. These monitors are located precisely in input and output ports such that each time monitor a distance *d* away from the input port has an equivalent time monitor a distance *d* away from the output port. After evaluating the reflection and transmission coefficients for each PTM and transforming them toward the location of the ports they should result in almost equal values; this ensures that simulation is setup correctly. The transformed reflection and transmission coefficients at the location of the ports are averaged and then transformed to the location of the junctions to compensate propagation losses and to obtain the pure reflection and transmission response of the junction.

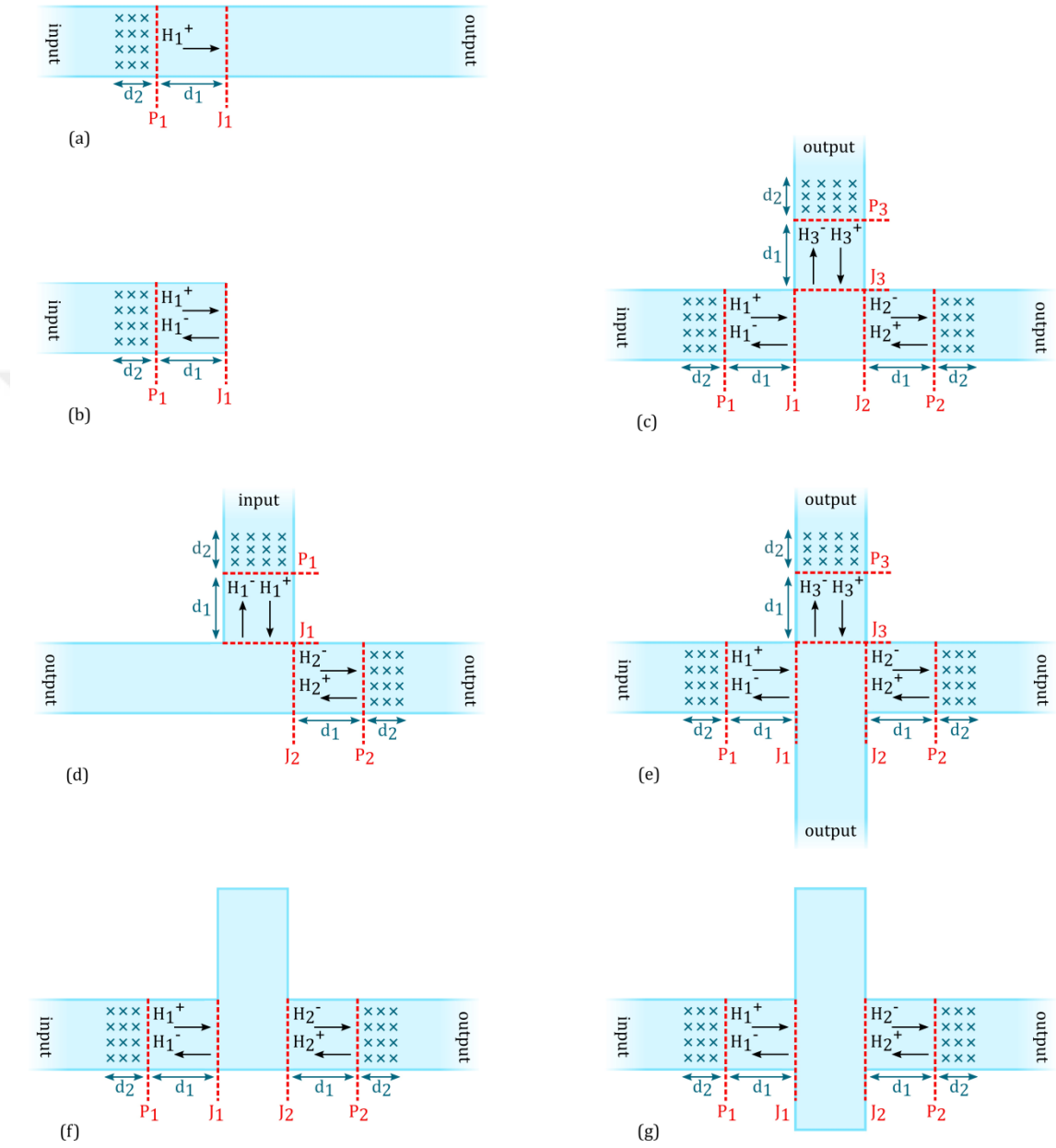

Figure 2.12 Extraction of (a) incident wave, (b) reflection from terminated waveguide, (c) reflection and transmission coefficients of T-junction with input from the left, (d) reflection and transmission coefficients of T-junction with input from the top, (e) reflection and transmission coefficients of X-junction , (f) reflection and transmission coefficients of single-stub resonator, (g) reflection and transmission coefficients of double-stub resonator.

In 2D simulations we used a uniform mesh of 2 nm in all directions and in 3D simulations we used a uniform override mesh of size 5 nm in a *xyz*-volume surrounding input and stub waveguides and non-uniform mesh elsewhere. To further check the

subtleties of the PTM method we verified its results with the results obtained with FDTD Solutions built-in Mode Expansion monitors (see Appendix C for the comparison of the results).

It is worth noting that all the reflection and transmission coefficients defined in Eqs. (2.1)-(2.4) use the propagation constant k with different values for 2D and 3D waveguides.

Amplitude of the evaluated complex reflection and transmission coefficients: r_1, r_2, r_3, r_4, and t_1, t_2, t_3, t_4, t_5 for wavelength interval 0.8-2.3 μm are shown and compared for 2D and 3D cases in Figure 2.13(a-d) and Figure 2.14(a-e). The phase information of the corresponding coefficients are also shown and compared in Figure 2.15(a-d) and Figure 2.16(a-e).

We used "stretched coordinate" PML with default settings in all of our simulations with mesh refinement C*onformal Variant 0*. We took complex conjugate of the FFT results calculated with MATLAB to match with numerical results of FDTD Solutions due to the different sign conventions that MATLAB and Lumerical use in FFT calculation.

We used complex propagation constant obtained by expansion monitors of FDTD Solutions in all our further analysis in this thesis especially for transforming the port results to the junctions.

The comparison reveals that according to Figure 2.13(a-d) there is rather small difference among the amplitudes of the reflection coefficients in 2D and 3D cases except for the reflection from the terminated waveguide as shown in Figure 2.13(b). 2D terminated waveguide acts almost like a perfect mirror and reflects back all the incident SPP wave, however, 3D terminated waveguide reflects less than 50% of the incident wave and most of the incident SPP is radiated out to the substrate and cladding via scattering.

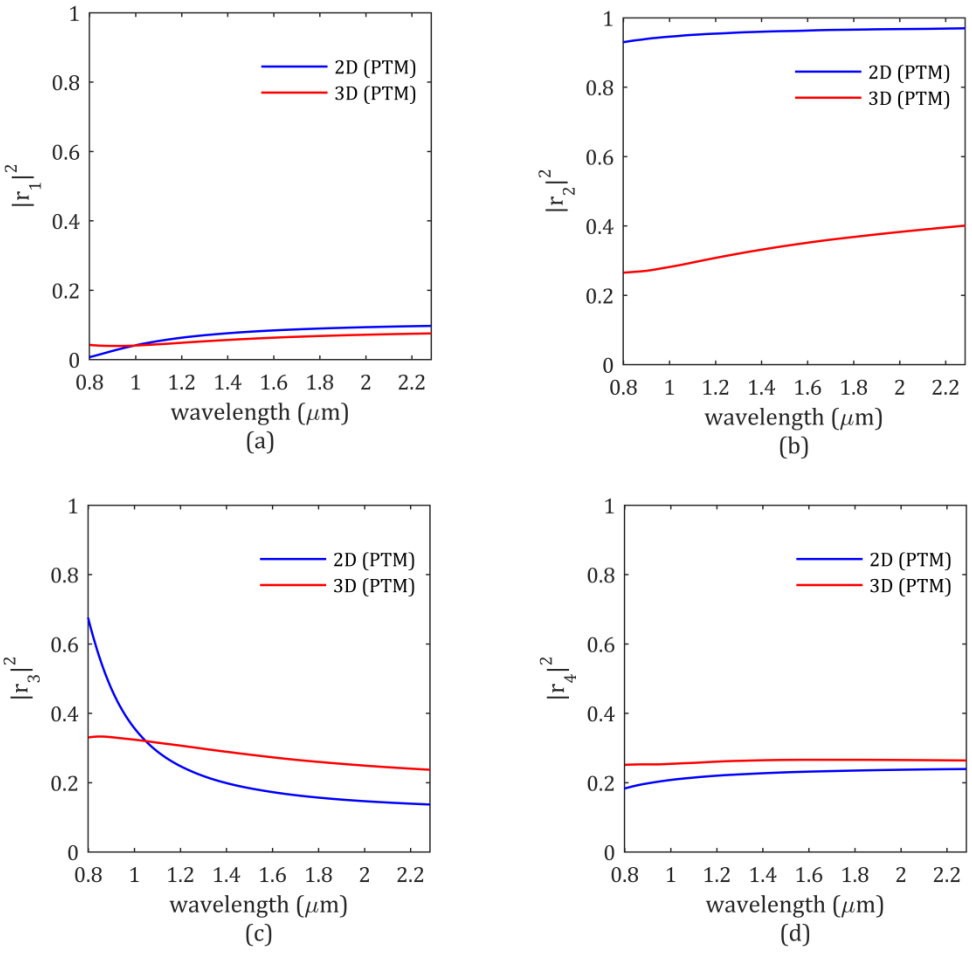

Figure 2.13 Comparing the amplitudes of the 2D and 3D reflection coefficients calculated by PTM method.

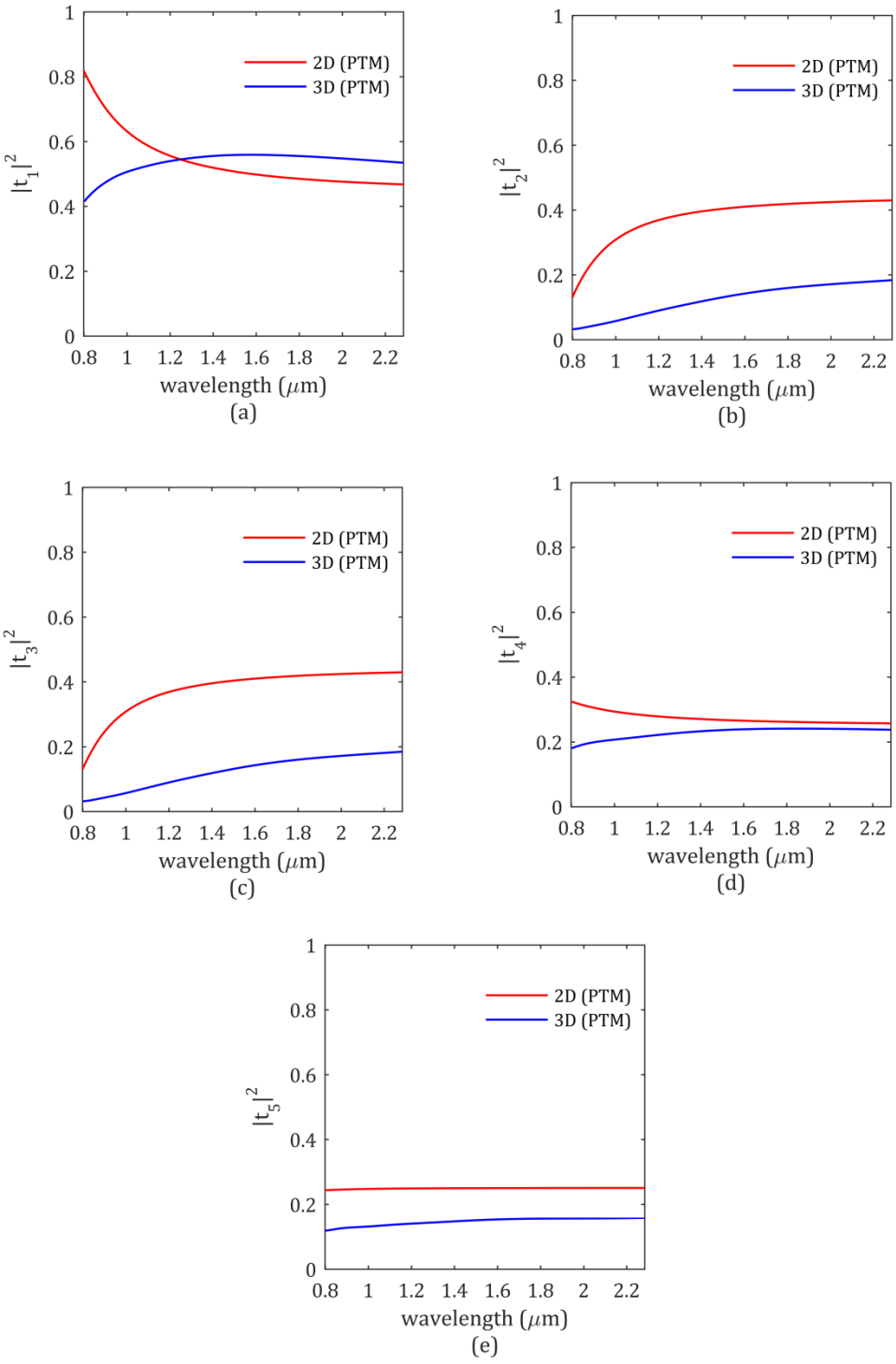

Figure 2.14 Comparing the amplitudes of the 2D and 3D transmission coefficients calculated by PTM method.

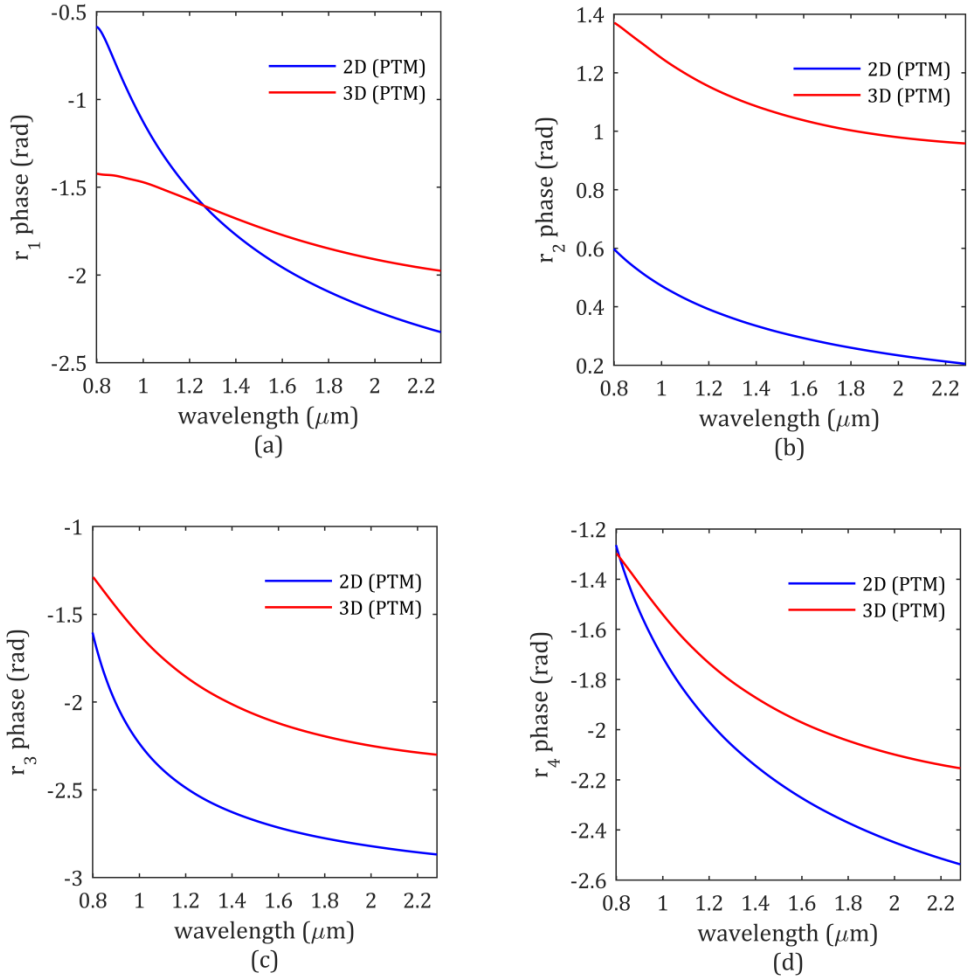

Figure 2.15 Comparing the phases of the 2D and 3D reflection coefficients calculated by PTM method.

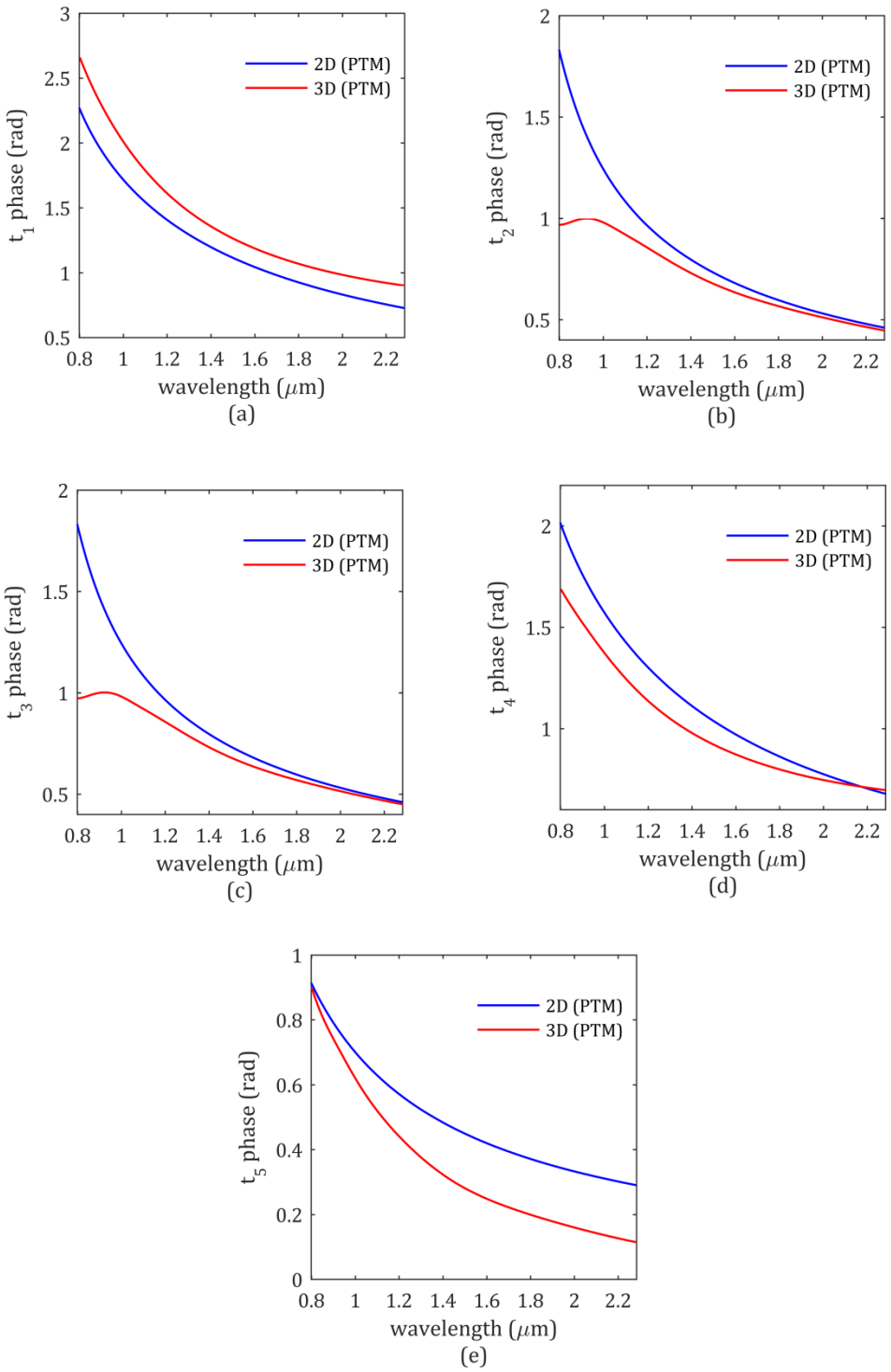

Figure 2.16 Comparing the phases of the 2D and 3D transmission coefficients calculated by PTM method.

2.4 Simulation Results

2.4.1 Single-stub resonators

In this section we give the guidelines for designing the 2D and 3D plasmonic single-stub resonators employing semi-analytical Eq. (2.1) obtained by scattering matrix theory. By plugging the complex reflection and transmission coefficients of the geometries sketched in Figure 2.9(a-c) and Figure 2.10(a-c) at 1550 nm into Eq. (2.1), we plot the 2D and 3D $|\mathrm{TSS}|^2$ versus stub length L as shown in Figure 2.17. These graphs give us the resonant lengths at 1550 nm and assist us in selecting the stub lengths that result in either dips or peaks in the transmission of 2D or 3D SS resonator at an operating wavelength of 1550 nm. The variations in the single-stub spectrum as a function of L are due to the interference of the two SPP waves undergoing different pathways: the SPP wave that goes directly through the junction and the ones that bounce within the stub [Figure 2.11(a,b)].

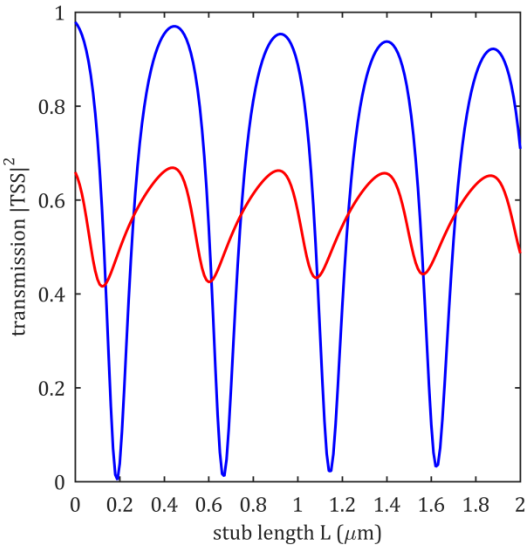

Figure 2.17 Power transmission coefficient $|\mathrm{TSS}|^2$ versus stub length L, for 2D (blue curve) and 3D (red curve) single-stub resonator.

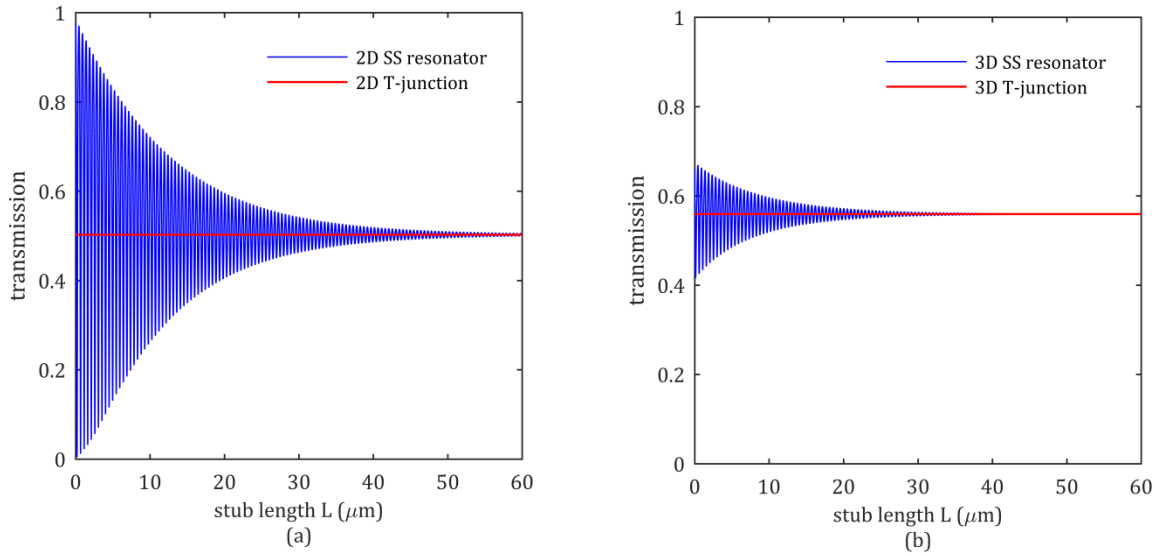

Figure 2.18 Asymptotic behavior of (a) 2D SS resonator, (b) 3D SS resonator, as stub length goes to infinity.

To further check the validity of our numerical results, in Figure 2.18 we show that the transmission of 2D and 3D SS resonators at 1550 nm asymptotically approaches to the transmission t_1 of 2D and 3D T-junctions (with input from the left) at 1550 nm as stub length goes to infinity.

Similarly, by plugging the relevant 2D and 3D complex reflection and transmission coefficients obtained for the wavelength interval 0.8-2.3 μm into Eq. (2.1), we plot the wavelength response for the first four resonant stub lengths corresponding to a dip or a peak in the transmission spectrum at 1550 nm for 2D (Figure 2.19) and 3D (Figure 2.20) SS resonators. The specifications of the resulting SMT-predicted spectra for 2D and 3D single-stub resonators are listed Table 2.1 and Table 2.2. From the information provided in these tables we see that the spectra which feature dips have less FWHM compared to the spectra that feature peaks.

We found that in both of the 2D and 3D spectra with either dips or peaks, longer stub lengths resulted in narrower FWHM but slightly lower contrast. This means that there is a tradeoff between the device footprint and its optimum performance. This observation originates from the fact that a single-stub resonator can be assumed as a Fabry- Perot resonator with partially reflecting mirrors of fixed reflection coefficients r_1 and r_2. In a

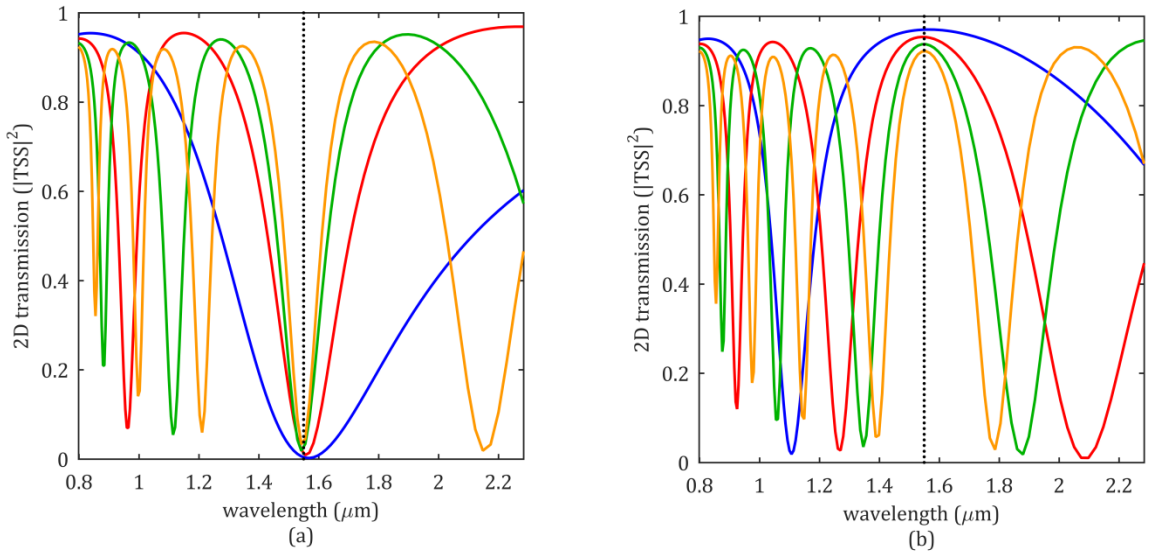

Figure 2.19 (a) First four resonant orders corresponding to a dip in 2D SS resonator spectrum at 1550 nm (blue: L=190 nm, red: L=670 nm, green: L=1140 nm, yellow: L=1620 nm), (b) first four resonant orders corresponding to a peak in 2D SS resonator spectrum at 1550 nm (blue line: L=450 nm, Red: L=920 nm, green: L=1400 nm, yellow: L=1880 nm).

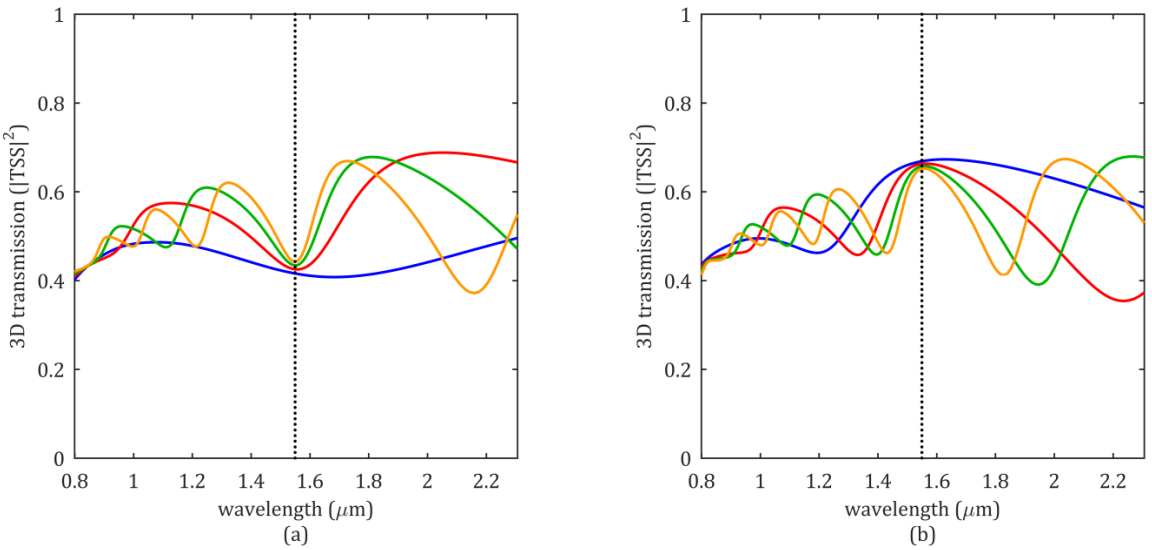

Figure 2.20 (a) First four resonant orders corresponding to dip in 3D SS resonator spectrum (blue: L=120 nm, red: L=600 nm, green: L=1080 nm, yellow: L=1560 nm), (b) first four resonant orders corresponding to a peak in 3D SS resonator spectrum (blue: L=440 nm, red: L=910 nm, green: L=1390 nm, yellow: L=1870 nm).

L_{dips} (nm)	FWHM (nm)	Q-factor
190	800	1.96
670	270	5.75
1140	170	9.28
1620	120	12.47
L_{peaks} (nm)	FWHM (nm)	Q-factor
450	1101	1.42
920	577	2.67
1400	376	4.14
1880	279	5.58

Table 2.1 Spectrum specifications of first four resonant orders resulting in dip or peak in 2D single-stub resonator transmission power.

L_{dips} (nm)	FWHM (nm)	Q-factor
120	------	------
600	467	3.33
1080	260	5.97
1560	182	8.5
L_{peaks} (nm)	FWHM (nm)	Q-factor
440	------	------
910	907	1.73
1390	550	2.88
1870	400	3.9

Table 2.2 Spectrum specifications of first four resonant orders resulting in dip or peak in 3D single-stub resonator transmission power.

Fabry-Perot resonator the resonator spectral bandwidth is directly proportional to the free spectral range and is inversely proportional to the finesse. Finesse factor is given in terms of the mirror reflectivity which is constant in our case. In a Fabry-Perot resonator by increasing the resonator thickness (equivalent to stub length here), free spectral range as well as frequency bandwidth (FWHM) decreases [48], accordingly, by increasing the stub length the spectral bandwidth decreases.

It is also evident (Figure 2.17) that the transmission contrast, i.e. the difference between minimum and maximum power levels which is a requisite for having high performance

switches and filters is far less in 3D SS resonator than the 2D SS resonator. This quantity varies between 0.43 and 0.67 for 3D SS resonator while for a 2D SS resonator the correspondent value varies between nearly 0 and 0.92. Furthermore, the 2D and 3D SS resonators which are designed to be equivalent at 1550 nm show peaks in their spectra for almost the same stub lengths but the dip in their spectra occurs for different stub lengths. The peak values corresponding to different stub lengths amount almost to the transmitted powers of the straight waveguides (L=0) in both 2D and 3D cases. However, the dip values in the 2D case almost reach zero and in the 3D case it reaches 0.43.

The low contrast and the shift in dip resonances in the 3D case can be explained by understanding the operational principle of the single-stub resonator. To understand the operational mechanism of single-stub resonators, in Figure 2.21(a) we show the transmitted power of a 2D single-stub resonator versus stub length L at 1550 nm (blue line) along with two different phase plots, all obtained by scattering matrix theory: a) phase difference between the SPP wave passing directly through the junction and the SPP wave coming back from the stub (yellow line) which in fact is the phase difference between the first and second terms of the Eq. (2.1), b) round-trip phase shift (red line) that the SPP wave entering the stub gains in the stub given by: $\varphi_{r_2}(\lambda) + 2k(\lambda)L + \varphi_{r_1}(\lambda)$, where $\varphi_{r_2}(\lambda)$ is the phase shift that the SPP wave experiences upon reflection from the terminated end of the stub, $\varphi_{r_1}(\lambda)$ is the phase shift experienced by the SPP wave as it reflects from the T-junction with input from the top, and $2k(\lambda)L$ is the round-trip phase shift that the SPP wave gains as it propagates along a stub of length L.

The phase analysis of the two SPP waves propagating along two different pathways in a single-stub resonator [Figure 2.21 (a,b)] reveals that when the phase difference between the two SPP waves (yellow line) is 2π (π) there is a peak (dip) in the transmitted power. Moreover, when there is a dip in the transmission the round-trip phase gained by the SPP wave inside the stub is 2π. Therefore, in the formation of a dip, the SPP wave that enters the stub undergoes constructive interference and bounces multiple times inside the stub before coming out. In this case due to the open nature of 3D SSR the SPP wave suffers more from the radiation loss compared to the case when it does not undergo constructive

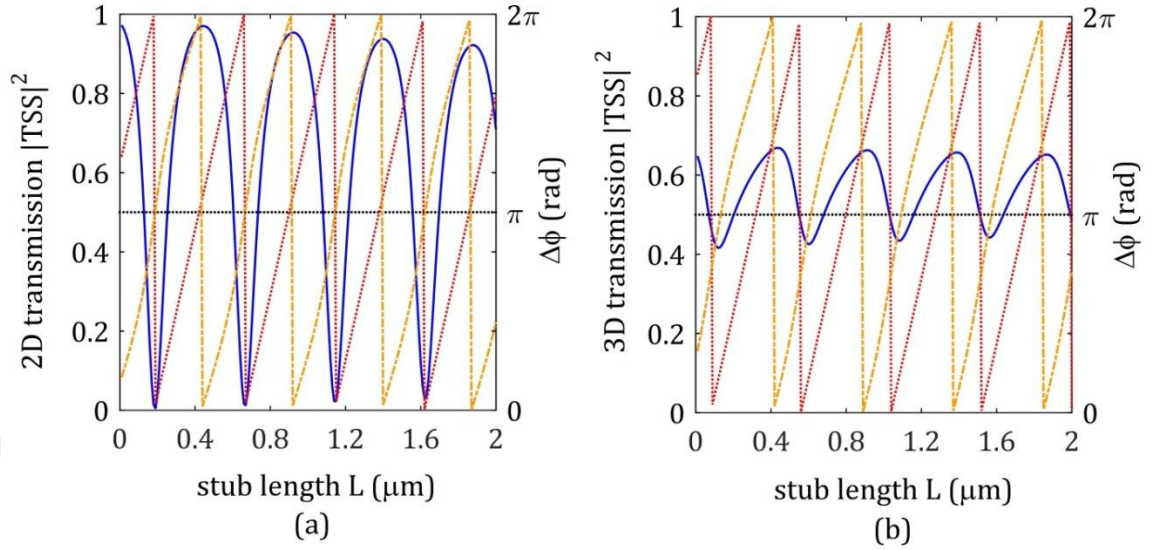

Figure 2.21 Relation between the variation of the transmission amplitude (blue line) and the evolution of phases (red and yellow lines) versus stub length *L* in (a) 2D SS resonator, (b) in 3D SS resonator.

interference inside the stub. Consequently, the attenuated SPP wave leaving the stub has smaller amplitude compared to the SPP wave that directly passes through the junction which results in a poor destructive interference between the two waves and thus low contrast despite being out of phase.

The main reason behind the shift in the resonant lengths corresponding to dips in 3D case with respect to the 2D case is due to the fact that, when there is a dip, the SPP wave circulating in the stub satisfies the resonance condition given by $\varphi_{r_2}(\lambda) + 2k(\lambda)L + \varphi_{r_1}(\lambda)$ (red line in Figures 2.21). Comparison of the phases of r_1 and r_2 coefficients in 2D and 3D cases [Figure 2.15(a,b)] reveals that in 3D, $\varphi_{r_2}(\lambda) + \varphi_{r_1}(\lambda)$ contribution is larger compared to 2D, hence a shorter *L* value suffices to reach the resonance.

The obtained semi-analytic results reveal the low capability of 3D SS resonator for being used in switching and filtering purposes compared to 2D SS resonators. We also verified the prediction of scattering matrix theory with numerical FDTD simulations. We simulated 2D and 3D SS resonators with stub lengths both set to the third resonant length of the 3D SS resonator at 1550 nm, i.e. L=1.39 μm as predicted by SMT in Table 2.2. The simulation results shown in Figure 2.22(a,b), verify the predictions of SMT and its applicability to the 3D structures.

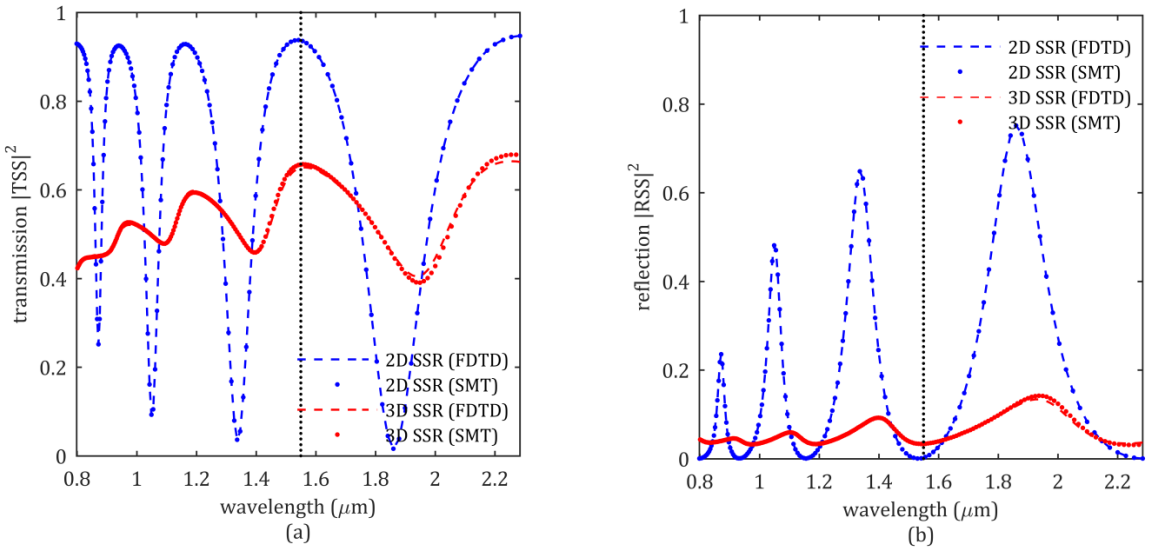

Figure 2.22 (a) Transmission, (b) reflection coefficients of 2D and 3D SS resonators with stub length L=1390 nm predicted by scattering matrix theory and verified with numerical FDTD simulations.

2.4.2 Double-stub resonators

Similar to the single-stub resonator, by substituting the complex reflection and transmission coefficients at 1550 nm of the relevant geometries [Figure 2.9(b,d) and Figure 2.10(b,d)] into Eq. (2.3) we plot the power transmission coefficient, $|TDS|^2$, for the 2D and 3D double-stub resonators versus stub lengths L_1 and L_2 both ranging from 0 to 2 μm as shown in Figure 2.23(a,b), respectively.

These transmission maps depict the resonant orders for which there is either a dip or a peak in the transmission power spectrum of double-stub resonators and thus are helpful in choosing the appropriate stub lengths depending on the application.

Due to the symmetry of the geometry, we focus only on the length pairs that lie above the L_1=L_2 line, shown by the white line. The resonant orders corresponding to peaks (dips) in transmission are denoted by black (red) dots and the letter P (D).

In the double-stub resonators the incident SPP wave has the opportunity to propagate through five different pathways as illustrated in Figure 2.11(c-g). Variation of the transmission power versus stub lengths originates from the fact that for some length pairs the five SPP waves interfere constructively (destructively) to form a peak (dip) in the

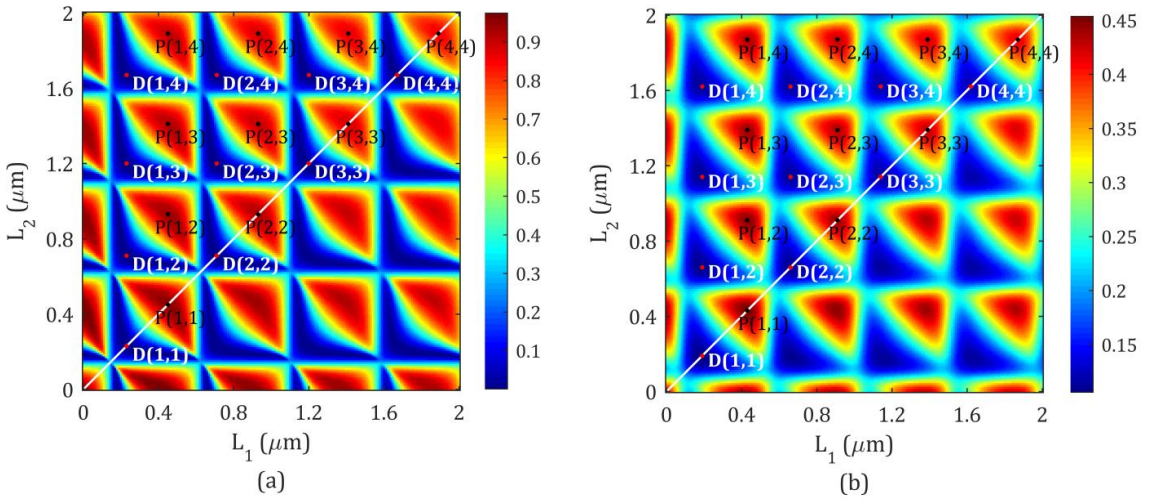

Figure 2.23 Power transmission coefficient $|TDS|^2$ versus L_1 and L_2 at 1550 nm for (a) the 2D DS, (b) the 3D DS resonator.

resulting transmission power spectrum. Moreover, in the $|TDS|^2$ plots, L_1=0 and L_2=0 axes, which due to symmetry are identical, give the power transmission spectrum of the single-stub resonator at 1550 nm with stub length ranging from 0 to 2 μm. It is clear that along these axes, the length interval for which we have a dip in the transmission spectrum of the SS resonator is less than the length interval for which we have a peak. As tuning of stub length is analogous to the tuning of wavelength this further proves that spectral FWHM of the SS resonator, which features a dip in transmission, is narrower than the one that features a peak in the transmission.

In Figure 2.24(a,b) we plot the SMT-predicted spectra of the 2D double-stub resonator $|TDS|^2$ for the first four resonant orders of equal stub lengths that result in a peak [denoted as P(1,1), P(2,2), P(3,3), P(4,4) in Figure 2.23(a)] or a dip [denoted as D(1,1), D(2,2), D(3,3), D(4,4) in Figure 2.23(a)], respectively. Similarly, in Figure 2.25(a,b) we show the predicted spectra of the equivalent resonant orders for the 3D double-stub resonator. Similar to 3D single-stub resonators, the peak amplitude of the 3D DS resonator is almost half of the 2D DS resonator and its contrast is lower compared to the 2D DS resonator.

Table 2.3 and Table 2.4 list the equal resonant length pairs that result in either a dip or a

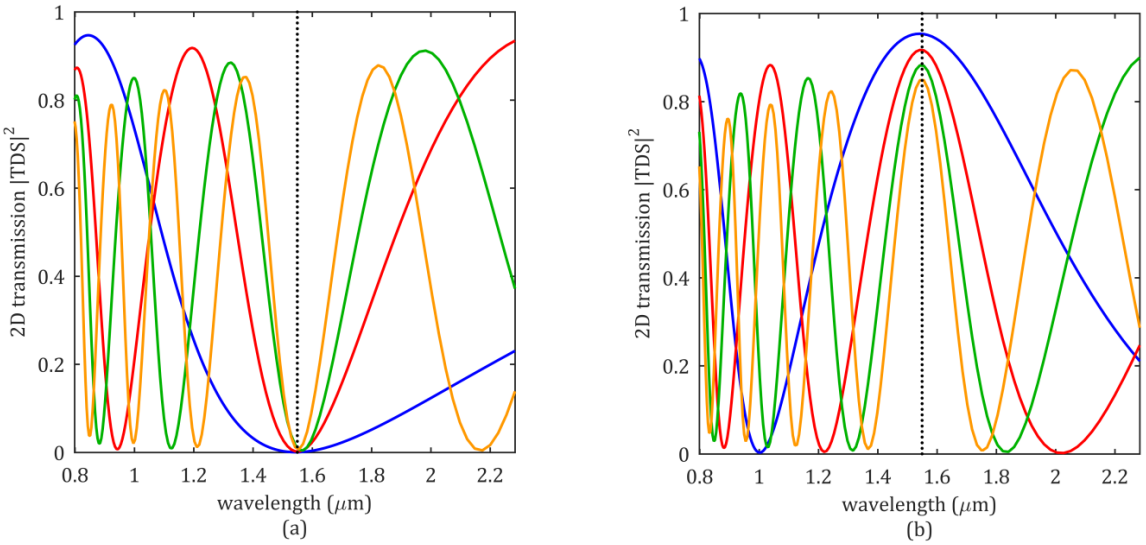

Figure 2.24 (a) Blue line: L_1=L_2=0.23 μm, red line: L_1=L_2=0.71 μm, green line: L_1=L_2=1.2 μm, yellow line: L_1=L_2=1.67 μm. (b) blue line: L_1=L_2=0.45 μm, red line: L_1=L_2=0.93 μm, green line: L_1=L_2=1.41 μm, yellow line: L_1=L_2=1.89 μm. Black dotted line specifies the location of the operating wavelength 1550 nm.

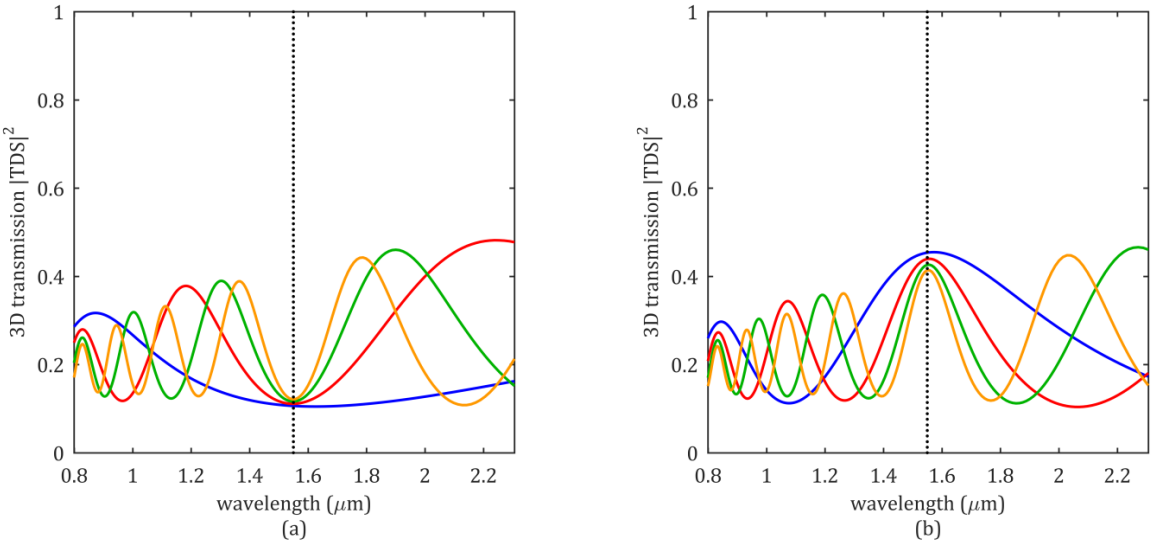

Figure 2.25 (a) Blue line: L_1=L_2=0.19μm, red line: L_1=L_2=0.66 μm, green line: L_1=L_2=1.14 μm, yellow line: L_1=L_2=1.62 μm. (b) blue line: L_1=L_2=0.43 μm, red line L_1=L_2=0.91 μm, green line: L_1=L_2=1.39 μm, yellow line: L_1=L_2=1.879 μm. Black dotted line specifies the location of the operating wavelength 1550 nm.

$L_1=L_2=L_{dip}$ (nm)	FWHM (nm)	Q-factor
230	1182	1.30
710	515	3.02
1200	308	5.09
1670	217	7.16
$L_1=L_2=L_{peak}$ (nm)	FWHM (nm)	Q-factor
450	821	1.88
930	397	3.90
1410	264	5.83
1890	199	7.83

Table 2.3 Spectrum specifications of first four resonant orders resulting in dip or peak in 2D double-stub resonator power transmission.

$L_1=L_2=L_{dip}$ (nm)	FWHM (nm)	Q-factor
190	------	------
660	586	2.64
1140	339	4.58
1620	238	6.51
$L_1=L_2=L_{peak}$ (nm)	FWHM (nm)	Q-factor
430	880	1.79
910	426	3.66
1390	288	5.41
1870	221	7.04

Table 2.4 Spectrum specifications of first four resonant orders resulting in dip or peak in 3D double-stub resonator power transmission.

peak in the 2D and 3D DS resonators along with the specifications of their corresponding spectra obtained by scattering matrix formalism. The comparison reveals that similar to the single-stub resonators the resonant orders corresponding to peaks (at 1550 nm) happen almost at the same stub lengths regardless of being 2D or 3D structures; however the resonant orders corresponding to dips (at 1550 nm) happen at slightly different length pairs. Comparison of the results provided in Table 2.2 for 3D SS resonator and Table 2.4 for 3D DS resonator reveals that single-stub and double-stub resonators show a peak in their transmission at the same stub lengths, however, double-stub resonators featuring a peak (dip) in their spectra have narrower (wider) FWHM and thus higher (lower) Q-factor compared to their corresponding single-stub resonators. The comparison of Figure

2.20(b) and Figure 2.25(b) also shows that double-stub resonators provide us with better contrast compared to single-stub resonators.

Our analysis shows that in both types of resonant orders (dips or peaks) in both 2D and 3D DS resonators, by increasing the stub length the FWHM of the resulting spectrum decreases. This again originates from the Fabry-Perot effect already explained in section 2.4.1.

It is worth noting that the same behavior occurs for a double-stub resonator of unequal stub lengths such that by keeping one stub length fixed and increasing the length of the second stub the FWHM decreases (not shown). For instance, P(1,3) has narrower FWHM compared to the P(1,2). However, in a DS resonator of unequal stub lengths some extra lobes and shoulders appear in the spectrum unlike in a DS resonator of equal lengths. Therefore we inspected only DS resonators of equal stub lengths which produce neat and uniform spectra.

Starting from second resonant order of equal length pairs P(2,2) denoted as point *A* in Figure 2.26(a,b) and moving away from this peak point along the symmetry axis, which ensures the equality of the single-stub lengths, in Figure 2.26(c,d) we show the tunability of the resonant wavelength in both 2D and 3D DS resonators, respectively. As expected, by increasing the stub lengths the resonant wavelength undergoes a red shift.

Further we found that, while tuning within each resonant order the spectrum FWHM remains almost unchanged however the change in FWHM is far more from one resonant order to another.

Utilizing the transmission maps of Figure 2.23(a,b) we can further locate the points that result in the plasmonic analogue to the electromagnetically induced transparency (PIT) phenomenon [38]. To observe this phenomenon we should start from an equal stub length pair with the DS resonator and the corresponding SS resonators simultaneously having a dip in the transmitted power [49]. These points are depicted with white dots in Figure 2.27(a,b) for 2D and 3D DS resonators, respectively. The PIT effect is observed by breaking the symmetry of the DS resonator which is possible by making stub lengths slightly unequal while keeping the total length constant. Asymmetric DS resonators of

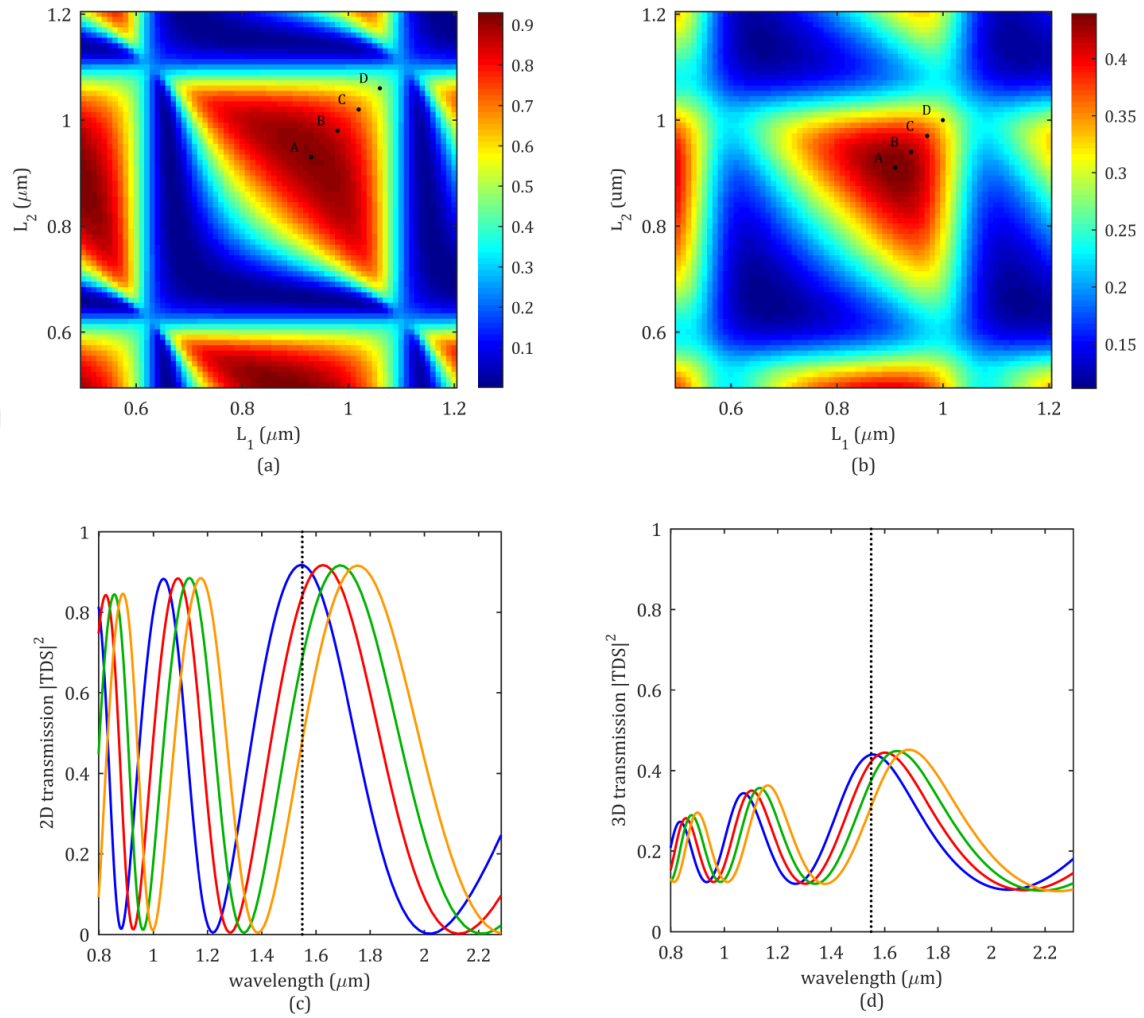

Figure 2.26 Four sets of equal-length pairs chosen from second resonant order along the symmetry axis of the transmission map of (a) 2D DS resonator, (b) 3D DS resonator. Transmission power spectra of (c) 2D DS resonator for length pairs A: L_1=L_2=930 nm (blue line, λ_{peak}=1550 nm), B: L_1=L_2=980 nm (red line, λ_{peak}=1626 nm), C: L_1=L_2=1020 nm (green line, λ_{peak}=1690 nm), D: L_1=L_2=1060 nm (yellow line, λ_{peak}=1752 nm), (d) 3D DS resonator for length pairs A: L_1=L_2=910 nm (blue line, λ_{peak}=1550 nm), B: L_1=L_2=940 nm (red line, λ_{peak}=1600 nm), C: L_1=L_2=970 nm (green line, λ_{peak}=1650 nm), D: L_1=L_2=1000 nm (yellow line, λ_{peak}=1690 nm).

slightly unequal stub lengths allow the formation of an asymmetric mode in the combined resonator of length L_1+w+L_2 (w being the width of the waveguide) in addition to the symmetric mode and pave the way for their coupling which is the origin of the Fano-shaped transparency window in PIT phenomenon [37].

Taking into account the fact that the resonant wavelength in the PIT phenomenon, for

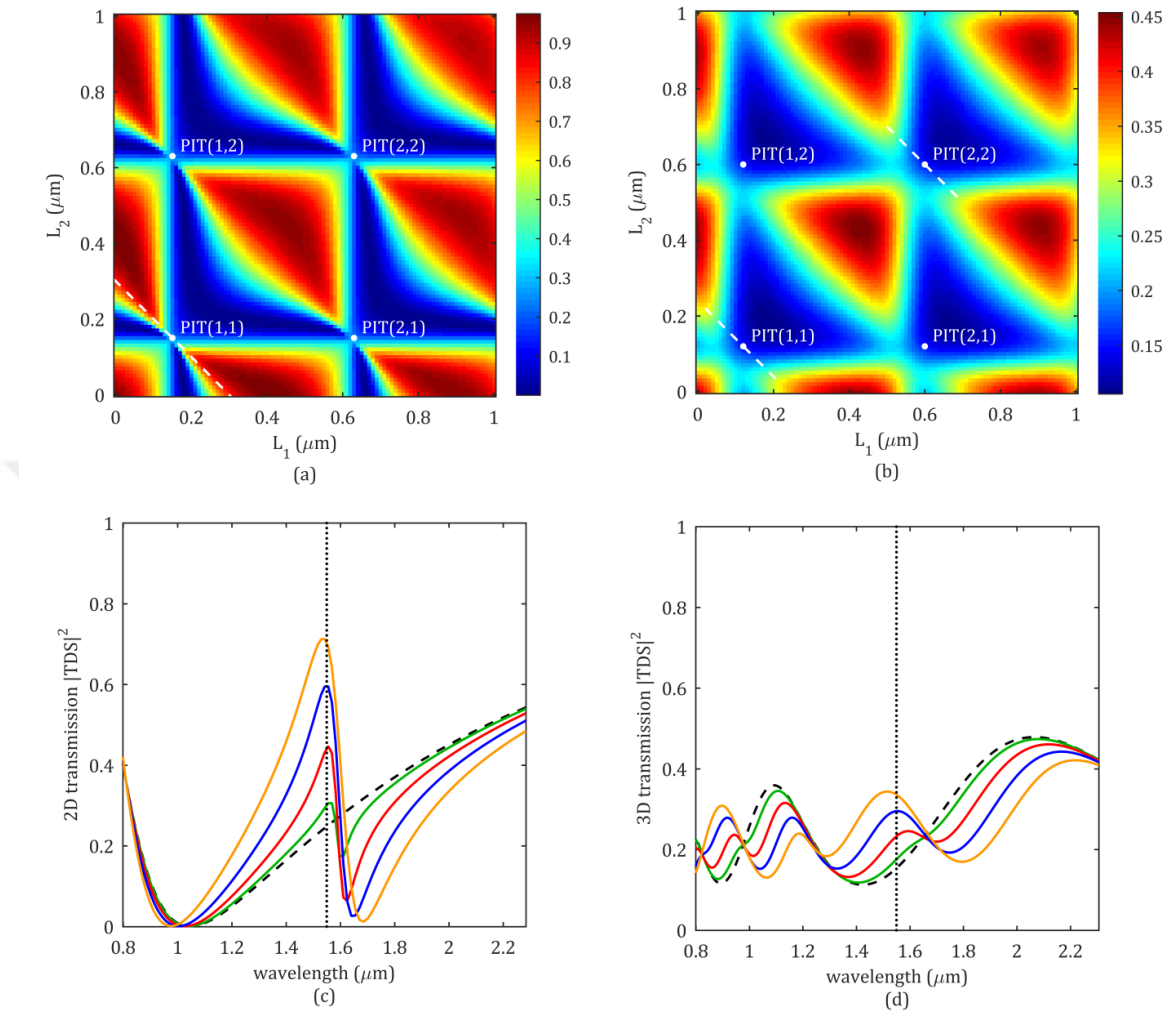

Figure 2.27 Asymmetric PIT-type spectra (a) 2D DS resonator :black dashed: (L_1, L_2)=(150,150) nm, green: (L_1, L_2)=(160,140) nm, red: (L_1, L_2)=(170,130) nm, blue: (L_1, L_2)=(180,120) nm, yellow: (L_1, L_2)=(190, 110) nm, (b) 3D DS resonator: black dashed: (L_1, L_2)=(600,600) nm, green: (L_1, L_2)= (630, 570) nm, red: (L_1, L_2)= (660,540) nm, blue: (L_1, L_2)=(690,510) nm, yellow: (L_1, L_2)=(720, 480) nm.

which a peak in the transmission appears, is proportional to the combined resonator length, by increasing one stub length by an amount of *dL* and decreasing the other stub length by the same amount we can keep the total resonator length and thus PIT resonant wavelength fixed. This is possible by moving along the dashed white lines [Figure 2.27(a,b)] which pass through PIT(1,1) and PIT(2,2) resonant orders and make an angle of 45° with horizontal and vertical axes.

Starting from PIT(1,1) and moving along dashed white line [Figure 2.27(a)] with steps of *dL*=10 nm in Figure 2.27(c) we show the spectra of the 2D DS resonator for four sets of

unequal length pairs. The dashed black curve gives the transmission of the 2D DS resonator of equal stub length which due to the finite and rather wide widths of our reference plasmonic MDM waveguide is not zero [49]. We found that by increasing *dL* the asymmetry factor remains the same but transmission amplitude increases [37].

Starting from PIT(1,1) for 3D DS resonators [Figure 2.27(b)] with steps of *dL*=30nm we tried the same approach in 3D DS resonator, however we could not observe any reasonable asymmetric Fano-shaped transparency window for this PIT resonant order. We tried PIT(2,2) and the resulting spectra for four different sets of unequal stub lengths are shown in Figure 2.27(d). We conclude that observing PIT in 3D DS resonators is almost impossible which might be due to the open nature of 3D slot waveguide that does not allow the formation of well-defined junction resonator modes [37]. Although we could not observe PIT phenomenon in the studied 3D double-stub resonator, the PIT phenomenon has been observed in slightly decoupled stub pairs attached to a U-shaped 3D plasmonic waveguide [50].

2.4.3 Designing efficient terminated waveguide

2.4.3.1 Grating-terminated stubs

The SPP waves propagating through the 3D SWG-based devices not only experience radiation loss at the terminated-ends (TE) but they also experience loss as they go through the 3D junctions and sharp or curved bends. However, comparing the reflection and transmission coefficients of the 2D geometries [Figure 2.9(a-d)] with the reflection and transmission of their 3D counterparts [Figure 2.10(a-d)] shown in Figure 2.13(a-d) and Figure 2.14(a-g) reveal that the r_2 coefficient—which is the reflection from a terminated waveguide end —is far less in 3D terminated-end than in the 2D one, compared to all the other reflection and transmission coefficients. This is a sign of significant radiation loss in the 3D terminated ends. One way for increasing the r_2 coefficient is to increase the height of the metallic layer which converts the 3D slot-waveguide to MDM waveguide or adding block reflectors as high as 1 μm to the terminated ends [51,52]. Nonetheless, the latter approach not only adds complexity to the fabrication of the terminated ends but it also increases the device footprint. Therefore, our

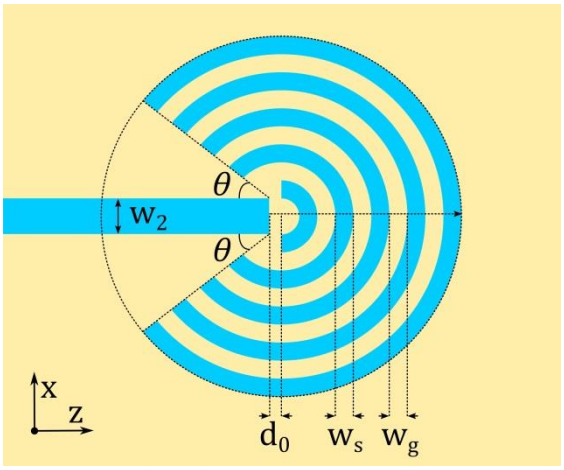

Figure 2.28 Schematic of the top-view of the circular grating reflector and its design parameters.

3D simulation results emphasize the necessity of suppressing or reducing radiation loss at the terminated ends.

At the terminated ends, the 3D slot waveguide is abruptly converted to a dielectric-metal-dielectric DMD waveguide with width equal to the height of the slot-waveguide. Due to the mismatch between the modal shapes of the slot-waveguide and DMD waveguide the SPP wave partially scatters to the cladding and substrate layers and partially is coupled to the MD and DMD modes.

One way to boost the r_2 reflection coefficient is to add a Bragg grating to the terminated end to reflect back the portion of the mode which is coupled to the DMD waveguide modes. Due to the fact that the scattered light at the end of the terminated waveguide has circular wavefronts we adapted the circular grating design in [53] to reduce the diffraction loss as the SPP wave propagates through the grating. It should be noted that this circular grating has been designed on a 220 nm silicon-on-insulator platform; however, we need to employ it in a plamonic dielectric-metal-dielectric waveguide. Therefore, in our case silicon blades will be replaced with gold blades. The structure of the circular grating with its design parameters and the input slot-waveguide, adapted into our case are shown in Figure 2.28. The widths of silica trenches and metallic blades are W_s and W_g, respectively. d_0 is the gap between the first silica trench and input waveguide to avoid merging. The angle θ is the angle between input waveguide propagation axes and end of silica trenches.

Trench terminology is assigned to the grating bar that its material is identical as the substrate and superstrate layers which is silica in our case. On the other hand, the blade terminology is assigned to a grating bar of different material which is sandwiched between substrate and superstrate layers, which is gold in our case. With these descriptions, the SPP wave passing through a silica trench can be assumed as an SPP wave that propagates through a bulk medium made of silica, on the other hand, the SPP wave passing through a gold blade resembles a SPP wave propagating in a slab dielectric-metal-dielectric DMD waveguide. Since the effective refractive index of a circular structure cannot be calculated analytically, by approximating the refractive index of the circular gold blades with the refractive index of a slab DMD waveguide, the period of the circular grating can be calculated based on the Bragg grating equation used in straight gratings given by [53]

$$\Lambda = \frac{m\lambda_c}{2n_{eff}} = \frac{m\lambda_c}{2(dc \times n_s + (1-dc) \times n_g)} \qquad (2.10)$$

where m is an integer number representing the grating order, λ_c is the Bragg wavelength which is supposed to be 1550 nm in our case, n_{eff} defined as $2(dc \times n_s + (1-dc) \times n_g)$ is the effective refractive index of the straight silica/gold grating which is used as an approximation for effective refractive index of the circular silica/gold grating.

Effective refractive index can be assumed as geometric mean between n_s and n_g with duty cycle dc serving as the weight factor. Duty cycle is defined as

$$dc = \frac{W_s}{\Lambda} \qquad (2.11)$$

To evaluate the approximate period of the circular grating for wavelength 1550 nm, we first numerically calculated the effective refractive index of the slab DMD waveguide denoted as n_g at 1550 nm with Mode Expansion monitor in FDTD Solutions which amounted to n_g=1.45763. In this calculation the width of the slab DMD waveguide is set to the height of the slot-waveguide. The refractive index of the silica trench bars is set to the refractive index of the bulk silica n_s=1.44

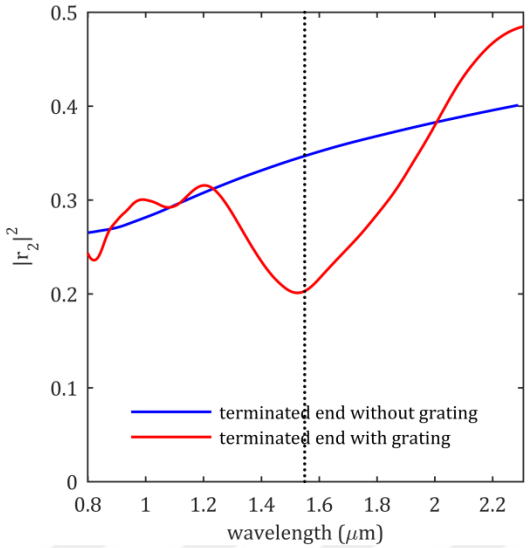

Figure 2.29 Comparison of the power reflection $|r_2|^2$ from a 3D terminated end with and without circular grating. Grating parameters are: Λ= 535 nm, dc=50%, d_0=30nm, θ=70°, N=6.

To achieve high reflectance with Bragg gratings the contrast between the refractive indices of the blades and trenches should be high enough otherwise the number of grating periods need to be increased which increases the device footprint. The calculated n_g value is very close to n_s=1.44 which is a detriment and is one of the drawbacks for achieving high contrast and thus compact gratings in plasmonic field [54].

By taking dc=50%, the first order (m=1) period of the circular grating is calculated to be Λ= 535.14 nm ~ 535 nm. By adding a circular grating to the end of terminated slot-waveguide with parameters dc=50% and thus W_s=W_g=$\Lambda/2$=267.5 nm, d_0=30 nm, θ=70°, and the number of periods N=6 , we ran a 3D FDTD simulation to numerically calculate the reflection coefficient r_2. The numerical results belonging to reflection from terminated ends with and without gratings are shown and compared in Figure 2.29.

By addition of the circular grating to the terminated end, instead of having increase in back reflection at 1550 nm there is a dip. This shows that the designed circular grating has increased the radiation loss at the terminated end and serves more like an antenna than a back reflector.

Regardless of how well the curved grating in a DMD waveguide is designed, due to the finite height of the grating blades the reflected SPP wave will suffer from radiation loss

as it propagates through them.

Since the calculated approximate value for the grating period Λ did not give us the desired result we decided to numerically sweep over the period of the grating to find the period that results in an increase in the value of r_2. We swept over grating period in the range Λ=100-500 nm with steps of Λ=100 nm and we extracted r_2 coefficient for each grating configuration. In all these simulations we set the grating parameters to: dc=50%, θ =50°, d_0=30 nm, and N=4 and the override mesh size which covered the whole grating area is initially set to 10 nm. The initial test simulations shown in Figure 2.30 reveal that to have an increase in r_2 reflection the grating period needs to be around 100nm. Therefore, we ran another set of simulations and swept over grating period in the range Λ=100-140 nm with steps of Λ=10 nm. The grating parameters are as before except N=5 and override mesh size is reduced to 5 nm. The sweeping result is shown in Figure 2.31. By increasing the grating period from 100 nm to 140 nm the resonant wavelength for which we have a peak in back reflection shifts to longer wavelengths, as expected. The black dashed curve which is the r_2 power refection from a terminated-end without grating has been shown for comparison.

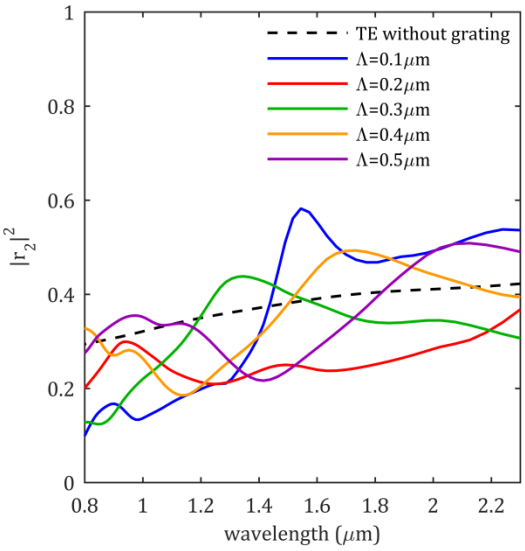

Figure 2.30 Comparision of the power reflection $|r_2|^2$ from a 3D terminated end with circular gratings of different periods. Override mesh size is 10 nm.

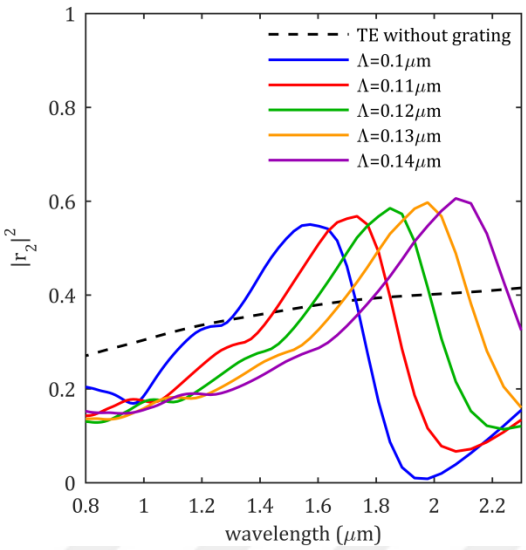

Figure 2.31 Comparision of the power reflection $|r_2|^2$ from a 3D terminated end with circular gratings of different periods. Override mesh size is 5 nm.

For almost the same grating parameters (except number of periods N), the r_2 spectrum for grating of period Λ=100 nm shown in Figure 2.30 and Figure 2.31 are not the same which is due to the coarse mesh size of 10 nm used in the initial test simulation.

So far, we have used duty cycle of dc=50%, therefore, we tried to optimize the r_2 reflection from the terminated end by sweeping over the duty cycle dc. For this end, we swept over the parameters W_s and W_g both in the range 40-80nm with steps of 10 nm and we evaluated the r_2 reflection for each (W_s, W_g) pair at wavelength 1550 nm. The resulting contour plot (shown in Figure 2.32) reveals the hotspots for which the r_2 reflection coefficient can be as high as 0.5 at 1550 nm. Based on the knowledge we gained from this contour plot, we selected a grating with silica trenches of width W_s=60nm and gold blades of width W_g=50 nm and thus duty cycle of $dc=W_s/\Lambda=W_s/W_s+W_g$=55% which results in r_2 spectrum with a peak at 1550 nm. The other parameters of the grating were: d_0=30 nm, θ=70°, N=6. In Figure 2.33 we compare the amplitude and phase of r_2 coefficient for the terminated end with and without selected grating and as is seen there is some improvement in the r_2 coefficient.

We added the selected grating of optimized parameters to the stub ends of the DS resonator and we ran a full 3D FDTD simulation to obtain the transmission of the double-

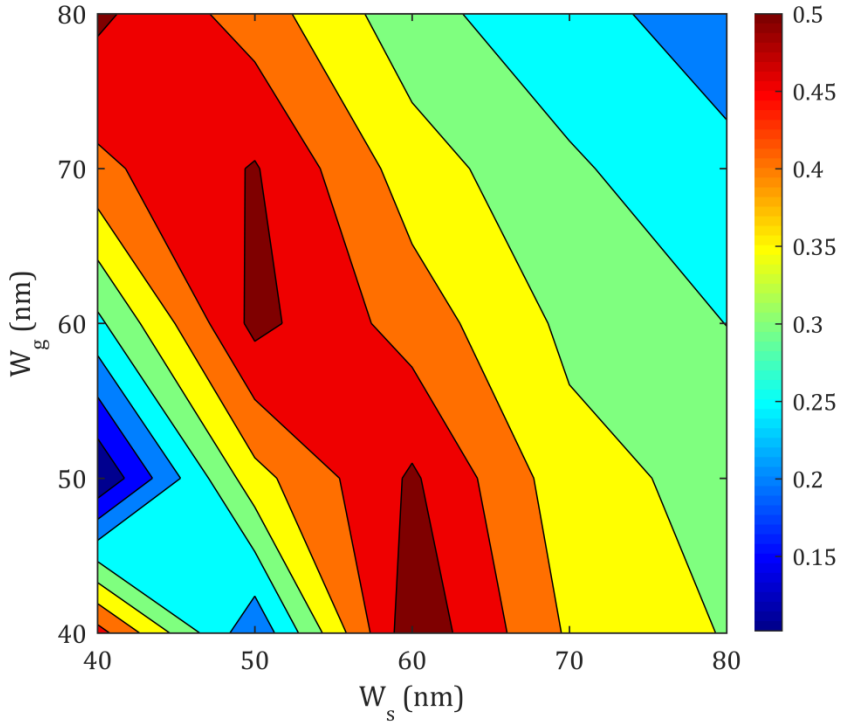

Figure 2.32 Contour map showing the relationship between the widths of silica trenches, gold blades, and power reflection $|r_2|^2$ at 1550 nm.

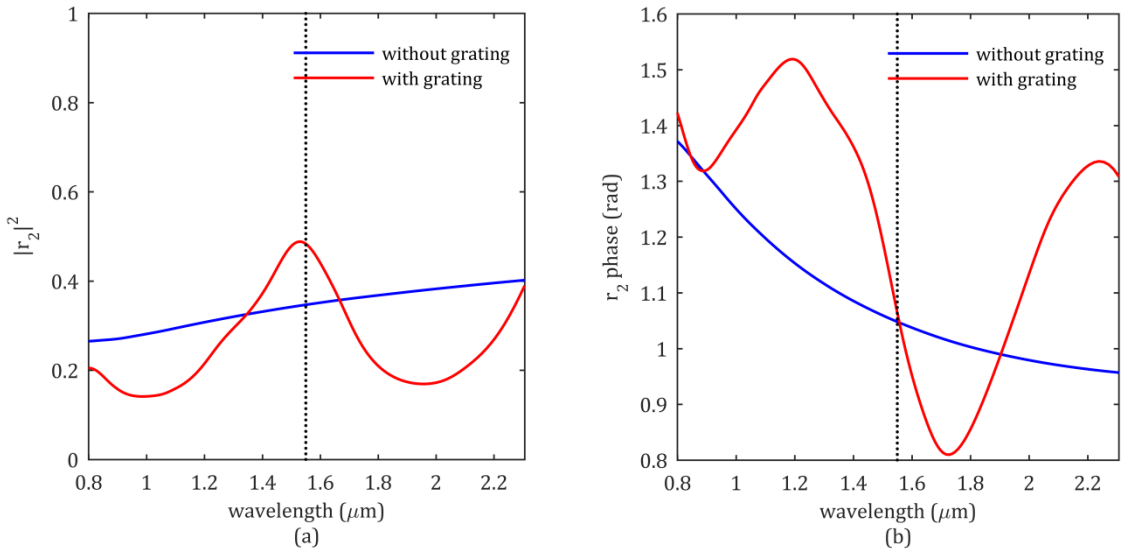

Figure 2.33 (a) Comparision of the power reflections $|r_2|^2$ from a 3D TE with and without optimized grating. (b) Comparision of the phases of reflection coefficient r_2 from a 3D TE with and without optimized grating. The parameters of the optimized grating are: W_s=60 nm, W_g=50 nm, dc= 55% d_0=30 nm, θ=70°, N=6. Black dotted line shows the location of the operating wavelength 1550 nm.

stub resonator. It should be noted that according to the TDS formula given by Eq. (2.3), any change in r_2 reflection coefficient should change the transmission map of the modified double-stub resonator such that the new resonant length pairs will be different than those corresponding to a DS resonator without grating at its terminated ends. However, surprisingly, the addition of the gratings and the change of r_2 reflection coefficient did not change the resonant length pairs of the modified DS resonator. This is most probably due to the fact that according to Figure 2.33(b) the phase of the r_2 reflection coefficient after addition of the grating remains almost equal to the phase of the r_2 reflection coefficient of 3D TE without grating at 1550nm. Therefore we set the stub lengths of the DS resonator with gratings to L_1=L_2=0.91 μm and compared its spectrum with the DS resonator (without gratings) with stub lengths set to L_1=L_2=0.91 μm. As shown in Figure 2.34, the addition of gratings results in 10% increase in the transmission power of the double-stub resonator. However, since the addition of a grating increases the device footprint which is a detriment in plasmonic field we decided to try another method for boosting the r_2 reflection. In this method, we modified the terminated end based on the knowledge we gained from the analysis the DS resonator itself which is described in the next section.

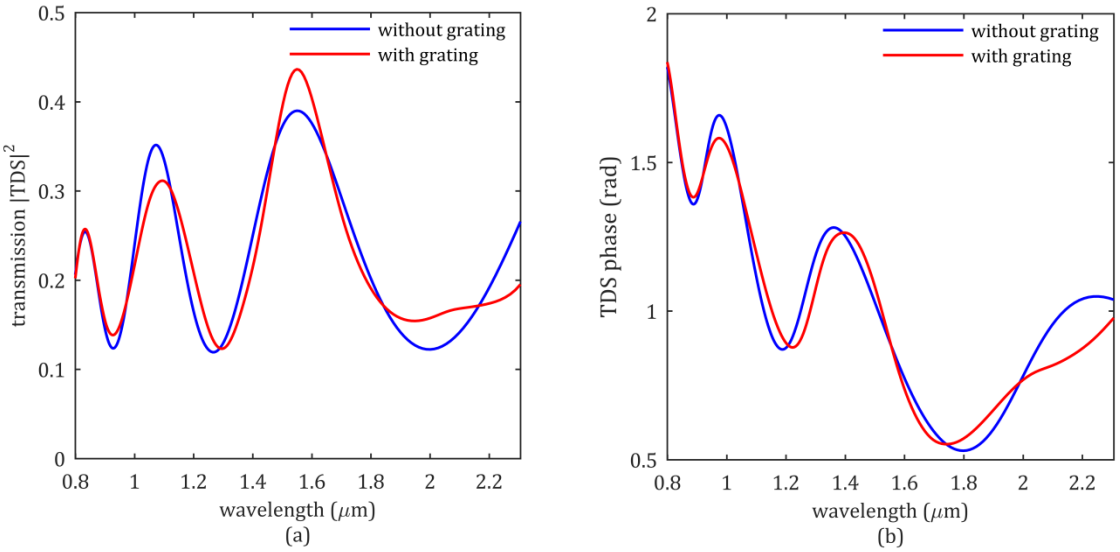

Figure 2.34 (a) Comparision of the power transmissions $|TDS|^2$ of 3D DS resonators with and without optimized gratings at the ends of their stubs. (b) Comparision of the phases of the transmission coefficients *TDS* of 3D DS resonators with and without optimized gratings at the ends of their stubs. The parameters of the optimized grating are: W_g=60 nm, W_s=50 nm, *dc*= 55% d_0=30 nm, θ=70°, N=6.

2.4.3.2 DS-terminated stubs

Another method that we tried for boosting the r_2 reflection coefficient was to add a double-stub resonator to the 3D terminated-end as shown in Figure 2.35(a). According to the transmission map of the 3D DS resonator [Figure 2.23(b)] the length pairs that result in a dip in the transmission of the DS resonator, result in a peak in the reflection spectrum. Hence, by adding a double-stub resonator with a dip in its transmission and thus a peak in its reflection to the terminated end we can expect an increase in the r_2 reflection coefficient.

In Figure 2.37(a) we compare the r_2 reflection coefficient evaluated for the 2D and 3D terminated-ends as well as the r_2 reflection coefficient for a terminated-end with a double-stub resonator with stub lengths corresponding to the second order dip D(2,2) in Figure 2.23(b). As is seen, the r_2 reflection coefficient for the 2D terminated-end is a lot higher than the 3D terminated-end and the 2D terminated-end acts almost like a perfect mirror. Further, it is evident that adding a DS resonator to the 3D terminated-end increases the r_2 reflection coefficient. We also tried the double-stub resonator corresponding to the first order dip D(1,1) in Figure 2.23(b), however, the improvement in r_2 reflection coefficient was not large enough so we selected the double-stub resonator corresponding to the second order dip in the transmission.

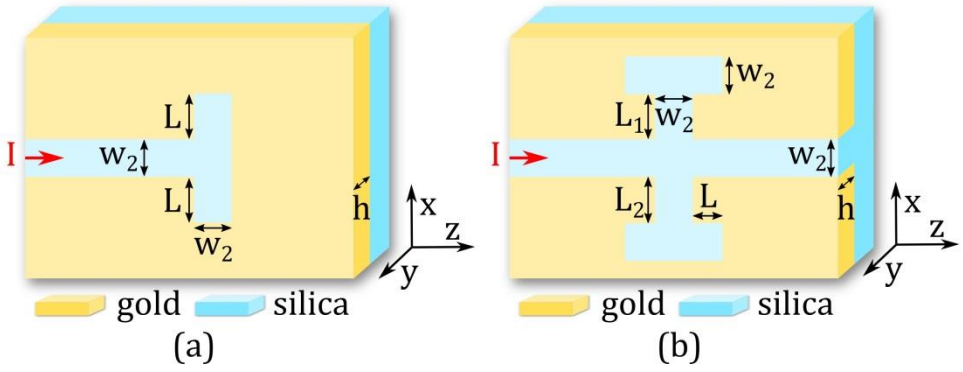

Figure 2.35 (a) Terminated-end with a DS resonator (b) double-stub resonator with DS resonator at the end of its stubs.

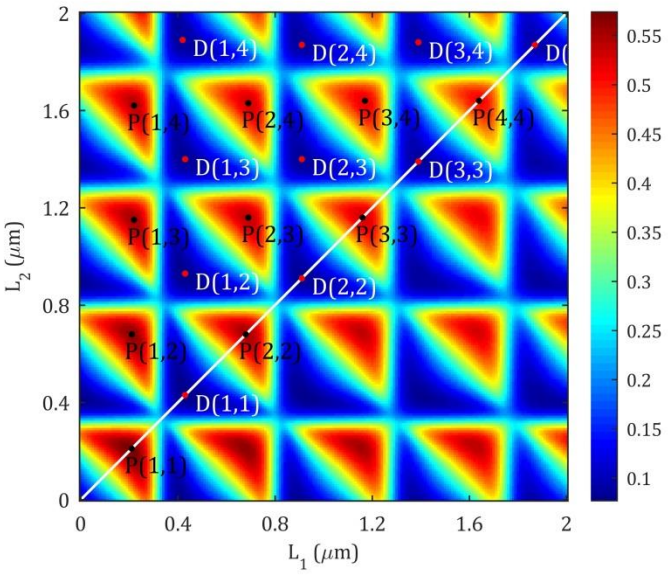

Figure 2.36 Power transmission coefficient $|TDS|^2$ versus L_1 and L_2 at 1550 nm for the 3D DS resonator with DS-terminated stubs.

$L_1=L_2=L_{dip}$ (nm)	FWHM (nm)	Q-factor
430	694	2.22
910	380	4.08
1390	260	5.96
1870	199	7.78
$L_1=L_2=L_{peak}$ (nm)	FWHM (nm)	Q-factor
210	1057	1.50
680	420	3.69
1160	269	5.76
1640	201	7.72

Table 2.5 Spectrum specifications of first four resonant orders resulting in a dip or a peak in power transmission of the 3D double-stub resonator with a DS termination.

Schematic of a double-stub resonator with a double-stub at the end of its stubs are shown in Figure 2.35(b). Any change in the r_2 reflection coefficient affects the transmission map of the double-stub resonator such that the locations of the resonant length pairs that correspond to dips or peaks change. By reevaluating the transmission map for a double-stub resonator (with double-stub at the end of its stubs) we selected the length pair L_1=L_2=680 nm corresponding to the second-order peak P(2,2) in its transmission power map (shown in Figure 2.36) to be able to compare its power transmission with the power transmission of a double-stub resonator (without double-stub at the end of its stubs) with stub lengths L_1=L_2=910 nm corresponding to the second-order peak in its power transmission map. The comparison result [Figure 2.37(b)] reveals that the addition of DS resonator to the stub ends improves the contrast and amplitude of the transmission spectrum.

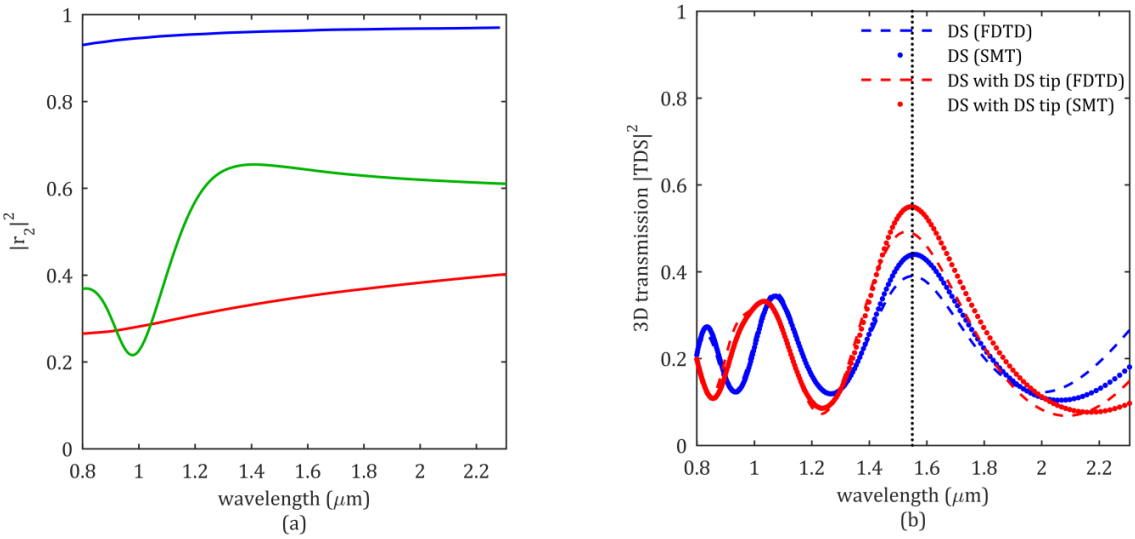

Figure 2.37 (a) Comparison of the reflection coefficients of the terminated ends (TE). Blue line: 2D TE, red line: 3D TE, green line: 3D TE with DS at its end, (b) comparison of the |TDS|2 results. Blue curve: P(2,2) resonator as in Figure 2.23(b), red curve: P(2,2) resonator as in Figure 2.36 with DS terminated stubs. Solid lines are scattering matrix results and dashed lines are calculated numerically with 3D FDTD simulations.

Chapter 3
FABRICATION

3.1 EBL Mask

Prior to fabrication we designed our mask with LayoutEditor, which is a software for designing the pattern of MEMs and ICs to be fabricated with nano-lithography instruments.

In the fabrication phase, for experimental purposes we designed bend waveguides instead of straight waveguides to increase the signal to noise ratio (see chapter 4 for more details). Additionally, in practice there is an impedance mismatch between the free-space wave and the slot-waveguide that is not addressed in the simulations. To overcome this mismatch, we added the nanoscale counterpart of the Uagi-Uda style dipole antenna to the input and output ends of the bend waveguides to facilitate and increase the efficiency of coupling free-space input laser beam to the subwavelength gaps of slot waveguides as well as efficient decoupling of SPP waves into free-space for measuring purposes. We adapted the same dimensions as [55] for our antennas which are designed for operating wavelength of 1550 nm (Figure 3.1). This antenna has been proven to be an efficient coupler for exciting subwavelength SPP waves [55,56,57,58].

Symmetric slot waveguides do not suffer from lower or upper modal cutoff when their

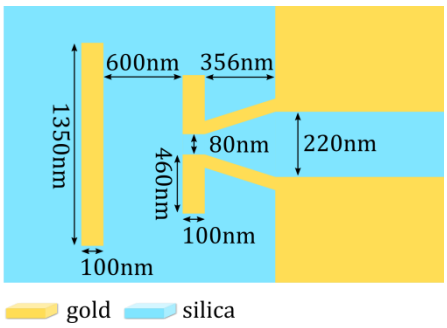

Figure 3.1 Dimensions of dipole antenna along with its non-resonant reflector element and taper.

dimensions are reduced or increased [27]. This enables us to use a taper to connect the dipole antenna to the waveguide entrance to reduce back reflections due to impedance mismatch between antennas and waveguide. Due to the symmetry the dipole antenna radiates in both directions therefore a non-resonant reflector element is used to reflect back the backward propagating radiation toward slot-waveguide to further increase the coupling efficiency.

According to our simulations the spectral response of single-stub resonators has very low contrast such that any non-ideality in their fabrication will cause the resonance to be embedded in noise. However, double-stub resonators provides better contrast and sharper peaks therefore we focused on their fabrication and characterization.

For each waveguide with double-stub resonator we also designed a corresponding bend slot-waveguide without any resonator for normalization purpose in order to compensate propagation and radiation losses and to obtain the pure response of the resonator (Figure 3.2).

One of the most interesting aspects of 3D plasmonic waveguides is that they enable light to be routed around a sharp 90° bends, a feature not available in either conventional dielectric waveguides or photonic crystal devices [13,34]. In 2D plasmonic waveguides

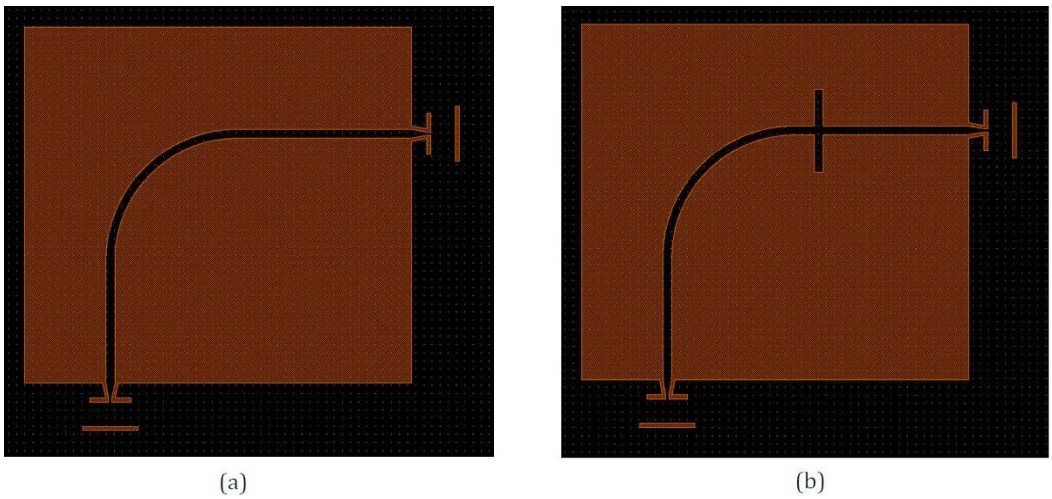

Figure 3.2 Designed mask: (a) bend slot-waveguide with input and output antennas, (b) bend slot-waveguide with double-stub resonator of equal stub lengths added.

the radiation loss through right-angle bends is small and can be made almost zero by introducing a curved bend instead of a right-angle bend [13].

However, in 3D slot waveguides unlike 2D MDM waveguides, due to their open nature radiation losses through right-angled corners is high [34]. Therefore a round curve is preferred to the sharp corners to reduce the radiation losses. Optimized radius of curvature recommended in the literature for reducing the radiation loss in SWG bends is between 3-4 μm [55].

We designed two sets of slot-waveguides either with radius R=3 μm or R=4 μm. Due to rather low power propagation lengths of 3D slot-waveguide evaluated as ~9 μm at 1550 nm we also designed samples with three sets of lengths: 8 μm, 10 μm, 12 μm. We patterned samples in a dose array of 3×3 with dose ranging between 600-1000 μC/cm^2 with step of 50 μC/cm^2.

3.2 Fabrication Procedure

In this section we briefly overview the fabrication steps for plasmonic 3D slot waveguide on a single crystal quartz (SiO_2) substrate. The fabrication steps for fabrication of 3D slot-waveguide are schematically illustrated in Figure 3.3.

The same procedure holds in the fabrication of other structures. The details of fabrication recipe are described in section 3.3.

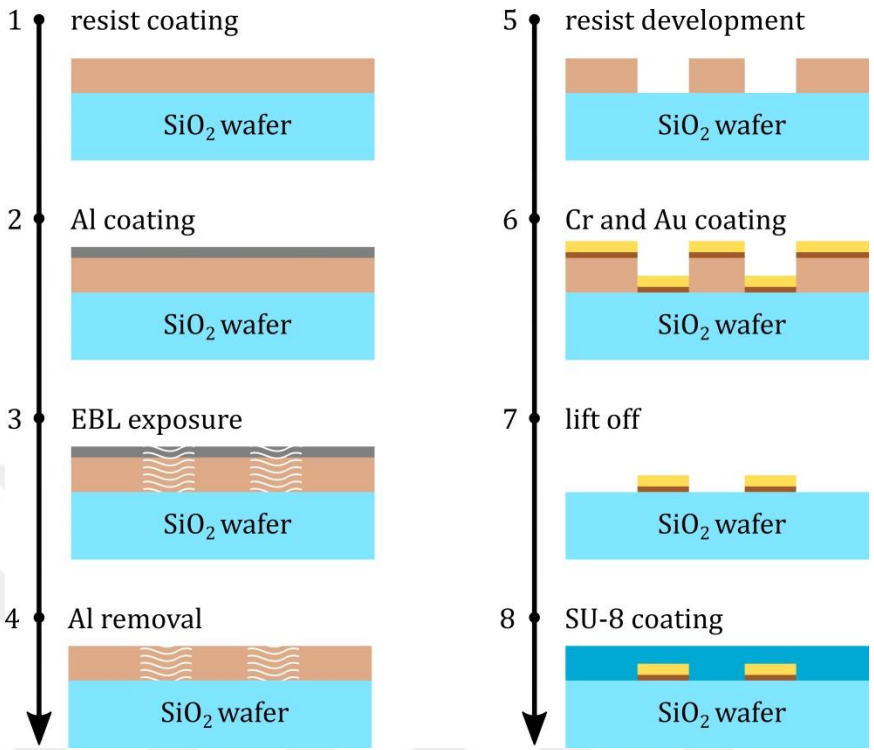

Figure 3.3 Schematic of fabrication steps for fabrication of 3D symmetric slot-waveguide (silica/gold/SU-8).

The fabrication steps for fabrication of plasmonic 3D slot-waveguide are as follows:

1. Standard wafer cleaning procedure, so-called Piranha cleaning, is performed on the wafer prior to dicing.
2. Cleaned wafer is diced into pieces.
3. Standard cleaning of diced substrates is performed.
4. Sample is coated with resist.
5. The resist-coated sample is coated with aluminum to avoid charging effects during the EBL exposure.
6. The Al-coated sample is exposed with EBPG.
7. Al layer is removed after exposure.
8. Exposed sample is developed to carve the pattern on the resist.
9. For better adhesion and high quality gold layers, the developed sample is first coated with Titanium (Ti) prior to gold coating.

10. Titanium-coated sample is then coated with gold.
11. The standard liftoff procedure is applied to remove the residue resist.
12. The resultant sample is then coated with SU-8 to make the fabricated waveguide symmetric.

3.3 Fabrication Recipe

The detailed steps of fabrication are as follows:

1. *Sample Cleaning (Koç Clean Room)*

- Mix 95% H_2SO_4 (50 mL) with 35% H_2O_2 (20 mL) to make the so-called piranha mixture.
- Wait for 2 minutes to let the mixture to cool down
- Keep quartz samples in piranha mixture for 5 mins
- Wash samples with DI Water 1 for 30 seconds
- Wash samples with DI Water 2 for 30 seconds
- Wash samples with DI Water 3 for 30 seconds
- Dry samples with N2 gas gun

2. *Resist Coating (SUNUM)*

    - 5000 rpm 495K A4 + 950K A2 Microchem coating, bilayer resist, total thickness ~250-300 nm (http://microchem.com/pdf/PMMA_Data_Sheet.pdf)
    - 170C bake for 5 mins

3. *Al Metallization (SUNUM)*

    - 15 nm Al coated at ~1E-6 torr

4. *Al Removal (SUNUM)*

- 1 min in AZ 726 developer (TMAH based)
- Distilled water clean
- Dry

5. *PMMA Development (SUNUM)*

- 1:3 (MIBK:IPA) 1min
- 1:1 (MIBK:IPA) 5 sec to remove residual PMMA (can replace with O_2 etch at KUYTAM)
- IPA 30 sec
- Dry with N_2 gun
- Microscope inspection

6. *Titanium+Gold Coating (KUYTAM)*

- Nanovak nvts 400 machine
- Loaded 1.6 gr Au %99.99
- Loaded 2 of the 4 EBL written samples (C_1, C_2)
- Loaded extra 2 empty samples (M_1, M_2) to measure Au permittivity
- 2E-6 torr base pressure
- Ti 57.1 Amp, 2.6 V, 0.2 angstrom/sec, total 4 nm
- Au 91 Amp, 0.9 V, ~0.5 angstrom/sec, total 115 nm

7. *Lift-off (Koç Clean Room)*

- 15 mins in hot acetone (50 °C)
- 3 min flush with acetone
- 10 mins in acetone with ultrasonic cleaner
- 10 mins in IPA with ultrasonic cleaner
- Dry with N_2 gun
- Microscope inspection

8. *SU8 Coating*

- Use SU8 2000 thinner to reduce SU8 2010 (58%) to SU8 2000.5 (14.3%) level
- 3000 rpm coating should give 450-500 nm of resist

- Exposure & hard bake might be necessary
- 500 rpm 5 sec 300 rpm/sec acceleration
- 3000 rpm 30 sec 300 rpm/sec acceleration
- 95 °C softbake (1 min)
- Microscope inspection

3.4 Fabrication Results

The Field Emission Scanning Electron Microscope (FESEM) images of the fabricated slot-waveguide and slot-waveguide with a double-stub resonator of equal stub lengths are shown in Figure 3.4. The images belong to the sample without SU-8 coating. The SU-8 coated sample due to being an insulator causes charging effects under FESEM which prevented us from having high resolution images especially at higher magnifications.

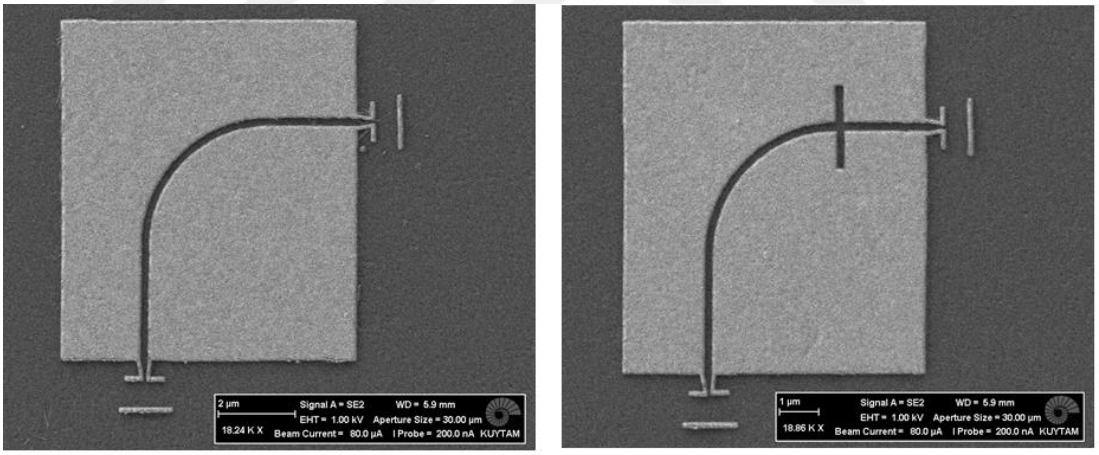

(a) (b)

Figure 3.4 FESEM images of uncoated (a) 3D slot-waveguide with input and output dipole antennas, (b) 3D slot-waveguide with input and output antennas and a double-stub resonator of equal stub lengths. The total length of the designed bend waveguides is 10 µm and the radius of curvature is 3µm in both images. The designed stub lengths are 910 nm. Both images belong to dose 850 µC/cm^2.

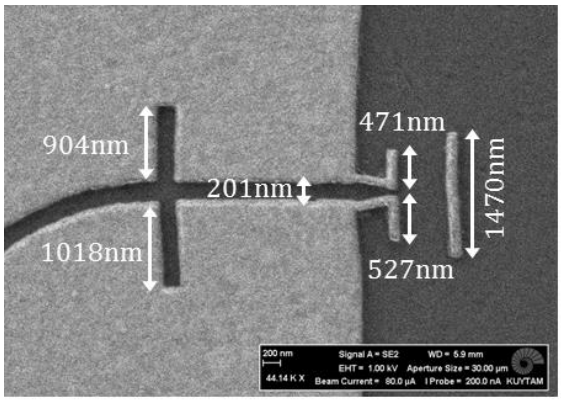

(a)

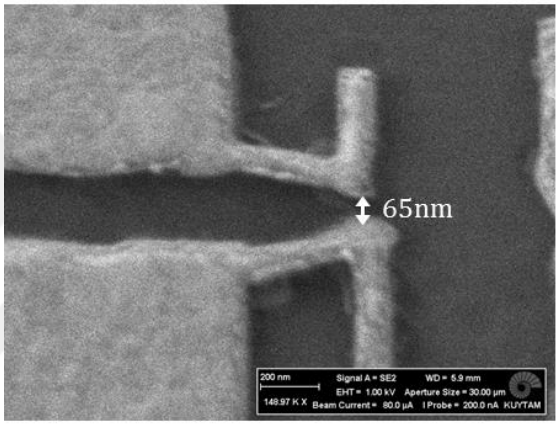

(b)

Figure 3.5 Magnified images of Figure 3.4: (a) critical dimensions of the double-stub resonator and dipole antenna after fabrication, (b) width of antenna gap after fabrication. Both images belong to uncoated sample at dose 850 μC/cm^2.

Therefore, to have better understanding of the dimensions of the fabricated structures we took FESEM images of the uncoated sample. The SEM images of the SU-8 coated sample are shown in Figure 3.6 for comparison.

The dimensions of the fabricated antennas are specified in Figure 3.5(a,b). There are always deviations between the dimensions of the designed and fabricated structures as can be seen by comparing designed dimensions shown in Figure 3.1 and fabricated ones shown in Figure 3.5(a,b). It should be noted that, the inequality in the lengths of upper and lower stubs as well as upper and lower sections of the dipole antenna is again due to the charging effects.

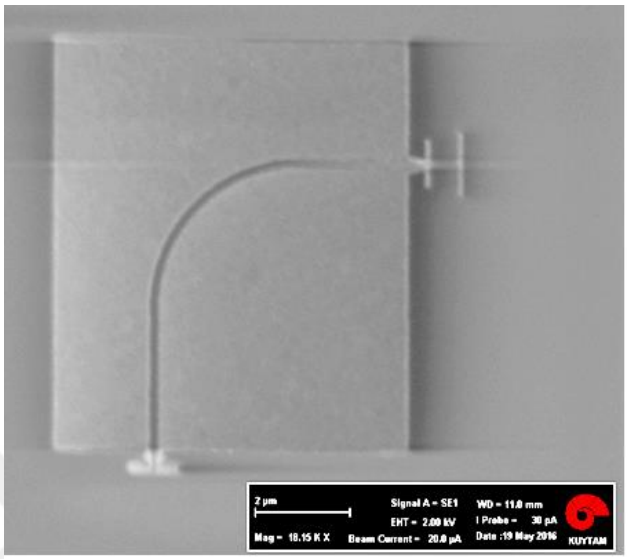

(a)

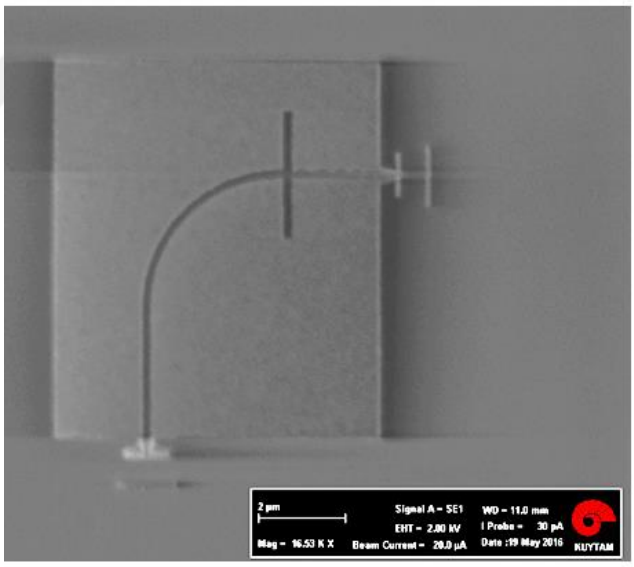

(b)

Figure 3.6 SEM images of SU-8 coated (a) 3D slot-waveguide, (b) 3D slot-waveguide with a double-stub resonator of equal stub lengths. The total length of designed bend waveguides is 12 µm and the radius of curvature is 3 µm in both images. The designed stub lengths are 1080 nm. Both images belong to dose 850 $\mu C/cm^2$.

Chapter 4
MEASUREMENT

4.1 Experimental Setup

We characterized our samples with a home-built optical far-field reflection microscopy setup. The schematic of this setup is shown in Figure 4.1. We adapted the so-called cross-polarization method in which two linear polarizers oriented perpendicular to each other (labeled as LP_1 and LP_2 in Figure 4.1) are employed to measure the output signal radiated from the output dipole antenna while suppressing the input signal and thus to increase the signal-to-noise ratio (SNR) [55,56,57]. In this method, bend waveguides are used instead of straight waveguides to rotate the polarization of the output signal 90 degrees with respect to the input signal. To efficiently excite the input dipole antenna the polarization of the input beam should be parallel to the dipole axis of the input antenna thus the polarization axis of LP_1 (650-2000 nm) is aligned parallel to the dipole axis of the input antenna. Accordingly, to efficiently collect the radiated signal from the output antenna the polarization of LP_2 (650-2000 nm) is aligned parallel to the dipole axis of the output antenna. The polarization of the output signal after turning the bend waveguide rotates 90 degrees with respect to the input signal and thus only output signal will pass through LP_2 polarizer and the input signal due to having perpendicular polarization will be suppressed.

If instead of bend waveguides, straight waveguides had to be used then the input and output signals both had the same polarization states and the weak output signal in the order of nW would have been buried in high intensity input signal of order mW and it was impossible to detect it.

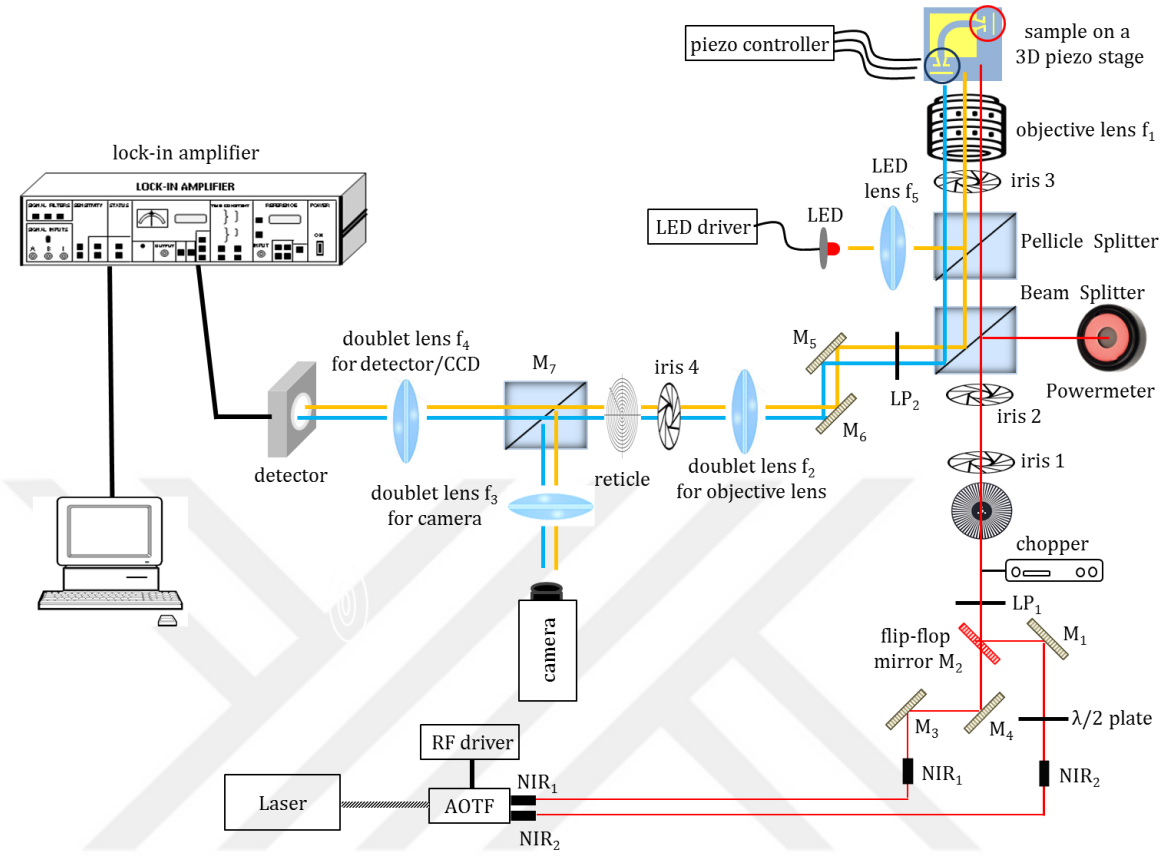

Figure 4.1 Far-field cross-polarization reflection microscope setup.

However, due to the near-field effects at the focus of a high NA objective lens [10,59] a linearly polarized input beam does not remain linearly polarized after being focused by a high NA objective lens but it gains other polarization states. Due to this phenomenon, as shown in Figure 4.2 the input signal is not fully eliminated by the second linear polarizer (LP_2) such that at the cross-polarization configuration not only the round output signal is imaged but the residual spatial intensity pattern of input beam with a four-lobe shape is also imaged at the location of the input beam [55,56,57]. This is the residue of the linearly-polarized input laser beam that acts as a noise. As will be explained in below we will use an iris to cover up this noise beam.

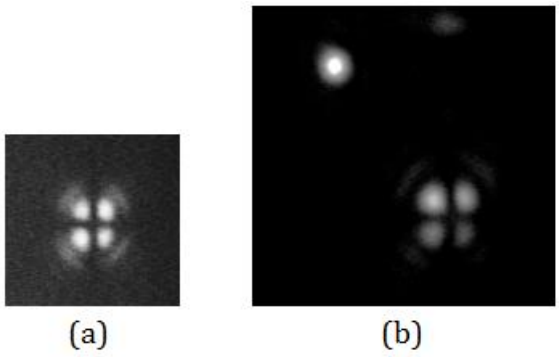

Figure 4.2 (a) The four-lobe residue input beam reflected off of quartz-air surface of uncoated sample at 1550 nm in cross-polarization configuration, (b) output signal radiated from output dipole antenna in a bend waveguide of 12 um long and input signal reflected off of SU-8 coated sample at the location of input dipole antenna when iris4 is not closed. Two AOTF channels of 1475 nm and 1550 nm are on for better visualization of weak output signal. Images are taken with infrared camera and in both images chopper, reticle, and LED light are removed for having better images of input and output signals.

We used a red LED (Edison, 2ES103RX000001) of maximum power 3 W radiating at 620-630 nm to illuminate our sample. Since we characterize the performance of our double-stub resonators in near infrared (1200-1700 nm) and they are specifically designed for operating wavelength of 1550 nm, it would be good if we illuminated the sample with LED radiating around 1550 nm to be able to focus on both input beam and sample image simultaneously. However, due to the lack of high power LEDs at 1550 nm they turned out inefficient in illumination of sample such that the image resolution decreased and dipole antennas were not visible. Consequently, due to the mismatch between the illumination wavelength and input/output wavelengths the sample image shifts with respect to input/output signals.

We used a super continuum pulsed fiber laser (Fianium, Model: SC450), with pulse repetition rate of 40 MHz and maximum free-space output power of 4 W for excitation of our samples. The laser has a broad operational wavelength range as 450-1700 nm.

A dual acousto-Optic tunable filter AOTF unit (Fianium) is used to select one (or more) wavelength at a time from supercontinuum laser and tune the input beam. This unit has two AOTF crystals with two free-space/fiber-coupled outputs: NIR_1 (650-1100 nm), NIR_2 (1100-2200nm). We work with NIR_2 output fiber and a longpass filter is used in front of this output to filter out the wavelengths below 1000 nm. The power delivered to NIR_2 output fiber at 1550 nm is around 1.5 mW.

A half-wave plate is placed in the beam path for maximizing the intensity of the input beam after LP_1 which is always set parallel to the dipole axis of input antenna. The two broadband dielectric mirrors M_1 and M_2 designed for wavelength range 1200-1600 nm are used for setting the optical path between iris1 and iris2. Iris3 is used to ensure that the input beam goes through the objective lens after placing the beam splitter in the path.

The experimental setup has three different arms. The first arm is the input arm extending from NIR_2 output fiber to the objective lens which is used for directing the laser beam to the sample and its excitation. The second arm is the imaging arm extending from objective lens to the infrared camera (0.4-1.9 um) which is used to image the sample. And the third arm is the measuring arm that extends from objective lens to the detector (800-1800 nm) and is used for measuring the output signal from output dipole antenna. To switch between second and third arms we used a removable diagonal silver mirror labeled as M_7 in Figure 4.1.

Sample is placed on a pitch and roll tilt platform (Thorlabs, APR001/M) for adjusting its tilt and ensuring that the reflected light off of the sample surface is passing through iris4. For this purpose, prior to mounting the real sample on the tilt platform a gold-coated sample which acts as a mirror is first installed on it to adjust the tilt of the sample.

The tilt platform is then mounted on an automatized piezoelectric *xyz*-translation stage (Thorlabs, NanoMax-TS) with resolution (minimum displacement) of 20 nm for fine adjustments of focus or small displacements on sample surface. Piezo stage is further mounted on a manual *xyz*-translation stage for coarse alignment and large movements or sample surface.

The 3D piezo stage is used for three different purposes: 1) to place the sample at the focus of the objective lens and adjust the focus, 2) to move around on the sample surface and locate the desired structure that we would like to characterize, 3) to fine align the location of the input antenna with respect to the input beam, which is kept fixed after setting the optical path of the first arm, to increase the antenna efficiency. The piezo stage is drived with a piezo controller and is remotely controlled by computer.

A Pellicle (1-2 μm) directs the LED light to sample surface and transmits the sample

image signal toward the third arm into the infrared camera (when diagonal mirror M_7 is in its place).

Similarly, a beam splitter (1.1-1.6 μm) transmits the input beam to sample and directs the output signal and the residue of input signal reflected off of the sample surface to either infrared camera or detector.

The optical axis of the first arm of the setup is aligned by input laser beam, however the optical axis of the third arm (measuring arm) is aligned using the input beam, tilt platform, reticle (Thorlabs, R1DS2P) and a CDD camera(400-1000 nm). Note that when aligning the measuring arm detector is removed and a CCD camera is installed at the location of the detector for aligning purposes. By ensuring that image signal is centered in CCD camera we make sure that it is also centered on the detector with limited circular active area of 2 mm diameter. In alignment phase we work in parallel-polarization configuration such that LP_2 is parallel to LP_1 for having intense input power and facile the alignment procedure.

Reticle is a transparent optic with ten numbered concentric circles increasing in diameter by 1 mm, superimposed on a crosshair as shown in Figure 4.3 and serves three different

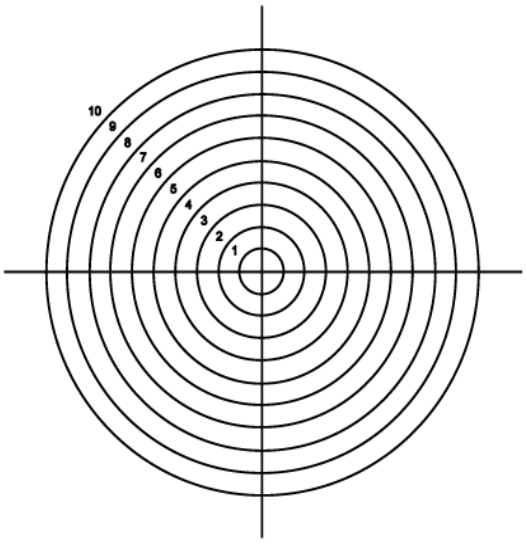

Figure 4.3 Positive concentric circle reticle (Ø1"), with transmission greater than 90% in the 200-1200 nm spectral range.

roles in our setup: 1) in alignment phase of second and third arms it is used for centering the sensors of infrared and CCD cameras with respect to the center of the reticle which coincides with the center of optical axis. This ensures that image signal hits the centers of the camera sensors. For instance, Figure 4.4 shows the cross-hair of reticle superimposed on the cross-hair of CCD camera, 2) it provides a reference location for the image formed by objective (f_1) and doublet (f_2) lenses, 3) it is used for evaluating the image magnification on detector and infrared camera. The detail on how reticle is used for the calculation of magnification is provided in section 4.3.

Accordingly, the third arm is aligned using reticle and screen image taken by infrared camera.

In the measuring arm, the input beam is only used for aligning purpose but for measuring purpose we just need the output signal to be centered to the optical axis of the measuring arm. Therefore, unlike the excitation arm that input beam has to propagate along the optical axes in the measuring arm it is the output signal that is required to propagate along the optical axes and the residue input signal reflected off of the sample surface at the location of the input antenna is an unwanted noise signal which should be made off axes. Since as shown in Figure 4.2 input and output signals are separated by the length of

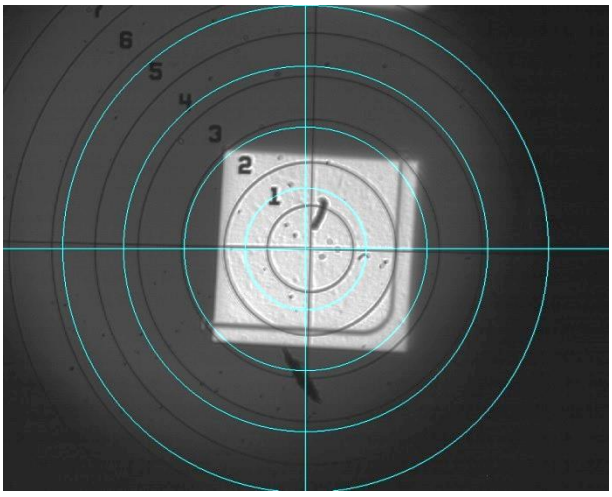

Figure 4.4 Aligning the center of the CCD camera and thus detector using reticle. Black circles belong to physical reticle and the green-circles are software-provided reticle belonging to the CCD camera.

bend waveguide, in longer waveguides centering the output signal becomes of particular importance because due to the limited size of the detector's active area the output signal might not hit the detector's sensor. To address this problem we have introduced two broadband metallic mirrors in the measuring arm labeled as M_5 and M_6 in Figure 4.1, in order to translate the output signal to the center of the detector. The output signal needs to be within the 2 mm diameter of the reticle that covers the active area of the detector's sensor to ensure that detector detects the output signal.

A distinguished feature of our setup we use lock-in amplifier for measuring the output signal. In all the already published papers that use cross-polarization method images captured by camera has been used for measuring the output signal [55,56,57].

4.2 Measuring Procedure

After aligning the setup and locating the structures on sample and imaging them with infrared camera we set the LP_1 parallel to input antenna and using half-wave plate we maximize the input beam through LP_1 for 1550 nm. We move the sample such that the input beam hits the quartz-air interface and we ensure that we set LP_2 parallel to the output antenna and by adjusting it in this cross polarization configuration we try to get the best image of the four-lobe pattern (on quartz-air interface) at 1550 nm such that the four lobes are as symmetric as possible and there are fringes around it as shown in Figure 4.2(a). This is to ensure that the alignment has been done correctly. We focus to this image to have the sharpest image possible and then during the measurement we do not touch the focus. However, the focus might be readjusted when we move from one structure to another due to the thickness non-uniformity of the sample surface which might originate from thickness non-uniformity of the substrate or SU-8 coating.

To start measurement we position the input antenna of the desired structure under the input beam and using piezo knobs we first manually adjust the location of antenna until we see the round output signal radiating from output antenna. The excitation of plasmonic gap modes is shown to depend on the polarization, position, and wavelength of the incident beam. Therefore, a computer code is developed for piezo stage to find the best location of the input antenna with respect to the input beam which gives the

maximum output signal. We collect the output signals from air.

Finally, using the M_5 and M_6 mirrors we translate the output signal to the center of the reticle, then we remove reticle and M_7 diagonal mirror and using a chopper we provide a reference signal to the lock-in which is connected to the detector and then we start the measuring. All our measuring procedure is automated by a MATLAB code. As shown in Figure 4.1, a germanium powermeter (700-1800 nm) has also been used to measure the input power for normalization purposes. Due to possible fluctuations in the Fianium power, we always need to measure the power from PM100 and use that as a normalization coefficient

4.3 Image Magnification

To excite the input antennas with input beam and to make sure that there is an output signal radiating out from output antenna we need to image the sample with high magnifications. A rather simplified schematic of our four-lens microscope setup is shown in Figure 4.5 to illustrate how imaging and measuring with desired magnifications is performed. The focal lengths of the lenses are given at the top right corner of the Figure 4.5.

Our infinity-corrected objective lens with focal length f_1=2 mm when combined with a doublet lens with focal length f_2=200 mm provides us with the magnification of 100×. This is the magnification of the first image which is formed by the objective lens f1 and the doublet lens f_2 at the location of the reticle which is positioned at the focus of the doublet lens f_2.

The first real image serves as a virtual image for infrared camera or detector and is imaged by the doublet lens f_3 on the infrared camera for imaging purposes and is imaged by the doublet lens f_4 on the detector for measuring purposes. Due to rather small size of the detector's sensor (∅=2 mm) the first magnification of 100× suffices for measuring arm therefore the real image and the detector are positioned at $2f_4$ on both sides of the doublet

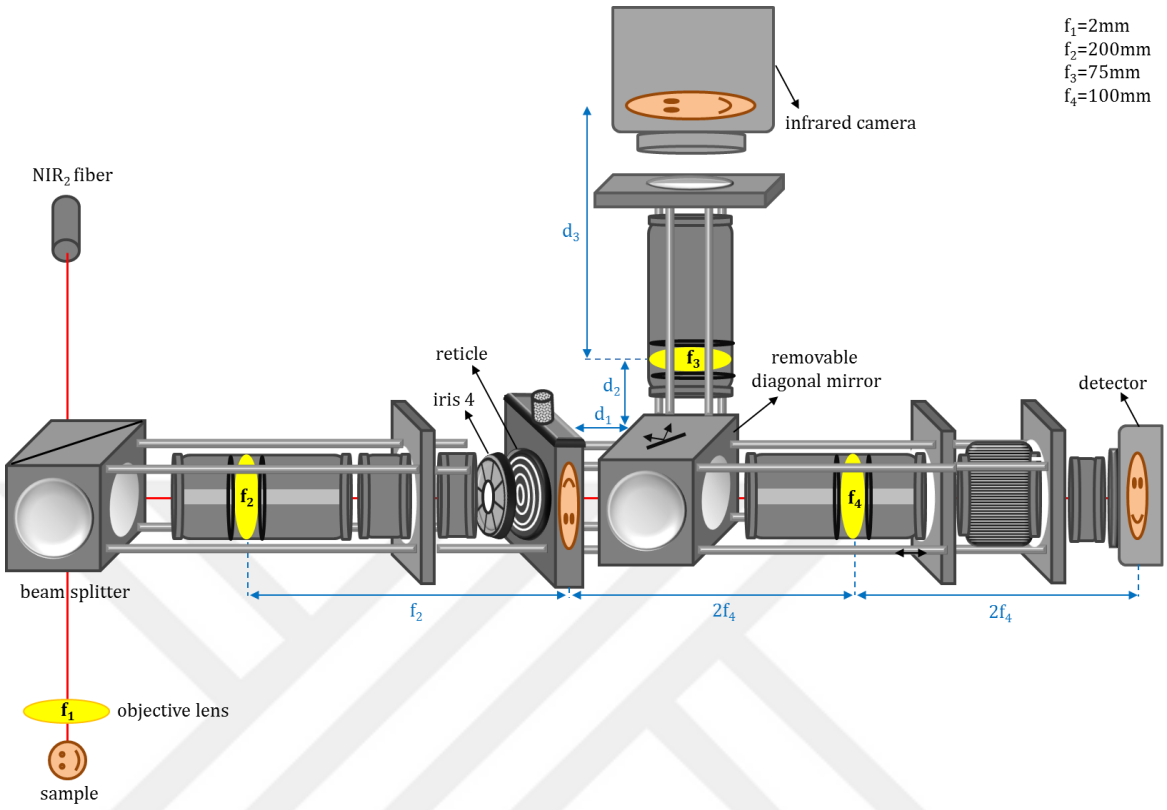

Figure 4.5 Simplified schematic of our four-lens microscope setup for illustration of image magnification.

lens f_4 which results in magnification of 1× to image the first real image on the detector with no further magnification. However, to locate input and output antennas in imaging arm we need magnifications in the range 150-200×. This is accomplished by adding the doublet lens f_3 that determines the ultimate magnification. From thin lens optics we know that to have a magnified image with magnifications greater that 1× the object needs to be within the range $f<d<2f$ from a thin lens which translates to $f_3<d_1+d_2<2f_3$ in our setup as shown in Figure 4.5. Therefore, the desired magnification is achieved by adjusting the distance d_1+d_2 which specifies the location of the object (real image) with respect to doublet lens f_3 and accordingly the distance d_3 which specifies the location of the image (infrared camera) with respect to the doublet lens f_3.

In our setup due to optomechanical connections d_1 is a fixed distance and thus we are just able to adjust the distance d_2.

By applying the Gaussian formula for the doublet lens f_3 given as

$$\frac{1}{p} + \frac{1}{q} = \frac{1}{f} \qquad (4.1)$$

where p is the object distance from lens, q is the image distance from lens, and f is the focal length of lens; we approximately calculated the d_1+d_2 and d_3 distance pairs and the corresponding magnifications as shown in Figure 4.6.

The distances are approximate due to the fact that the doublet lens is a thick lens and the Gaussian formula is valid only for thin lenses. However, the evaluated distances and magnifications matched in practice pretty well.

As is seen, to have magnifications between 150× and 200× which has turned to be sufficient for our imaging purpose, the doublet lens f_3 should be positioned within 11-12 cm away from reticle.

The image of the reticle and first image monitored by infrared camera are magnified with the same factor by doublet lens f_3, due to the fact that they are positioned at the same location in the microscope setup. Therefore, the magnification factor and the size of the

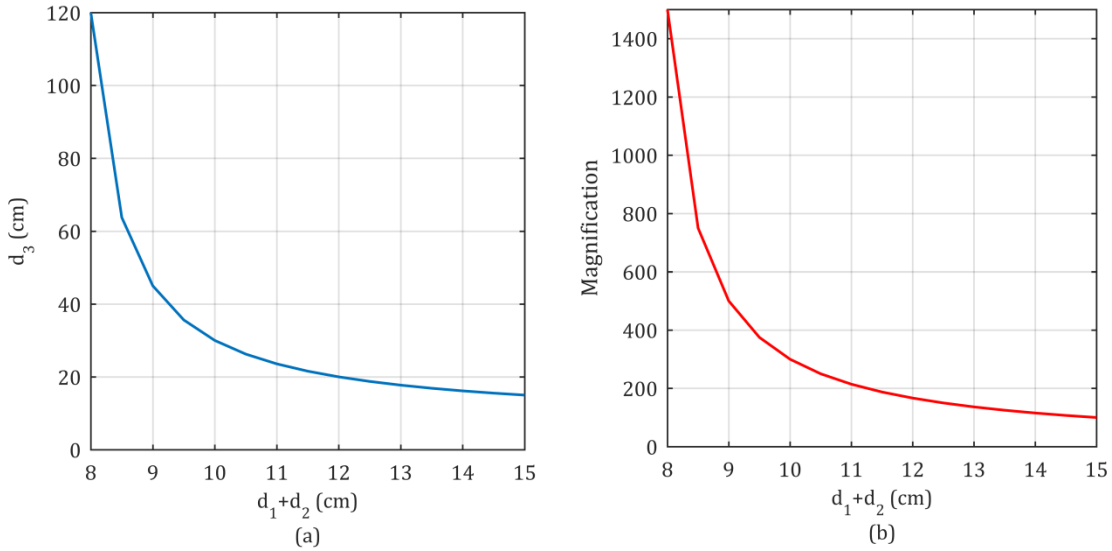

Figure 4.6 (a) Distance configurations of IR camera (d_3) and camera doublet-lens (d_1+d_2), (b) magnification corresponding to each distance configuration.

first image can be directly evaluated by comparing its size to the reticle rings. For instance, if a rectangle structure of length L=20 μm fits within the second ring of reticle amounting to 2 mm, then the total magnification at the location of reticle would be M_1=2 mm/0.02 mm=100.

However, the ultimate magnification factor on the sensor of the infrared camera is evaluated by comparing either vertical or horizontal lengths of the infrared camera sensor with sensor size of $V \times H$=9.5×12.7 mm^2 against the reticle rings. For instance if the fifth ring of the reticle fits to the camera sensor vertically then the magnification factor of doublet lens f_3 would be: M_2=9.5/5~1.9 which results in total magnification of $M=M_1 \times M_2$=190×.

4.4 Experimental Results

In this section we give the experimentally measured power transmission spectrum of two sets of double-stub resonators with equal stub lengths $L_1=L_2$=0.91 μm and $L_1=L_2$=1.39 μm. We expect to have some discrepancies between the measured and simulated results due to the following reasons: 1) as shown in Figure 3.5 fabricated dimensions are always expected to slightly deviate from the designed ones, 2) the vertical walls of the fabricated waveguides might be slightly angled, 3) unlike simulation, the spectrum of the input beam as shown in Figure 4.7 is not uniform for all wavelengths, 4) there are always impurities and unwanted residue of materials during different fabrication steps that act as loss and scattering centers which degrade the fabricated device performance compared to the simulated results, 5) dielectric functions of silica and gold are dependent on the fabrication conditions and might be different from those used in simulations.

Only half of the input power is directed into the sample by the beam splitter (50:50) and the other half is dumped. Therefore, by positioning the powermeter at the location showed in Figure 4.1 we can measure the input power which its spectrum is shown in Figure 4.7.

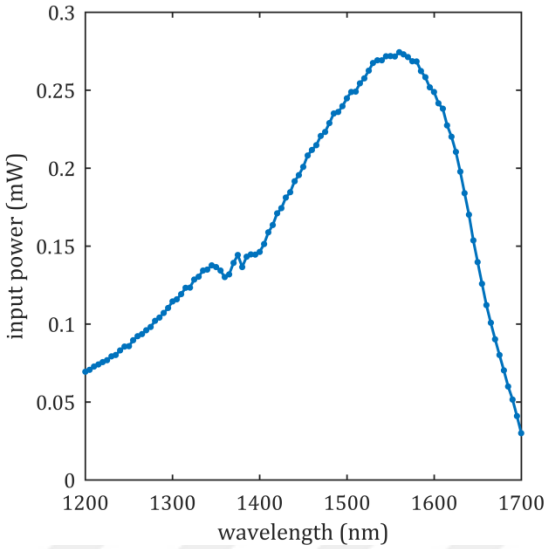

Figure 4.7 Power spectrum of incident beam measured by powermeter positioned at the location shown in Figure 4.1

This power is obviously lower than the input power at the tip of the NIR_2 fiber. Due to possible power fluctuations of Fianium laser from one measurement to another we normalize each measured data by the lock-in amplifier with the input power. However, it should be noted that not all of the input power is coupled to the waveguide mode. Some of the input power is reflected off of the SU-8/air interface and some is converted to loss in the input antenna.

The non-uniformity of the input beam spectrum influences the response of the bend waveguide as well as the dipole antenna compared to the simulation results. Moreover, the spectral response of the double-stub resonator would also be embedded in the spectral responses of input and output antennas and bend waveguides. The total transmission of a bend waveguide without resonator is given by

$$\begin{aligned} T_{tot}(\lambda) &= T_{ant_{in}}(\lambda)\, T_{swg}(\lambda)\, T_{ant_{out}}(\lambda) \\ &= T_{ant_{in}}(\lambda)^2\, T_{swg}(\lambda) \end{aligned} \qquad (4.2)$$

where, $T_{ant_{in}}(\lambda)$ and $T_{ant_{out}}(\lambda)$ are the spectral responses of input and output antennas that are assumed to be identical and $T_{swg}(\lambda)$ is the transmission of the slot waveguide.

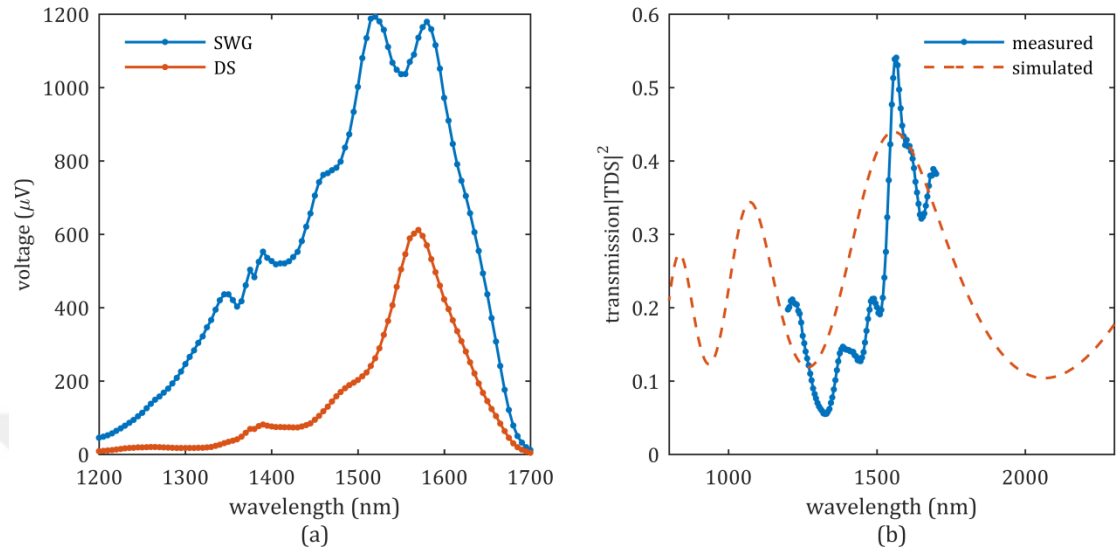

Figure 4.8 (a) Spectral response of slot-waveguide (8 μm long with radius of curvature 3 μm) and corresponding double-stub resonator (with stub-lengths L_1=L_2=0.91μm) measured with lock-in, (b) normalized spectrum of the same double-stub resonator and simulated spectrum. Both graphs belong to SU-8 coated sample with dose 900 μC/cm^2.

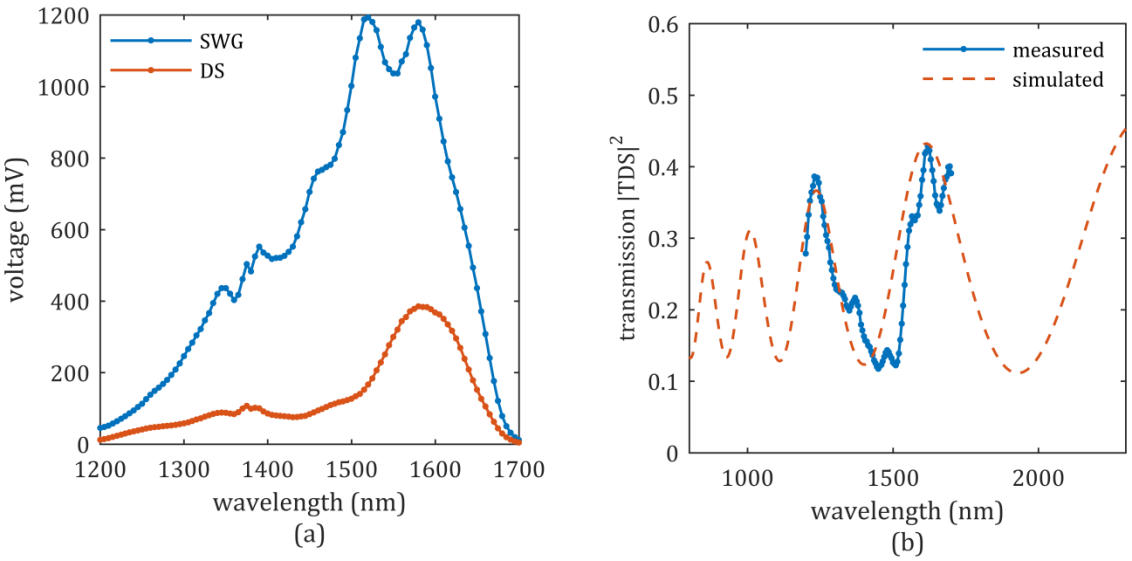

Figure 4.9 (a) Spectral response of slot-waveguide (8μm long with radius of curvature 3 μm) and corresponding double-stub resonator (with designed stub lengths L_1=L_2=1.39 μm) measured with lock-in. (b) normalized spectrum of the same double-stub resonator and its simulated spectrum (corresponding to a DS resonator with stub lengths L_1=L_2=1.45 μm). Both graphs belong to SU-8 coated sample with dose 900 μC/cm^2.

Therefore to extract the pure spectral response of the double-stub resonator we normalized the output of the double-stub resonator with that of the corresponding bend waveguide (Figure 3.2). We measured the total transmission of each structure in the range λ=1200-1700 nm with steps of 5 nm.

In Figure 4.8(a), we show the output signal measured by lock-in amplifier from 8 μm long slot-waveguide and its corresponding double-stub resonator with designed stub lengths L_1=L_2=0.91 μm. The radius of curvature in both structures is 3 μm and they belong to an SU-8 coated sample fabricated with dose 900 μC/cm^2. The ripples in the slot-waveguide spectrum (blue curve), are due to the Fabry-Perot effect caused by the impedance mismatch between the input and output antennas and the slot-waveguide which results in bouncing of SPP wave between the two antennas. This effect mostly happens in waveguides of shorter lengths.

The comparison of output signals reveals the presence of peak in the output of double-stub resonator around 1600 nm. The shift in resonant wavelength is due to the discrepancies between simulation and fabrication as discussed above. In Figure 4.8(b), we show the output signal of double-stub resonator normalized by its corresponding slot-waveguide (blue curve) along with simulated signal predicted by scattering matrix theory. The stub lengths of the simulated DS resonator are the same as the stub lengths of the designed DS resonator that is: L_1=L_2=0.91μm. The shape of the measured spectrum nearly obeys the simulated spectrum however the location of resonances has been shifted which might be again due to the discrepancies between the dimensions of simulated and fabricated resonators.

In Figure 4.9(a,b), we show the results for DS resonator with designed stub lengths of L_1=L_2=1.39 μm. The waveguide length is 8 μm and the radius of curvature is 3 μm. The results belong to SU-8 coated sample fabricated with dose 900 μC/cm^2. The same arguments stated above for DS resonator of lengths L_1=L_2=0.91 μm holds for this measurement as well. However, to match the simulation and experimental spectra shown in Figure 4.9(b) we set the stub lengths of the simulated DS resonator to L_1=L_2=1.45 μm.

Chapter 5
CONCLUSION

Two-dimensional metal-dielectric-metal (MDM) and three-dimensional slot waveguides (SWG) are the most promising plasmonic interconnects due to their high confinement, wide operational bandwidth, and most importantly their CMOS compatible fabrication. To the best of our knowledge, comparison between general properties of 2D plasmonic MDM and 3D plasmonic slot waveguides has been made; however, comparison between functional devices built out of these two geometries has not been made. This is mostly due to the open nature of the 3D slot-waveguide that results in radiation loss in addition to the inherent ohmic losses which is common in all the plasmonic waveguides. However, we intended to know how far the characteristics of a plasmonic device based on a 3D slot-waveguide can be from its 2D counterpart which uses MDM waveguide as its platform. To answer this question, we selected two plasmonic functional devices namely single-stub and double-stub resonators to compare their 2D and 3D performances. A 3D plasmonic slot-waveguide can come in different variations [44,50] our particular choice was based on having more realistic and practical waveguide which is compatible with CMOS-fab.

We analyzed our structures both theoretically and numerically. For numerical simulations we used the commercial software Lumerical FDTD Solutions which is a finite difference time-domain electromagnetic solver. We fabricated our samples with electron-beam lithography EBL and characterized them with a home-built far-filed cross-polarization reflection microscope setup.

In Chapter 2, we gave the general properties and specifications of the structures that we focused on. We employed scattering matrix theory to analytically investigate the properties of our structures and predict their spectral responses prior to running numerical simulations. We verified our analytical results with the numerical ones.

We showed that scattering matrix can be extended to the 3D plasmonic structures despite of the radiation losses. We found that 3D stub resonators can show similar characteristics to the 2D ones but with degraded performances. Utilizing scattering matrix theory we

provided the guidelines for designing the 2D and 3D stub resonators. We particularly addressed how to choose the stub lengths in 2D and 3D SS and DS resonators without numerically sweeping over the stub lengths that can be a time-consuming process in the 3D simulations. We further, provided the power transmission maps of the 2D and 3D DS resonators versus their stub lengths at the desired wavelength 1550 nm and we specified the regions on these maps that give us plasmonic analogue of electromagnetically induced transparency (PIT).

We found that the 3D double-stub resonators show superior performances compared to the 3D single-resonators which makes them suitable in sensing and filtering applications. Therefore, we focused on their fabrication and experimental characterization.

To reduce the radiation losses from the 3D terminated ends utilizing the knowledge we gained from the properties of the DS resonators we proposed a terminated-end based on the properties of the DS resonators themselves. By addition of DS resonator to the end of the 3D stubs we were able to improve the reflectivity of the 3D terminated-ends and reduce their radiation losses.

In Chapter 3, we emphasized the necessity of fabricating bend waveguides instead of the straight ones and addition of the dipole antenna couplers to the fabricated structures for measurement purposes. In this chapter, the detailed steps of fabrication procedure are provided and fabrication results are illustrated with scanning electron microscope SEM images.

In chapter 4, we provided the schematic of our experimental microscope setup that we used for the characterization of our samples. We demonstrated the various parts of the setup and described the function of some of the optical elements that had critical role. The distinguished aspect of our microscope setup is the use of the lock-in amplifier for measuring the weak output signal from our samples unlike the already published papers in which output signal is measured by integrating over the intensity of the images taken by CCD cameras [55,56]. Finally, we provided the experimental results of the fabricated DS resonators which were in line with our simulation results and revealed the resonance capabilities of the 3D double-stub resonators.

The designed stub resonators can be useful in some applications. For example, by reducing the height of the cladding layer within the evanescent field of the double-stub resonators and adding a sensing layer such as mesoporous silica thin film on top of the cladding layer, the propagating surface plasmon resonances (PSPRs) of a DS resonator can be utilized in plasmon-based sensors [60]. The resonant wavelength and amplitude of the PSPRs can be tuned by varying the stub lengths or the refractive index of the cladding layer. The double-stub resonator can further be utilized in investigation of enhanced light-matter interactions in quantum plasmonic applications via positioning colloidal quantum dot emitters in hotspots within the DS resonator [52].

Appendix A

Derivation of semi-analytic complex transmission (TSS) and reflection (RSS) coefficients of single-stub resonator.

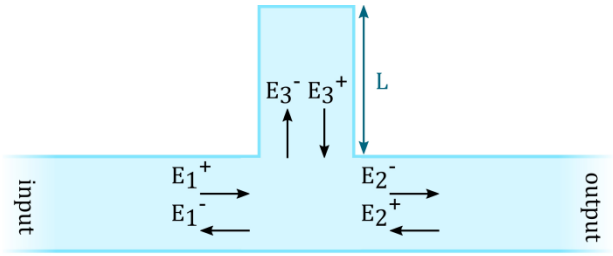

For a 3-port network the general scattering matrix relating the output fields to the input fields at the location of junctions is written as:

$$\begin{pmatrix} E_1^- \\ E_2^- \\ E_3^- \end{pmatrix} = \begin{pmatrix} S_{11} & S_{12} & S_{13} \\ S_{21} & S_{22} & S_{23} \\ S_{31} & S_{32} & S_{33} \end{pmatrix} \begin{pmatrix} E_1^+ \\ E_2^+ \\ E_3^+ \end{pmatrix} \qquad (1)$$

Rewriting the above equation for the single-stub resonator and utilizing the notations that we used for the reflection and transmission coefficients of the geometries that single-stub resonator is composed of, we will get:

$$\begin{pmatrix} E_1^- \\ E_2^- \\ E_3^- \end{pmatrix} = \begin{pmatrix} r_1 & t_1 & t_3 \\ t_1 & r_1 & t_3 \\ t_2 & t_2 & r_3 \end{pmatrix} \begin{pmatrix} E_1^+ \\ E_2^+ \\ E_3^+ \end{pmatrix} \qquad (2)$$

Taking into account that in our case SPP wave is incident from the left to SS resonator, we have $E_2^+ = 0$ and thus we will have:

$$\begin{pmatrix} E_1^- \\ E_2^- \\ E_3^- \end{pmatrix} = \begin{pmatrix} r_1 & 0 & t_3 \\ t_1 & 0 & t_3 \\ t_2 & 0 & r_3 \end{pmatrix} \begin{pmatrix} E_1^+ \\ 0 \\ E_3^+ \end{pmatrix} \qquad (3)$$

Transmission coefficient is defined as:

$$TSS = \frac{E_2^-}{E_1^+} \qquad (4)$$

To obtain the TSS we need to write E_2^- in terms of E_1^+. From Eq. (3) E_2^- can be written as

$$E_2^- = t_1 E_1^+ + t_3 E_3^+ \qquad (5)$$

To have E_2^- fully written in terms of E_1^+, we need to write E_3^+ in terms of E_1^+as well. In single-stub resonator E_3^+ is formed by the portion of the incident SPP wave that enters the stub which is given by $t_2 E_1^+$.

$t_2 E_1^+$ enters the stub propagates a distance *L* which amounts to the phase shift of *exp(ikL)* then reflects back from the stub end with reflection coefficient r_2 and again propagates a distance *L* equivalent to the phase shift *exp(ikL)* toward the stub entrance. At the stub entrance the SPP wave is again reflected back but with the reflection coefficient r_3. The SPP wave entering the stub undergoes this oscillatory motion infinite times before emitting out equally to the right and left of the input waveguide. The summation of all these multiple bounces gives us E_3^+ and is calculated as follows:

$$E_3^+ = t_2 E_1^+ \left(e^{ikL}\, r_2 e^{ikL}\right) + t_2 E_1^+ \left(r_2 e^{2ikL}\right)\left(r_3 r_2 e^{2ikL}\right) +$$

$$t_2 E_1^+ \left(r_2 e^{2ikL}\right)^2 r_3 \left(r_3 r_2 e^{2ikL}\right) + \cdots \qquad (6)$$

$$E_3^+ = t_2 E_1^+ \left(r_2 e^{2ikL}\right)\left[1 + \left(r_3 r_2 e^{2ikL}\right) + \left(r_3 r_2 e^{2ikL}\right)^2 + \cdots\right] \qquad (7)$$

$$E_3^+ = t_2 E_1^+ \frac{r_2 e^{2ikL}}{1 - r_3 r_2 e^{2ikL}} \qquad (8)$$

By substituting Eq. (8) in Eq. (5) we get:

$$E_2^- = t_1 E_1^+ + t_3 \left(t_2 E_1^+ \frac{r_2 e^{2ikL}}{1 - r_3 r_2 e^{2ikL}} \right) \qquad (9)$$

And finally by substituting Eq. (9) in Eq. (4) we will have:

$$TSS = t_1 + \frac{t_2 t_3 r_2 e^{2ikL}}{1 - r_3 r_2 e^{2ikL}} \qquad (10)$$

In a similar manner, the reflection coefficient of the single-stub resonator can be derived as follows.

Reflection coefficient is defined as:

$$RSS = \frac{E_1^-}{E_1^+} \qquad (11)$$

To obtain the RSS we need to write E_1^- in terms of E_1^+. From Eq. (3) E_1^- can be written as

$$E_1^- = r_1 E_1^+ + t_3 E_3^+ \qquad (12)$$

It should be noted that the second term in Eq. (10) is the SPP wave inside the stub that emits out to the right to give the transmission coefficient. The same amount emits to the left of the input waveguide to contribute to the reflection coefficient. Therefore, E_3^+ in Eq. (12) is the same given by Eq. (8).

By substituting E_3^+ in Eq. (12) we get:

$$E_1^- = r_1 E_1^+ + t_3 \left(t_2 E_1^+ \frac{r_2 e^{2ikL}}{1 - r_3 r_2 e^{2ikL}} \right) \qquad (13)$$

By substituting Eq. (13) in Eq. (11) we will have:

$$RSS = r_1 + \frac{t_2 t_3 r_2 e^{2ikL}}{1 - r_3 r_2 e^{2ikL}}$$

Appendix B

Derivation of semi-analytic complex transmission (TDS) and reflection (RDS) coefficients of double-stub resonator.

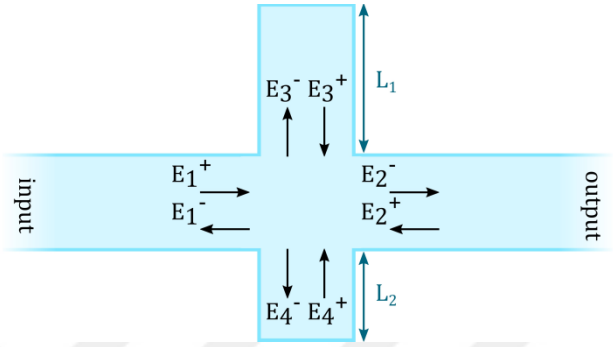

For a 4-port network the general scattering matrix relating the output fields to the input fields at the location of junctions is written as:

$$\begin{pmatrix} E_1^- \\ E_2^- \\ E_3^- \\ E_4^- \end{pmatrix} = \begin{pmatrix} S_{11} & S_{12} & S_{13} & S_{14} \\ S_{21} & S_{22} & S_{23} & S_{24} \\ S_{31} & S_{32} & S_{33} & S_{34} \\ S_{41} & S_{42} & S_{43} & S_{44} \end{pmatrix} \begin{pmatrix} E_1^+ \\ E_2^+ \\ E_3^+ \\ E_4^+ \end{pmatrix} \qquad (1)$$

Rewriting the above equation for the double-stub resonator and utilizing the notations that we used for the reflection and transmission coefficients of the geometries that double-stub resonator is composed of, we will get:

$$\begin{pmatrix} E_1^- \\ E_2^- \\ E_3^- \\ E_4^- \end{pmatrix} = \begin{pmatrix} r_4 & t_4 & t_5 & t_5 \\ t_4 & r_4 & t_5 & t_5 \\ t_5 & t_5 & r_4 & t_4 \\ t_5 & t_5 & t_4 & r_4 \end{pmatrix} \begin{pmatrix} E_1^+ \\ E_2^+ \\ E_3^+ \\ E_4^+ \end{pmatrix} \qquad (2)$$

Taking into account that in our case SPP wave is incident from the left to DS resonator, we have $E_2^+ = 0$ and thus we will have:

$$\begin{pmatrix} E_1^- \\ E_2^- \\ E_3^- \\ E_4^- \end{pmatrix} = \begin{pmatrix} r_4 & 0 & t_5 & t_5 \\ t_4 & 0 & t_5 & t_5 \\ t_5 & 0 & r_4 & t_4 \\ t_5 & 0 & t_4 & r_4 \end{pmatrix} \begin{pmatrix} E_1^+ \\ 0 \\ E_3^+ \\ E_4^+ \end{pmatrix} \qquad (3)$$

Transmission coefficient is defined as:

$$TDS = \frac{E_2^-}{E_1^+} \qquad (4)$$

To obtain the *TDS* we need to write E_2^- in terms of E_1^+. From Eq. (3) E_2^- can be written as

$$E_2^- = t_4 E_1^+ + t_5 E_3^+ + t_5 E_4^+ \qquad (5)$$

To have E_2^- fully written in terms of E_1^+, we need to write E_3^+ and E_4^+ in terms of E_1^+as well. In DS resonator, due to symmetry, $t_5 E_1^+$ portion of the incident SPP wave enters the upper stub (3rd port) and $t_5 E_1^+$ portion enters the lower stub (4th port). Both of these portions have contributions in building up E_3^+ and E_4^+ waves.

E_3^+ is formed as follows: $t_5 E_1^+$ enters the *upper* stub and oscillates there infinite times to give E_{33}^{+0}, then $t_4 E_{33}^{+0}$ enters *lower* stub and after oscillating there infinite times reenters *upper* stub and there undergoes infinite oscillation again to give E_{33}^{+1} and this continues on and on.

However, besides the portion of the SPP wave that enters *lower* stub by means of the *upper* stub, $t_5 E_1^+$ portion of the incident SPP wave that directly enters *lower* stub has also contribution in building up E_3^+ as follows: $t_5 E_1^+$enters *lower* stub oscillates there infinite times to give E_{44}^{+0}, then $t_4 E_{44}^{+0}$ enters *upper* stub and oscillates there infinite times to give E_{34}^{+0} , and this procedure continues on and on.

Field components denoted by subscript 33 are those built up by $t_5 E_1^+$ that directly enters *upper* stub, however, components denoted by 34 are those built up by $t_5 E_1^+$ that enters lower stub indirectly that is by means of *upper* stub.

Therefore, E_3^+ wave can be decomposed into two terms as follows:

$$E_3^+ = E_{33}^+ + E_{34}^+ \qquad (6)$$

$$= E_{33}^{+0} + E_{33}^{+1} + E_{33}^{+2} + \cdots + E_{34}^{+0} + E_{34}^{+1} + E_{34}^{+2} + \cdots$$

The same procedure holds in the formation of E_4^+ wave:

$$E_4^+ = E_{44}^+ + E_{43}^+ \qquad (7)$$

$$= E_{44}^{+0} + E_{44}^{+1} + E_{44}^{+2} + \cdots + E_{43}^{+0} + E_{43}^{+1} + E_{43}^{+2} + \cdots$$

where field components denoted by subscript 44 are those built up by $t_5E_1^+$ that directly enters lower stub, however, components denoted by 43 are those built up by $t_5E_1^+$ that enters lower stub indirectly that is by means of upper stub.

Starting from Eq. (7), and assuming that the upper stub has length L_1 and the lower stub has length L_2, each of the terms stated in this equation is calculated as follows:

$$E_{33}^{+0} = t_5E_1^+\left(e^{ikL_1}r_2e^{ikL_1}\right) + \left(t_5r_2e^{2ikL_1}E_1^+\right)r_4\left(e^{ikL_1}r_2e^{ikL_1}\right) +$$

$$\left(t_5r_4{r_2}^2e^{4ikL_1}E_1^+\right)r_4\left(e^{ikL_1}r_2e^{ikL_1}\right) + \cdots$$

$$= t_5r_2e^{2ikL_1}E_1^+\left[1 + r_2r_4e^{2ikL_1} + (r_2r_4e^{2ikL_1})^2 + \cdots\right]$$

$$= \frac{t_5r_2e^{2ikL_1}}{1 - r_2r_4e^{2ikL_1}}E_1^+ \qquad (8)$$

By defining *A* as:

$$A = \frac{r_2e^{2ikL_1}}{1 - r_2r_4e^{2ikL_1}} \qquad (9)$$

Equation (8) can be simplified as:

$$\mathrm{E}_{33}^{+0} = (\mathrm{t}_5\mathrm{A})\ \mathrm{E}_1^+ \qquad (10)$$

Now, E_{33}^{+0} enters the lower stub, oscillates there infinite times and returns to the upper stub and again oscillates there infinite times to give E_{33}^{+1} as calculated below:

$$E_{33}^{+1} = (t_4 E_{33}^{+0}) \left(\frac{r_2 e^{2ikL_2}}{1 - r_2 r_4 e^{2ikL_2}} \right) t_4 \left(\frac{r_2 e^{2ikL_1}}{1 - r_2 r_4 e^{2ikL_1}} \right)$$

$$= \frac{r_2 e^{2ikL_1}}{1 - r_2 r_4 e^{2ikL_1}} \times \frac{r_2 e^{2ikL_2}}{1 - r_2 r_4 e^{2ikL_2}} \; t_4^2 E_{33}^{+0} \qquad (11)$$

By defining *B* as:

$$B = \frac{\mathrm{r_2 e^{2ikL_2}}}{1 - \mathrm{r_2 r_4 e^{2ikL_2}}} \qquad (12)$$

Equation (11) can be simplified as:

$$E_{33}^{+1} = (AB{t_4}^2) E_{33}^{+0} \qquad (13)$$

Now, E_{33}^{+1} goes under the same procedure as E_{33}^{+0} to give E_{33}^{+2} as calculated below:

$$E_{33}^{+2} = (t_4 E_{33}^{+1}) \left(\frac{r_2 e^{2ikL_2}}{1 - r_2 r_4 e^{2ikL_2}} \right) t_4 \left(\frac{r_2 e^{2ikL_1}}{1 - r_2 r_4 e^{2ikL_1}} \right)$$

$$= (AB{t_4}^2) \; E_{33}^{+1} \qquad (14)$$

By substituting Eq. (13) in Eq. (14) we get:

$$E_{33}^{+2} = (AB{t_4}^2)(AB{t_4}^2) E_{33}^{+0}$$

$$= (AB{t_4}^2)^2 \; E_{33}^{+0} \qquad (15)$$

This procedures continues infinite times, however, calculation of a few terms is sufficient to derive E_{33}^{+}.

By substituting Eq. (13) and Eq. (15) back into first term of Eq. (6) we get:

$$E_{33}^{+} = E_{33}^{+0} + E_{33}^{+1} + E_{33}^{+3} + \cdots$$

$$= E_{33}^{+0} + (AB{t_4}^2) E_{33}^{+0} + (AB{t_4}^2)^2 E_{33}^{+0} + \cdots$$

$$= [1 + AB{t_4}^2 + (AB{t_4}^2)^2 + \cdots] E_{33}^{+0}$$

$$= \frac{E_{33}^{+0}}{1 - AB{t_4}^2} \qquad (16)$$

By substituting Eq. (10) into Eq. (16) we get:

$$E_{33}^{+} = \frac{At_5}{1 - AB{t_4}^2} E_1^{+} \qquad (17)$$

To derive the second term of Eq. (6) that is E_{34}^{+}, we will consider the $t_5 E_1^{+}$portion of the incident SPP wave that enters *lower* stub first.

$$E_{44}^{+0} = t_5 E_1^{+}\left(e^{ikL_2} r_2 e^{ikL_2}\right) + \left(t_5 r_2 e^{2ikL_2} E_1^{+}\right) r_4 \left(e^{ikL_2} r_2 e^{ikL_2}\right) +$$

$$\left(t_5 r_4 {r_2}^2 e^{4ikL_2} E_1^{+}\right) r_4 \left(e^{ikL_2} r_2 e^{ikL_2}\right) + \cdots$$

$$= t_5 r_2 e^{2ikL_2} E_1^{+}\left[1 + r_2 r_4 e^{2ikL_2} + (r_2 r_4 e^{2ikL_2})^2 + \cdots\right]$$

$$= \frac{t_5 r_2 e^{2ikL_2}}{1 - r_2 r_4 e^{2ikL_2}} E_1^{+} \qquad (18)$$

Therefore

$$E_{44}^{+0} = (t_5 B) E_1^{+} \qquad (19)$$

E_{44}^{+0}enters the *upper* stub, oscillates there infinite times to give E_{34}^{+0}:

$$E_{34}^{+0} = (t_4 E_{44}^{+0}) \frac{r_2 e^{2ikL_1}}{1 - r_2 r_4 e^{2ikL_1}}$$

$$= (t_4 A) E_{44}^{+0} \qquad (20)$$

E_{34}^{+0}, will enter the *lower* stub, oscillate there multiple times and will turn back to the *upper* stub and oscillate there infinite times to give:

$$E_{34}^{+1} = (t_4 E_{34}^{+0}) \left(\frac{r_2 e^{2ikL_2}}{1 - r_2 r_4 e^{2ikL_2}}\right) t_4 \left(\frac{r_2 e^{2ikL_1}}{1 - r_2 r_4 e^{2ikL_1}}\right)$$

$$= (AB{t_4}^2)\, E_{34}^{+0} \qquad (21)$$

E_{34}^{+1} will undergo the same procedure as E_{34}^{+0} to give E_{34}^{+2}:

$$E_{34}^{+2} = (t_4 E_{34}^{+1}) \left(\frac{r_2 e^{2ikL_2}}{1 - r_2 r_4 e^{2ikL_2}} \right) t_4 \left(\frac{r_2 e^{2ikL_1}}{1 - r_2 r_4 e^{2ikL_1}} \right)$$

$$= (ABt_4{}^2)\, E_{34}^{+1} \qquad (22)$$

By substituting Eq. (21) into Eq. (22) we get:

$$E_{34}^{+2} = (ABt_4{}^2)(ABt_4{}^2)\, E_{34}^{+0}$$

$$= (ABt_4{}^2)^2\, E_{34}^{+0} \qquad (23)$$

Finally, by substituting Eq. (21) and Eq. (23) into the second term of Eq. (6) we get:

$$E_{34}^{+} = E_{34}^{+0} + E_{34}^{+1} + E_{34}^{+2} + \cdots$$

$$= E_{34}^{+0} + \left(ABt_4{}^2\right) E_{34}^{+0} + (ABt_4{}^2)^2 E_{34}^{+0} + \cdots$$

$$= E_{34}^{+0} \left[1 + ABt_4{}^2 + \left(ABt_4{}^2\right)^2 + \cdots \right]$$

$$= \frac{E_{34}^{+0}}{1 - ABt_4{}^2} \qquad (24)$$

Substituting Eq. (20) into Eq. (24) gives:

$$E_{34}^{+} = \frac{t_4 A}{1 - ABt_4{}^2} E_{44}^{+0} \qquad (25)$$

Substituting Eq. (19) into Eq. (25) gives:

$$E_{34}^{+} = \frac{ABt_4 t_5}{1 - ABt_4{}^2} E_1^{+} \qquad (26)$$

E_{44}^{+} and E_{43}^{+}can be calculated in the same way as $E_{33}^{+}$and E_{34}^{+}. $t_5 E_1^{+}$ enters the lower stub and oscillates there infinite times to give E_{44}^{+0} which is given by Eq. (19). E_{44}^{+0} enters the upper stub and oscillates there infinite times to give E_{44}^{+1}:

$$E_{44}^{+1} = (t_4 E_{44}^{+0}) \left(\frac{r_2 e^{2ikL_1}}{1 - r_2 r_4 e^{2ikL_1}} \right) t_4 \left(\frac{r_2 e^{2ikL_2}}{1 - r_2 r_4 e^{2ikL_2}} \right) \qquad (27)$$

By substituting *A* and *B* in Eq. (27) we get:

$$E_{44}^{+1} = \left(AB{t_4}^2 \right) E_{44}^{+0} \qquad (28)$$

Now, E_{44}^{+1} enters the upper stub again and oscillates there infinite times to give E_{44}^{+2}:

$$E_{44}^{+2} = (t_4 E_{44}^{+1}) \left(\frac{r_2 e^{2ikL_1}}{1 - r_2 r_4 e^{2ikL_1}} \right) t_4 \left(\frac{r_2 e^{2ikL_2}}{1 - r_2 r_4 e^{2ikL_2}} \right) \qquad (29)$$

By substituting *A* and *B*, Eq. (29) can be simplified as:

$$\begin{aligned} E_{44}^{+2} &= \left(AB{t_4}^2 \right) E_{44}^{+1} \\ &= \left(AB{t_4}^2 \right) \left(AB{t_4}^2 \right) E_{44}^{+0} \\ &= \left(AB{t_4}^2 \right)^2 E_{44}^{+0} \end{aligned} \qquad (30)$$

By substituting Eq. (28) and Eq. (30) into first term of Eq. (7) we get:

$$\begin{aligned} E_{44}^{+} &= E_{44}^{+0} + E_{44}^{+1} + E_{44}^{+2} + \cdots \\ &= E_{44}^{+0} + \left(AB{t_4}^2 \right) E_{44}^{+0} + \left(AB{t_4}^2 \right)^2 E_{44}^{+0} + \cdots \\ &= E_{44}^{+0} \left[1 + AB{t_4}^2 + (AB{t_4}^2)^2 + \cdots \right] \\ &= \frac{E_{44}^{+0}}{1 - AB{t_4}^2} \end{aligned} \qquad (31)$$

By substituting Eq. (19) into Eq. (31) we get:

$$E_{44}^{+} = \frac{Bt_5}{1 - AB{t_4}^2} E_1^{+} \qquad (32)$$

E_{43}^{+}, which is built up by $t_5 E_1^{+}$ portion of the incident SPP wave that first enters *upper* port, is calculated in the same way as E_{44}^{+0}. $t_5 E_1^{+}$ enters upper port and oscillates there infinite times to give E_{33}^{+0} which is given by Eq. (10), E_{33}^{+0} enters *lower* port and oscillates

there infinite times to give E_{43}^{+0}, and this continues on and on.

$$E_{43}^{+0} = (t_4 E_{33}^{+0})\left(\frac{r_2 e^{2ikL_2}}{1 - r_2 r_4 e^{2ikL_2}}\right) \qquad (33)$$

By substituting Eq. (10) into Eq. (33) we get:

$$E_{43}^{+0} = t_4(t_5 A E_1^{+})B$$

$$= (t_4 t_5 AB)E_1^{+} \qquad (34)$$

Similarly, E_{43}^{+0}enters upper stub oscillates there infinite times and returns to lower stub again and oscillates there infinite times to give E_{43}^{+1}:

$$E_{43}^{+1} = (t_4 E_{43}^{+0})\left(\frac{r_2 e^{2ikL_1}}{1 - r_2 r_4 e^{2ikL_1}}\right) t_4 \left(\frac{r_2 e^{2ikL_2}}{1 - r_2 r_4 e^{2ikL_2}}\right)$$

$$= \left(AB{t_4}^2\right)E_{43}^{+0} \qquad (35)$$

Similarly, E_{43}^{+2} can be obtained as:

$$E_{43}^{+2} = (t_4 E_{43}^{+1})\left(\frac{r_2 e^{2ikL_1}}{1 - r_2 r_4 e^{2ikL_1}}\right) t_4 \left(\frac{r_2 e^{2ikL_2}}{1 - r_2 r_4 e^{2ikL_2}}\right)$$

$$= \left(AB{t_4}^2\right)E_{43}^{+1} \qquad (36)$$

By substituting Eq. (35) into Eq. (36) we get:

$$E_{43}^{+2} = \left(AB{t_4}^2\right)^2 E_{43}^{+0} \qquad (37)$$

Finally, by substituting Eq. (35) and Eq. (37) into the second term of Eq. (7) we get:

$$E_{43}^{+} = E_{43}^{+0} + E_{43}^{+1} + E_{43}^{+2} + \cdots$$

$$= E_{43}^{+0} + \left(AB{t_4}^2\right)E_{43}^{+0} + \left(AB{t_4}^2\right)^2 E_{43}^{+0} + \cdots$$

$$= E_{43}^{+0}[1 + {t_4}^2 AB + (t_4{}^2 AB)^2 + \cdots]$$

$$= \frac{E_{43}^{+0}}{1 - AB{t_4}^2} \qquad (38)$$

By substituting Eq. (34) into Eq. (38) we get:

$$E_{43}^{+} = \frac{t_4 t_5 AB}{1 - {t_4}^2 AB} E_1^{+} \qquad (39)$$

By summing the first and second terms of Eq. (6) which are given by Eq. (17) and Eq. (26), respectively, we get:

$$E_3^{+} = E_{33}^{+} + E_{34}^{+}$$

$$= \frac{At_5}{1 - AB{t_4}^2} E_1^{+} + \frac{ABt_4 t_5}{1 - AB{t_4}^2} E_1^{+}$$

$$= \left(\frac{At_5 + ABt_4 t_5}{1 - AB{t_4}^2}\right) E_1^{+} \qquad (40)$$

By summing the first and second terms of Eq. (7) which are given by Eq. (32) and Eq. (39), respectively, we get:

$$E_4^{+} = E_{44}^{+} + E_{43}^{+}$$

$$= \frac{Bt_5}{1 - AB{t_4}^2} E_1^{+} + \frac{ABt_4 t_5}{1 - AB{t_4}^2} E_1^{+}$$

$$= \left(\frac{Bt_5 + ABt_4 t_5}{1 - AB{t_4}^2}\right) E_1^{+} \qquad (41)$$

Substituting Eq. (40) and Eq. (41) into Eq. (5) gives:

$$E_2^{-} = t_4 E_1^{+} + t_5 E_3^{+} + t_5 E_4^{+}$$

$$= t_4 E_1^{+} + t_5 \left(\frac{At_5 + ABt_4 t_5}{1 - AB{t_4}^2}\right) E_1^{+} + t_5 \left(\frac{Bt_5 + ABt_4 t_5}{1 - AB{t_4}^2}\right) E_1^{+} \qquad (42)$$

Finally, by substituting Eq. (41) into Eq. (4) we get:

$$TDS = \frac{E_2^-}{E_1^+} = t_4 + \frac{{t_5}^2(A+B)}{1-AB{t_4}^2} + \frac{2t_4t_5^2AB}{1-AB{t_4}^2} \qquad (43)$$

By defining s_1 and s_2 parameters as:

$$s_1 = \frac{e^{2ikL_1}}{r_2} \qquad (44)$$

$$s_2 = \frac{e^{2ikL_2}}{r_2} \qquad (45)$$

Parameter A defined by Eq. (9) can be rewritten as:

$$A = \frac{r_2 e^{2ikL_1}}{1 - r_2 r_4 e^{2ikL_1}}$$

$$= \frac{1}{\frac{1}{r_2 e^{2ikL_1}} - r_4} \qquad (46)$$

Substituting Eq. (44) into Eq. (46) we get:

$$A = \frac{1}{s_1 - r_4} \qquad (47)$$

Similarly, parameter *B* defined by Eq. (12) can be rewritten as:

$$B = \frac{1}{s_2 - r_4} \qquad (48)$$

Therefore, the summation and multiplication of *A* and *B* which appear in Eq. (43) can be written as:

$$A + B = \frac{1}{s_1 - r_4} + \frac{1}{s_2 - r_4}$$

$$= \frac{s_2 - r_4 + s_1 - r_4}{(s_1 - r_4)(s_2 - r_4)}$$

$$= \frac{s_1 + s_2 - 2r_4}{(s_1 - r_4)(s_2 - r_4)} \qquad (49)$$

$$AB = \frac{1}{(s_1 - r_4)(s_2 - r_4)} \qquad (50)$$

Finally, by substituting Eq. (49) and Eq. (5) into Eq. (43) we can simplify *TDS* as:

$$TDS = \frac{E_2^-}{E_1^+} = t_4 + \frac{{t_5}^2(A + B)}{1 - AB{t_4}^2} + \frac{2t_4 t_5^2 AB}{1 - AB{t_4}^2} \qquad (51)$$

$$TDS = t_4 + {t_5}^2\left[\frac{s_1 + s_2 - 2r_4}{(s_1 - r_4)(s_2 - r_4)}\right] \times \frac{1}{1 - \frac{{t_4}^2}{(s_1 - r_4)(s_2 - r_4)}} + 2t_4 t_5^2 \frac{\frac{1}{(s_1 - r_4)(s_2 - r_4)}}{1 - \frac{{t_4}^2}{(s_1 - r_4)(s_2 - r_4)}}$$

$$= t_4 + \frac{t_5^2\,(s_1 + s_2 - 2r_4)}{(s_1 - r_4)(s_2 - r_4) - {t_4}^2} + \frac{2t_4 t_5^2}{(s_1 - r_4)(s_2 - r_4) - {t_4}^2}$$

$$= t_4 - \frac{{t_5}^2(s_1 + s_2 - 2r_4)}{{t_4}^2 - (s_1 - r_4)(s_2 - r_4)} - \frac{2t_4 t_5^2}{{t_4}^2 - (s_1 - r_4)(s_2 - r_4)}$$

$$= t_4 - \frac{{t_5}^2(2t_4 - 2r_4 + s_1 + s_2)}{{t_4}^2 - (s_1 - r_4)(s_2 - r_4)} \qquad (52)$$

Defining the second term in Eq. (52) as:

$$C = \frac{{t_5}^2(2t_4 - 2r_4 + s_1 + s_2)}{{t_4}^2 - (s_1 - r_4)(s_2 - r_4)} \qquad (53)$$

Equation (51) can be simplifies as:

$$TDS = t_4 - C \qquad (54)$$

In a similar way, *RDS* reflection coefficient can be derived as follows. *RDS* is defined as:

$$RDS = \frac{E_1^-}{E_1^+} \qquad (55)$$

From Eq. (3) E_1^- can be written as:

$$E_1^- = r_4 E_1^+ + t_5 E_3^+ + t_5 E_4^+ \qquad (56)$$

The summation of the second and third terms in Eq. (48) is already calculated in the derivation of *TDS* formula and is given in Eq. (42). Therefore, following the same steps taken after Eq. (42) we can derive the formula for *RDS* as:

$$RDS = r_4 - C \qquad (57)$$

Appendix C

Comparing power reflection and transmission coefficients of 2D and 3D geometries depicted in Figure 2.9(a-d) and Figure 2.10(a-d), obtained by point time monitor (PTM) and mode expansion monitor (EXPM) methods.

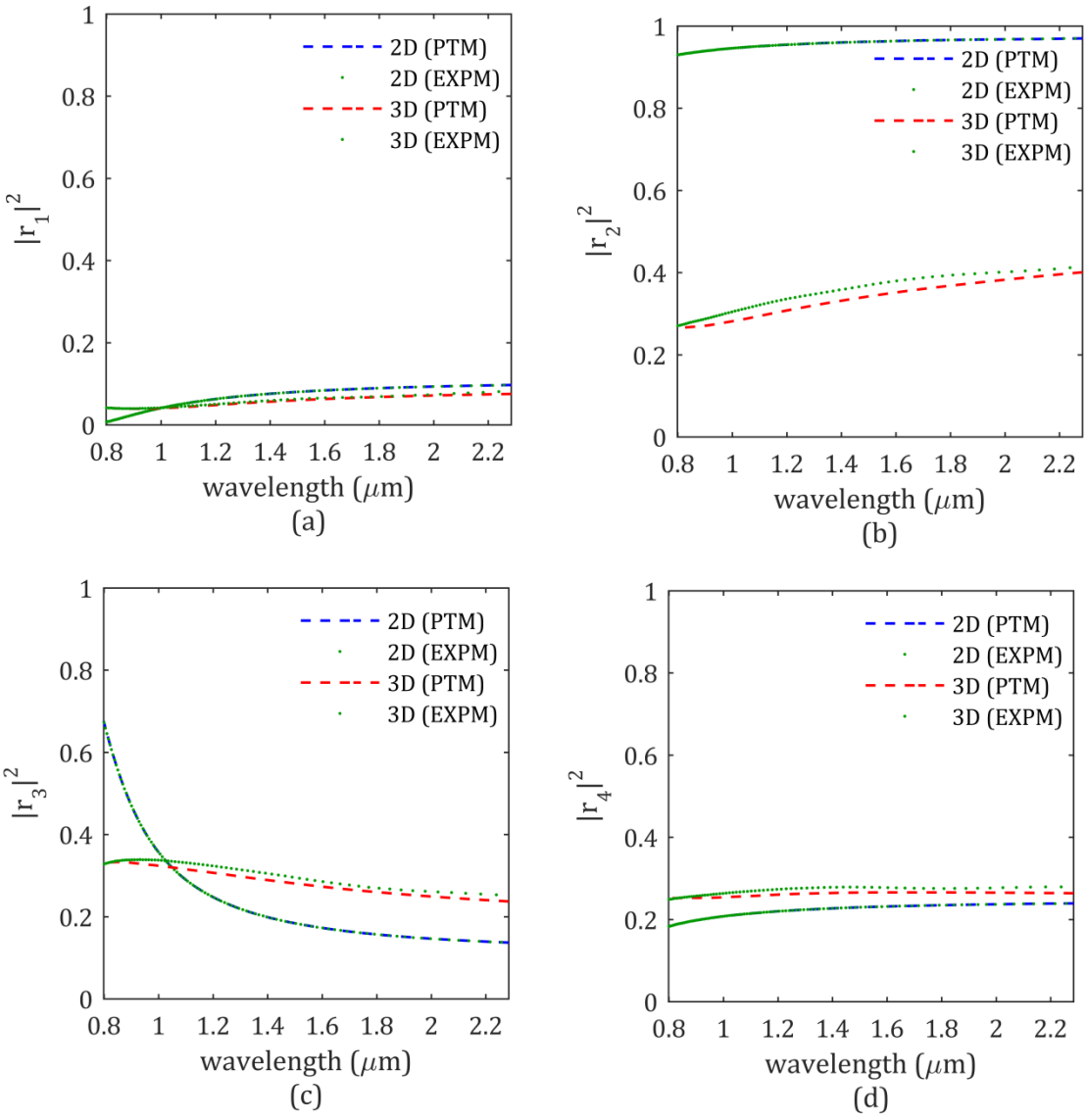

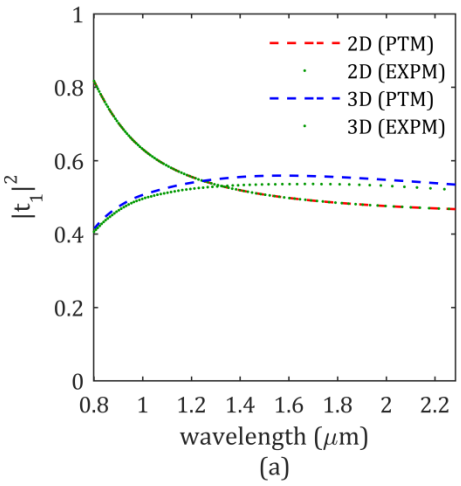
2D (PTM)
2D (EXPM)
3D (PTM)
3D (EXPM)
$|t_1|^2$
wavelength (μm)
(a)

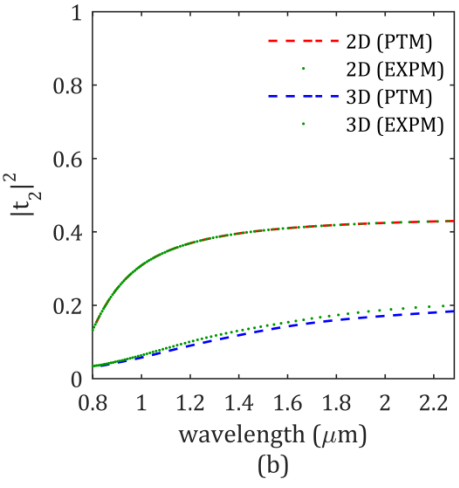
2D (PTM)
2D (EXPM)
3D (PTM)
3D (EXPM)
$|t_2|^2$
wavelength (μm)
(b)

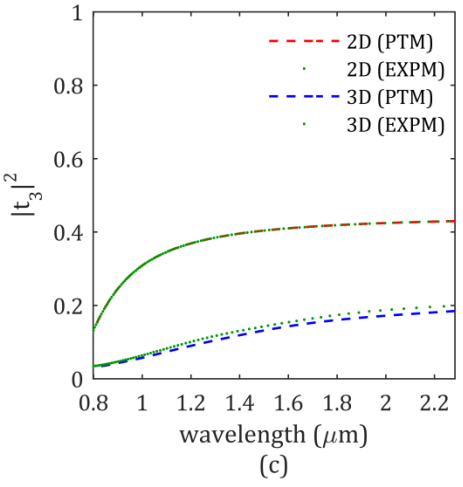
2D (PTM)
2D (EXPM)
3D (PTM)
3D (EXPM)
$|t_3|^2$
wavelength (μm)
(c)

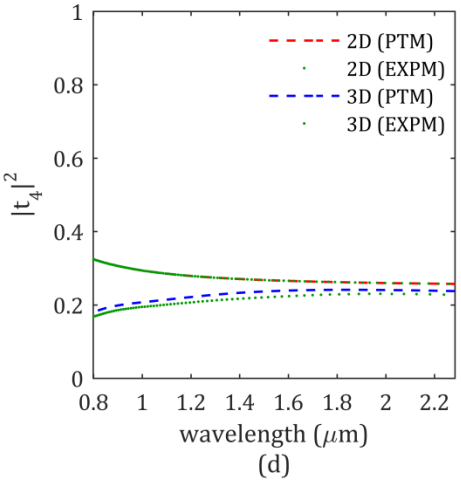
2D (PTM)
2D (EXPM)
3D (PTM)
3D (EXPM)
$|t_4|^2$
wavelength (μm)
(d)

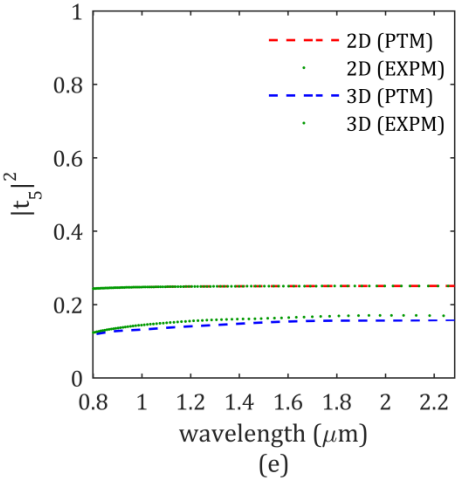
2D (PTM)
2D (EXPM)
3D (PTM)
3D (EXPM)
$|t_5|^2$
wavelength (μm)
(e)

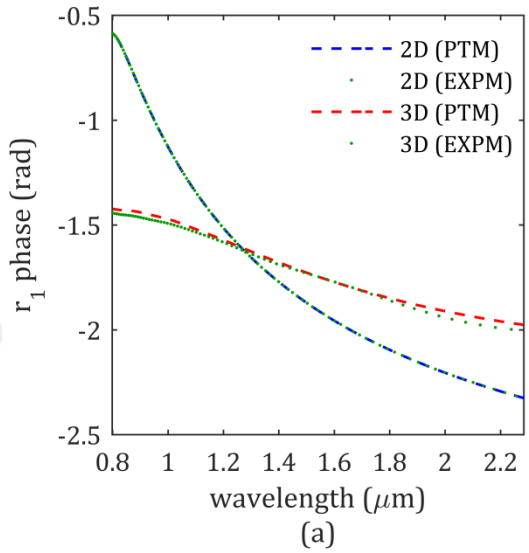
2D (PTM)
2D (EXPM)
3D (PTM)
3D (EXPM)
r1 phase (rad)
wavelength (μm)
(a)

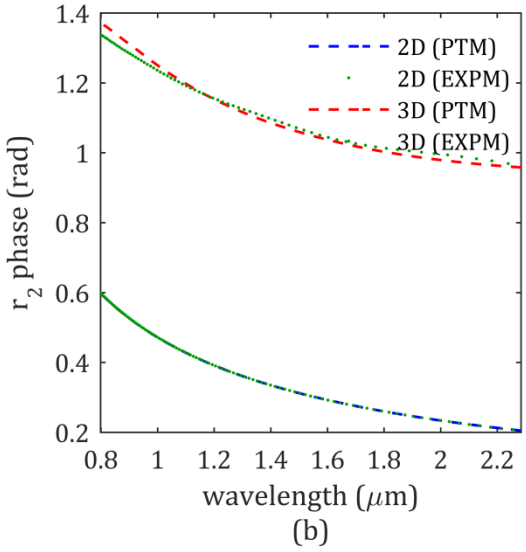
2D (PTM)
2D (EXPM)
3D (PTM)
3D (EXPM)
r2 phase (rad)
wavelength (μm)
(b)

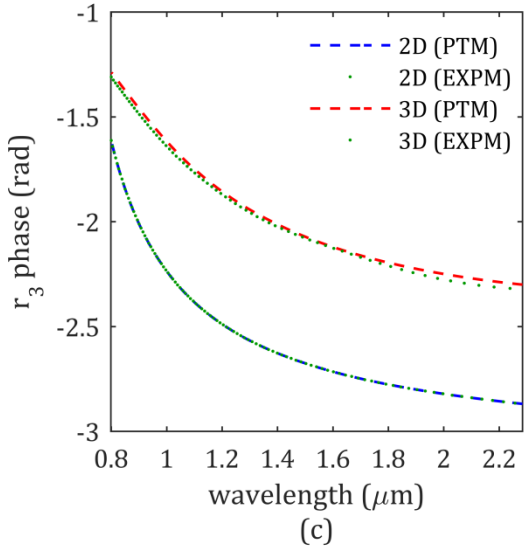
2D (PTM)
2D (EXPM)
3D (PTM)
3D (EXPM)
r3 phase (rad)
wavelength (μm)
(c)

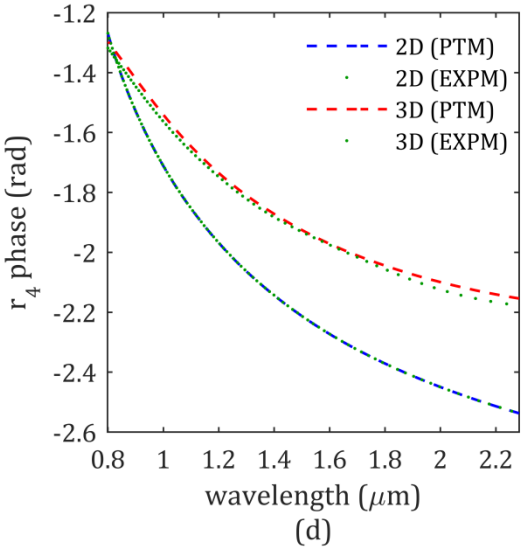
2D (PTM)
2D (EXPM)
3D (PTM)
3D (EXPM)
r4 phase (rad)
wavelength (μm)
(d)

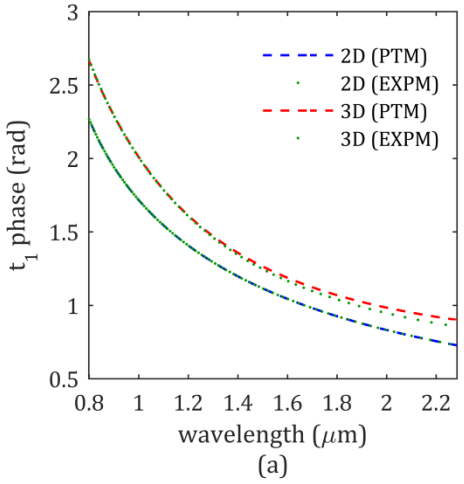
2D (PTM)
2D (EXPM)
3D (PTM)
3D (EXPM)
t1 phase (rad)
wavelength (μm)
(a)

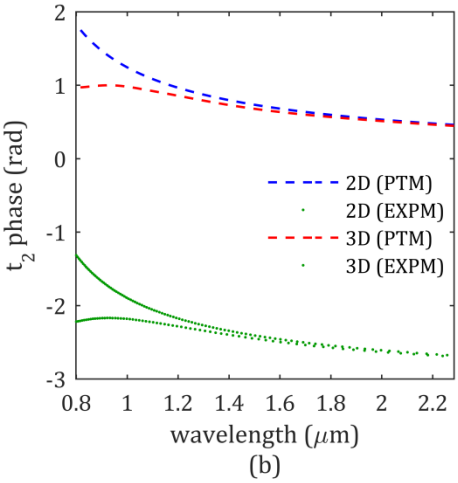
2D (PTM)
2D (EXPM)
3D (PTM)
3D (EXPM)
t2 phase (rad)
wavelength (μm)
(b)

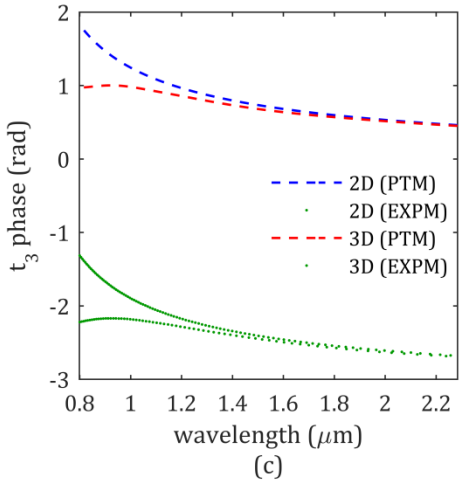
2D (PTM)
2D (EXPM)
3D (PTM)
3D (EXPM)
t3 phase (rad)
wavelength (μm)
(c)

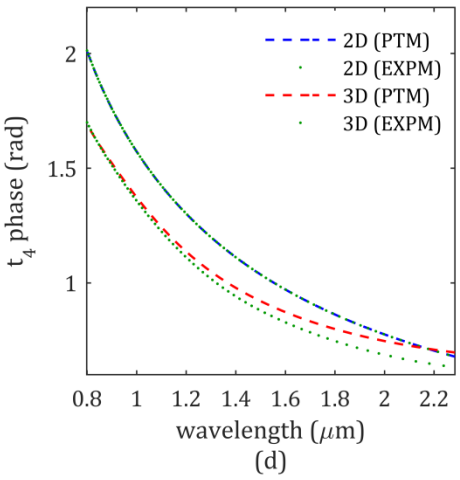
2D (PTM)
2D (EXPM)
3D (PTM)
3D (EXPM)
t4 phase (rad)
wavelength (μm)
(d)

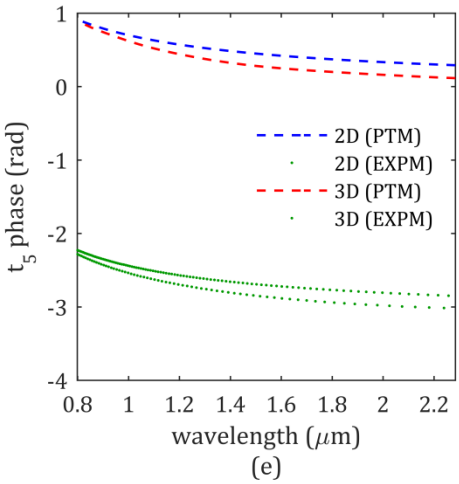
2D (PTM)
2D (EXPM)
3D (PTM)
3D (EXPM)
t5 phase (rad)
wavelength (μm)
(e)

References

[1] G. E. Moore, “Cramming more components onto integrated circuits,” Electronics **38**, 114 (1965).

[2] J. A. Davis, R. Venkatesan, A. Kaloyeros, M. Beylansky, S. J. Souri, K. Banerjee, K. C. Saraswat, A. Rahman, R. Reif, and J. D. Meindl, "Interconnect limits on gigascale integration (GSI) in the 21st century," Proceedings of the IEEE **89**, 305-324 (2001).

[3] David A. B. Miller, “Attojoule Optoelectronics for Low-Energy Information Processing and Communications: a Tutorial Review”, arXiv:1609.05510 [physics.optics] (2016).

[4] J. A. Conway, S. Sahni, and T. Szkopek, "Plasmonic interconnects versus conventional interconnects: a comparison of latency, crosstalk and energy costs," Opt. Express 15, 4474-4484 (2007).

[5] W. Steinhögl, G. Schindler, G. Steinlesberger, and M. Engelhardt, "Size-dependent resistivity of metallic wires in the mesoscopic range," Physical Review B 66, 075414 (2002).

[6] W. Steinhögl, G. Schindler, G. Steinlesberger, M. Traving, and M. Engelhardt, "Comprehensive study of the resistivity of copper wires with lateral dimensions of 100 nm and smaller," Journal of Applied Physics 97, 023706 (2005).

[7] N. Kinsey, M. Ferrera, V. Shalaev, A. Boltasseva, "A platform for practical plasmonics", (2014)

[8] W. Van Heddeghem, S. Lambert, B. Lannoo, D. Colle, M. Pickavet, and P. Demeester, "Trends in worldwide ICT electricity consumption from 2007 to 2012," Computer Communications 50, 64-76 (2014).

[9] D. Miller, "Device Requirements for Optical Interconnects to CMOS Silicon Chips," in Integrated Photonics Research, Silicon and Nanophotonics and Photonics in Switching, OSA Technical Digest (CD) (Optical Society of America, 2010), PMB3.

[10] L. Novotny, B. Hecht, Principles of Nano-Optics (Cambridge University Press, 2012).

[11] J. A. Dionne, L. A. Sweatlock, H. A. Atwater, and A. Polman, "Plasmon slot waveguides: Towards chip-scale propagation with subwavelength-scale localization," Physical Review B 73, 035407 (2006).

[12] E. Ozbay, "Plasmonics: Merging Photonics and Electronics at Nanoscale Dimensions," Science 311, 189-193 (2006).

[13] G. Veronis and S. Fan, "Bends and splitters in metal-dielectric-metal subwavelength plasmonic waveguides," Applied Physics Letters 87, 131102 (2005).

[14] S. Rakheja and V. Kumar, "Comparison of electrical, optical and plasmonic on-chip interconnects based on delay and energy considerations," in Thirteenth International Symposium on Quality Electronic Design (ISQED), 732-739, (2012).

[15] "International Technology Roadmap for Semiconductors, 2005 Edition, Interconnect" http://www.itrs.net/Links/2005ITRS/Interconnect2005/Interconnect2005.pdf.

[16] M. T. Hill, Y.-S. Oei, B. Smalbrugge, Y. Zhu, T. de Vries, P. J. van Veldhoven, F. W. M. van Otten, T. J. Eijkemans, J. P. Turkiewicz, H. de Waardt, E. J. Geluk, S.-H. Kwon, Y.-H. Lee, R. Notzel, and M. K. Smit, "Lasing in metallic-coated nanocavities," Nat Photon 1, 589-594 (2007).

[17] J. A. Dionne, K. Diest, L. A. Sweatlock, and H. A. Atwater, "PlasMOStor: A Metal−Oxide−Si Field Effect Plasmonic Modulator," Nano Letters 9, 897-902 (2009).

[18] W. Cai, J. S. White, and M. L. Brongersma, "Compact, High-Speed and Power-Efficient Electrooptic Plasmonic Modulators," Nano Letters 9, 4403-4411 (2009).

[19] A. Melikyan, N. Lindenmann, S. Walheim, P. M. Leufke, S. Ulrich, J. Ye, P. Vincze, H. Hahn, T. Schimmel, C. Koos, W. Freude, and J. Leuthold, "Surface plasmon polariton absorption modulator," Opt. Express 19, 8855-8869 (2011).

[20] H. M. G. Wassel, M. Tiwari, J. K. Valamehr, L. Theogarajan, J. Dionne, F. T. Chong, T. Sherwood, "Towards chip-scale plasmonic interconnects." Workshop on the Interaction between Nanophotonic Devices and Systems (WINDS), (2010).

[21] A. Melikyan, M. Sommer, A. Muslija, M. Kohl, S. Muehlbrandt, A. Mishra, V. Calzadilla, Y. Justo, J. P. Mart, x00Ed, P. nez, I. Tomkos, A. Scandurra, D. V. Thourhout, Z. Hens, M. Smit, W. Freude, C. Koos, and J. Leuthold, "Chip-to-chip plasmonic interconnects and the activities of EU project NAVOLCHI," in 2012 14th International Conference on Transparent Optical Networks (ICTON), 2012), 1-3.

[22] J.-C. Weeber, A. Dereux, C. Girard, J. R. Krenn, and J.-P. Goudonnet, "Plasmon polaritons of metallic nanowires for controlling submicron propagation of light," Physical Review B 60, 9061-9068 (1999).

[23] M. L. Brongersma, J. W. Hartman, and H. A. Atwater, "Electromagnetic energy transfer and switching in nanoparticle chain arrays below the diffraction limit," Physical Review B 62, R16356-R16359 (2000).

[24] V. R. Almeida, Q. Xu, C. A. Barrios, and M. Lipson, "Guiding and confining light in void nanostructure," Opt. Lett. 29, 1209-1211 (2004).

[25] D. K. Gramotnev and D. F. P. Pile, "Single-mode subwavelength waveguide with channel plasmon-polaritons in triangular grooves on a metal surface," Applied Physics Letters 85, 6323-6325 (2004).

[26] G. Veronis and S. Fan, "Guided subwavelength plasmonic mode supported by a slot in a thin metal film," Opt. Lett. 30, 3359-3361 (2005).

[27] G. Veronis and S. Fan, "Modes of Subwavelength Plasmonic Slot Waveguides," Journal of Lightwave Technology 25, 2511-2521 (2007).

[28] A. Boltasseva, V. S. Volkov, R. B. Nielsen, E. Moreno, S. G. Rodrigo, and S. I. Bozhevolnyi, "Triangular metal wedges for subwavelength plasmon-polariton guiding at telecom wavelengths," Opt. Express 16, 5252-5260 (2008).

[29] M. D. Pozar, Microwave Engineering (John Wiley & Sons, 2012).

[30] X.-S. Lin and X.-G. Huang, "Tooth-shaped plasmonic waveguide filters with nanometeric sizes," Opt. Lett. 33, 2874-2876 (2008).

[31] Y. Matsuzaki, T. Okamoto, M. Haraguchi, M. Fukui, and M. Nakagaki, "Characteristics of gap plasmon waveguide with stub structures," Opt. Express 16, 16314-16325 (2008).

[32] X. Piao, S. Yu, S. Koo, K. Lee, and N. Park, "Fano-type spectral asymmetry and its control for plasmonic metal-insulator-metal stub structures," Opt. Express 19, 10907-10912 (2011).

[33] Y. Huang, C. Min, L. Yang, and G. Veronis, "Nanoscale Plasmonic Devices Based on Metal-Dielectric-Metal Stub Resonators," International Journal of Optics 2012, 13 (2012).

[34] W. Cai, W. Shin, S. Fan, and M. L. Brongersma, "Elements for Plasmonic Nanocircuits with Three-Dimensional Slot Waveguides," Advanced Materials 22, 5120-5124 (2010).

[35] A. Pannipitiya, I. D. Rukhlenko, and M. Premaratne, "Analytical Modeling of Resonant Cavities for Plasmonic-Slot-Waveguide Junctions," IEEE Photonics Journal 3, 220-233 (2011).

[36] Z. Chen, R. Hu, L. Cui, L. Yu, L. Wang, and J. Xiao, "Plasmonic wavelength demultiplexers based on tunable Fano resonance in coupled-resonator systems," Optics Communications 320, 6-11 (2014).

[37] X. Piao, S. Yu, and N. Park, "Control of Fano asymmetry in plasmon induced transparency and its application to plasmonic waveguide modulator," Opt. Express 20, 18994-18999 (2012).

[38] Y. Huang, C. Min, and G. Veronis, "Plasmon-induced transparency in subwavelength metal-dielectric-metal waveguides," in (Proceedings of SPIE, 2011), 79410X-79410X-79417.

[39] G. Cao, H. Li, S. Zhan, H. Xu, Z. Liu, Z. He, and Y. Wang, "Formation and evolution mechanisms of plasmon-induced transparency in MDM waveguide with two stub resonators," Opt. Express 21, 9198-9205 (2013).

[40] Y. Cui and C. Zeng, "All-optical EIT-like phenomenon in plasmonic stub waveguide with ring resonator," Optics Communications 297, 190-193 (2013).

[41] Y. Binfeng, H. Guohua, J. Cong, and C. Yiping, "Plasmon induced transparency in metal–insulator–metal waveguide by a stub coupled with F-P resonator," Materials Research Express 1, 036201 (2014).

[42] W. Yueke, W. Jicheng, L. Cheng, L. Qin, Z. Wenxiu, and G. Shumei, "Plasmonic-Induced Transparency in Metal–Dielectric–Metal Waveguide Bends," Applied Physics Express 6, 082201 (2013).

[43] J. Liu, G. Fang, H. Zhao, Y. Zhang, and S. Liu, "Surface plasmon reflector based on serial stub structure," Opt. Express 17, 20134-20139 (2009).

[44] A. Mahigir, P. Dastmalchi, W. Shin, S. Fan, and G. Veronis, "Plasmonic coaxial waveguide-cavity devices," Opt. Express 23, 20549-20562 (2015).

[45] Lumerical Solutions, Inc. http://www.lumerical.com/tcad-products/fdtd/

[46] E. D. Palik, Handbook of Optical Constants of Solids (1997).

[47] S. E. Kocabas, G. Veronis, D. A. B. Miller, and S. Fan, "Transmission Line and Equivalent Circuit Models for Plasmonic Waveguide Components," IEEE Journal of Selected Topics in Quantum Electronics 14, 1462-1472 (2008).

[48] A. E. Siegman, Lasers (University Science Books, 1986).

[49] A. Mouadili, E. H. E. Boudouti, A. Soltani, A. Talbi, B. Djafari-Rouhani, A. Akjouj, and K. Haddadi, "Electromagnetically induced absorption in detuned stub waveguides: a simple analytical and experimental model," Journal of Physics: Condensed Matter 26, 505901 (2014).

[50] Y. Zhu, X. Hu, H. Yang, and Q. Gong, "On-chip plasmon-induced transparency based on plasmonic coupled nanocavities," Scientific Reports 4, 3752 (2014).

[51] V. J. Sorger, R. F. Oulton, J. Yao, G. Bartal, and X. Zhang, "Plasmonic Fabry-Pérot Nanocavity," Nano Letters 9, 3489-3493 (2009).

[52] S. J. P. Kress, F. V. Antolinez, P. Richner, S. V. Jayanti, D. K. Kim, F. Prins, A. Riedinger, M. P. C. Fischer, S. Meyer, K. M. McPeak, D. Poulikakos, and D. J. Norris, "Wedge Waveguides and Resonators for Quantum Plasmonics," Nano Letters 15, 6267-6275 (2015).

[53] Shitao Gao, Yang Wang, Ke Wang, and Efstratios Skafidas, "High contrast circular grating reflector on silicon-on-insulator platform," Opt. Lett. 41, 520-523 (2016).

[54] Amir Hosseini and Yehia Massoud, "A low-loss metal-insulator-metal plasmonic bragg reflector," Opt. Express 14, 11318-11323 (2006)

[55] A. Kriesch, S. P. Burgos, D. Ploss, H. Pfeifer, H. A. Atwater, and U. Peschel, "Functional Plasmonic Nanocircuits with Low Insertion and Propagation Losses," Nano Letters 13, 4539-4545 (2013).

[56] J. Wen, P. Banzer, A. Kriesch, D. Ploss, B. Schmauss, and U. Peschel, "Experimental cross-polarization detection of coupling far-field light to highly confined plasmonic gap modes via nanoantennas," Applied Physics Letters 98, 101109 (2011).

[57] H. W. Lee, G. Papadakis, S. P. Burgos, K. Chander, A. Kriesch, R. Pala, U. Peschel, and H. A. Atwater, "Nanoscale Conducting Oxide PlasMOStor," Nano Letters 14, 6463-6468 (2014).

[58] Q. Gao, F. Ren, and A. X. Wang, "Efficient optical coupling into ultra-compact plasmonic slot waveguides using dipole nanoantennas," in (Proceedings of SPIE, 2016), 975107-975107-975107.

[59] M. Mansuripur, "Distribution of light at and near the focus of high-numerical-aperture objectives," J. Opt. Soc. Am. A **3**, 2086-2093 (1986).

[60] I. Choi and Y. Choi, "Plasmonic Nanosensors: Review and Prospect," IEEE Journal of Selected Topics in Quantum Electronics 18, 1110-1121 (2012)